**Department of Precision and Microsystems Engineering**

# System identification of the brake setup in the TU Delft Vehicle Test Lab

Jean-Paul Busselaar


| | | |
|---|---|---|
| Report no | : | AUT 2012.018 |
| Coach | : | E.J.H. de Vries |
| Professor | : | E.G.M Holweg |
| Specialisation | : | Vehicle mechatronics |
| Type of report | : | MSc Thesis |
| Date | : | August 20 2012 |

Technische Universiteit Delft

# System identification of the brake setup in the TU Delft Vehicle Test Lab

Jean-Paul Busselaar
MSc. Thesis

Technische Universiteit Delft, The Netherlands

| | |
|---|---|
| Chairman, Examining Committee: | prof.dr.ir. E.G.M. Holweg |
| Daily supervisor: | ir. E.J.H. de Vries |
| External Experts: | dr.ir. M.P. Gerard |
| | dr.ir. M. Corno |

Technische Universiteit Delft
Faculty of Mechanical, Maritime and Material Engineering (3ME)
Department of Precision and Microsystems Engineering (PME)

Delft, 20-8- 2012

# Abstract

Testing facilities such as the TU Delft Vehicle Test Lab (VTL) are needed to provide necessary experimental data to validate and to compare the performance of several ABS controllers like the Feed-Forward Braking controller. Before testing ABS controllers with the VTL measurement system, it needs to be improved first. Earlier measurements reported in [11] showed a lack of developed braking torque due to decreased bandwidth of the measurement setup. This problem could be within the hydraulic brake line of the VTL measurement setup. Pressure dynamics results of the original situation show a significant decrease when increasing the actuating frequency. Differences in pressure dynamics are examined by replacing the original brake hose with a stainless steel braided brake hose. Sinus wave excitation measurements show a relative small increase of the maximal reaching brake pressure with the design improvements situation. Random noise excitation measurements show increased bandwidth, compared to the frequency results reported in [4] and [11]. Improvements in brake pressure dynamics are realized by using a stainless steel braided brake hose in addition with relative low varying amplitudes.

# Acknowledgements

I would like to give special thanks to my daily supervisor ir. Edwin de Vries for his constant guidance and support. This is regarding theoretical analysis as well as practical input, especially in the Vehicle Test Lab. My thanks go also to Mathieu Gerard and Matteo Corno for their support on testing procedures in the VTL. I want to thank prof. Edward Holweg for being the chairman of the examination committee as replacement of prof. Daniel Rixen.
My gratitude goes towards M.T. members of TOTAL Nederland N.V., namely M.D. Benoît Ortegat, Nathalie Baras, Gerhard Dekker, also my daily supervisor Sander de Geus and colleagues of TOTAL Technical Support for giving me the possibility to finish my thesis.
I wish to express my sincere gratitude to my parents and friends who have always been beside me through periods of joy and sorrow.

Delft, University of Technology Jean-Paul Busselaar
August 20, 2012

# Table of Contents

# List of Figures

# List of Tables



# Nomenclature

ABS: Anti-lock Braking System
DUT: Delft University of Technology
FFT: Fast Fourier Transform
LuGre: Lund and Grenoble Universities
SDL: Sequence Description File
MDL: Model file
RTI: Real Time Interface
VTL: Vehicle Test Lab

# Outline of the Report

The automotive disc brake, general tire basics, tire force generation and tire friction modeling and analysis issues will be explained in Chapter 1.The quasi-physical LuGre tire friction model analysis forms the basis of the Feed Forward ABS control. Chapter 2 will explain some basics of the Feed Forward ABS controller and VTL brake torque research described in [11]. Chapter 3 discusses the VTL and the data acquisition. In Chapter 4 the experimental validation is presented and static brake pressure results of the sinus wave excitation are explained of the original situation and the situation with design improvements. Chapter 5 shows the system identification of the VTL measurement setup and its random noise excitation results of the situation with design improvements. Chapter 6 is the conclusion of this thesis.

# Chapter 1
# Introduction

Improving cars in terms of driving comfort and pleasure as well as driving safety has always been the aim of car-manufacturers. Traffic has been increased for several decades and at the same time the number of road accidents has risen. The control of vehicle motion is becoming important by increasing demands in driving safety. The vehicle's stability during braking and cornering has to be maintained. By regulating the hydraulic pressure applied on the brakes, the lateral stability and steerability will increase especially during wet and icy road conditions. Physical properties related to tire-road friction behaviour are converted into mathematic models. The tire friction behaviour and road conditions are strongly affect the control schemes of the mathematic models. Based on its control schemes, an Anti-lock Braking System (ABS) adjusts the maximum brake force of each wheel and intends to prevent wheel lock and therefore skidding during braking.

## 1.1 Scope and aims

Old fashioned ABS systems regulate the brake pressure as an on-off switch in a rough way. While controlling the wheel speed of each wheel, the ABS control cycles around a target slip. To avoid this way of controlling the wheel speed as much as possible, an alternative Feed-Forward ABS control design is proposed by authors of [15]. This alternative control design decelerates each wheel first until the desired target point is reached. Then the ABS control cycles around the desired target point at a lowered wheel speed for a more efficient and effective wheel speed control. This optimal behaviour consists of a minimal braking distance and no wheel lock. Student Marien van Ditten who researched this ABS control before, reported his work in [11]. He focussed initially on testing the developed Feed-Forward ABS brake actuation algorithm on the TU Delft Vehicle Test Lab (VTL). During his research the maximal brake force of the VTL measurement setup seems to be too low to test the performance of the Feed-Forward Braking controller. The purpose of the work reported in this thesis is to identify and improve the brake pressure dynamics in the VTL measurement setup. Experimental data results of the original situation and the situation with design improvements are used to identify the dynamics. As well as optimizing controller gains and filter frequency settings in case of the mounted new hydraulic brake line. It is initially intended to modify the VTL measurement setup adequately, in order to test the performance of the Feed-Forward controller. Due to practical problems during the thesis project, the assignment is focused on improving the bandwidth of the VTL measurement setup

The following goals of this thesis are:

1. Introducing the reader about automotive brakes, tire dynamics and models.
2. Introducing the reader about the background of the Feed-Forward ABS control design.
3. Describing the TU Delft Vehicle Test Lab and data acquisition.
4. Presenting experimental data and system identification results of the measurement brake set up.

## 1.2 Automotive Disc Brakes

Before explaining details about the ABS system, the main parts for braking and parts influencing the brake force will be discussed first.
The automotive disc brake is a most common example of a braking system mounted on a car. The kinetic energy has to be transferred into heat by friction for slowing down the vehicle. The brake torque is developed by pushing the pads on the rotating brake disc. Figure 1.1 shows a typical automotive disc brake. The caliper forms the brake actuator, mounted on the steering knuckle and actuating the pads by a hydraulic piston. A ‘floating’ caliper brake is used on the VTL measurement setup and its design will be shortly described. A ‘floating’ caliper contains one piston at the inboard pad and an outboard pad inside a sliding part. While the piston pushes the inboard pad onto the brake disc, the sliding part will be pulled and pushes the outboard pad also onto the rotating brake disc. A ‘floating’ caliper is a cheaper design than a caliper with multiple pistons on both sides. Figure 1.2 shows the forces acting on the brake pads during braking. In appendix A-2 a basic simplified transfer function equation of a caliper can be found.

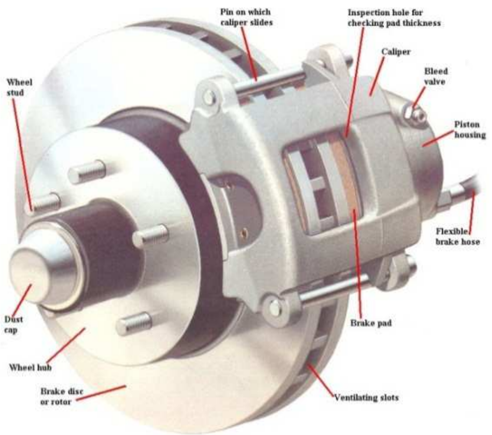


Figure 1.1 a typical Automotive Disc Brake System [2]

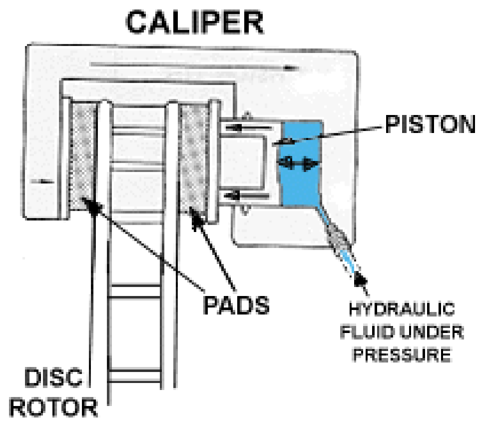


Figure 1.2 Actuation of the brake pads using a floating caliper type [2]

The dimensions of the rotor are determining the brake torque and the thermal properties. Increasing the brake disc diameter increases the brake torque with the same caliper force. Increasing the width of the brake discs and/or using ventilated brake discs will increase the thermal capacity; the ability to absorb and release the generated heat by friction due to the pads pushing on the rotating brake disc. The dimensions of the pads are determining the pads pressure distributed onto the disc and influencing the wear of the brake parts. While the composition of the brake pad material determines the friction and thus the generated brake force. Composition of relative softer brake pad material will increase the friction due to higher shear forces of the brake pads during braking. The hydraulic actuation of the brakes is influenced by its response. The response is based on the quotient between the output- and input signal, i.e. the piston displacement and the force resulting from the braking pressure. The difference between the measured and desired value is called the error. Decreasing the error can be done by decreasing the brake hose diameter and increasing the stiffness of the brake line material. Theoretically the brake pressure dynamics increase and therefore the response time decreases and will result into an improved brake actuation.

## 1.3 Tire Basics and Terminologies

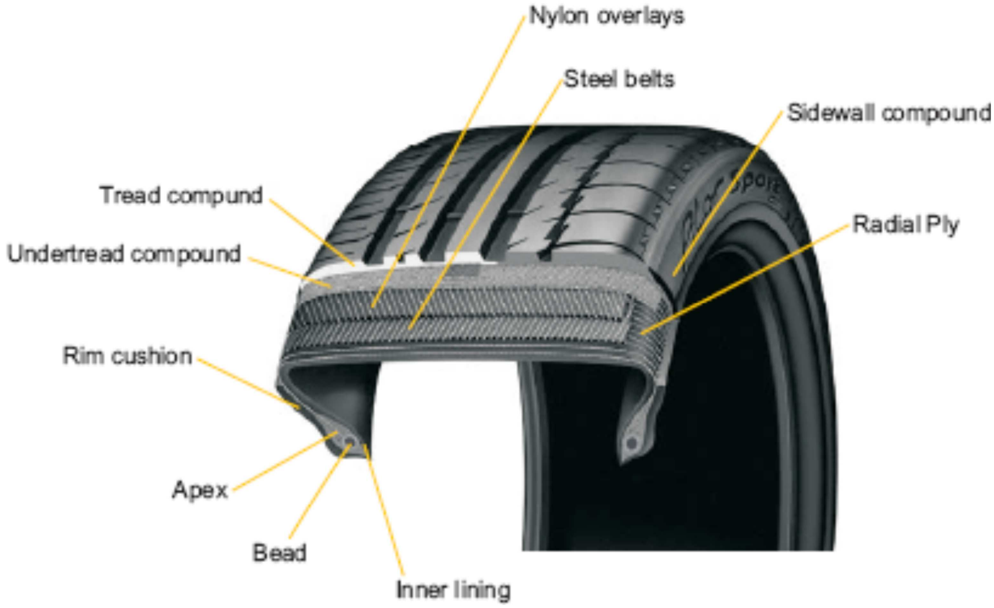

Figure 1.3 section of a tire structure

A tire as figure 1.3 shows is build up by several layers, to give strength towards the applied forces and moments. These forces and moments will be explained in section 1.4. A tire is a donut shape, composed of especially synthetic rubber with metal cords (beads) and several steel belts (brass plated steel wires) and nylon overlays. On top of the plies is thick, wear resisting tread rubber placed.

The behaviour and the maximum friction coefficient decrease significant, when the road conditions are going to be more slippery. There is no maximum friction-slip peak available and these are challenging situations for ABS system designs. Figure 1.4 shows the friction curve in different road conditions.

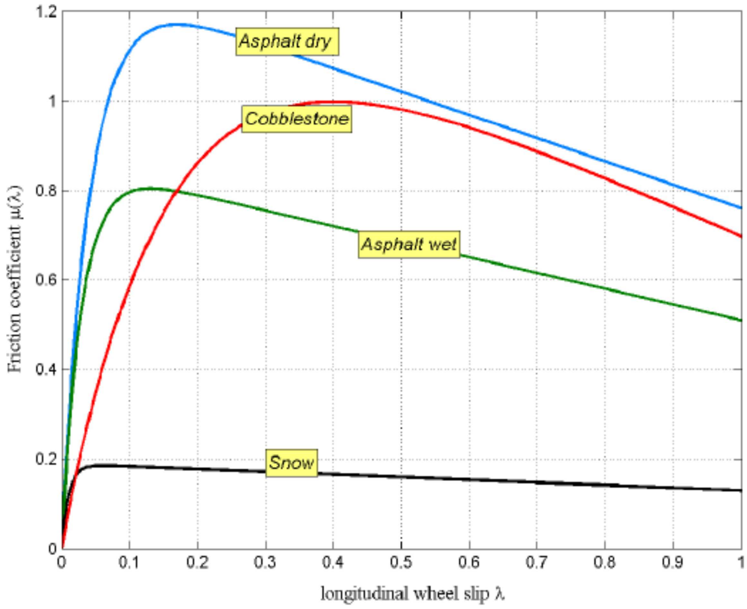

Figure 1.4 Friction Curve. Behaviour of the friction coefficient in different road conditions [25]

## 1.4 Tire Force Generation

The dynamic behaviour of the tire is suggested in a coordinate system. There is an interaction between the tire and the road due to several forces and moments.

The three forces are:

*1. Longitudinal force* $F_x$

*2. Lateral force* $F_y$

*3. Normal force* $F_z$

The three moments are:

*1. Overturning moment* $M_x$

*2. Rolling moment* $M_y = M_w$

*3. Yawing moment / self-aligning torque* $M_z$

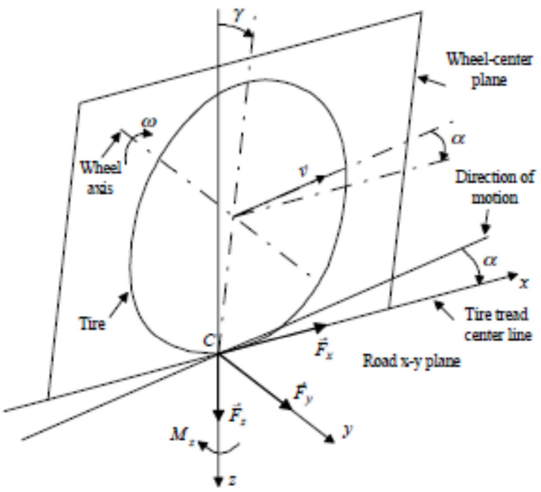


Figure 1.5 Tire axis definition and contact coordinates [25]

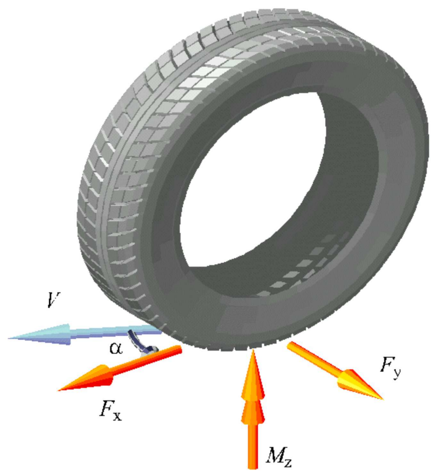


Figure 1.6 tire forces and moment

The longitudinal force $F_x$ results from the tire braking on the road; the lateral force $F_y$ is produced by a (non-zero) camber $\gamma$ angle and a (non-zero) slip angle $\alpha$ during cornering. *Side slip* $\alpha$ is the angle between the tire longitudinal axis and the wheel velocity vector. *Longitudinal slip* $\lambda$ is the normalized ratio of the slip velocity and vehicle velocity: $\lambda = \dfrac{v - \omega \cdot r}{\max\left(v, \omega \cdot r\right)}$. *Camber angle* $\gamma$ is the angle between the vertical plane and the wheel plane. The normal force $F_z$ is resulting from the vehicle's mass. The overturning moment $M_x$ is the result of the lateral shift of the vertical load during cornering. Different factors that lead to energy losses create the rolling resistance $M_y$. The self-aligning torque $M_z$ produces a restoring moment on the tire which tends to realign the direction of travel with the direction of heading when the slip angle is non-zero. The camber angle $\gamma$ and slip angle $\alpha$ are the most important angles, indicated in figure 1.5, while figure 1.6 shows tire forces $F_x$, $F_y$ and self-aligning torque $M_z$. The dependency of the longitudinal force $F_x$ as well as the lateral force $F_y$ is put in the following generic equations:

$$F_x = \mu_x(\alpha, \lambda, \gamma)F_z$$
$$F_y = \mu_y(\alpha, \lambda, \gamma)F_z$$

$where: \ \alpha : side\ slip\ angle \qquad \lambda : longitudinal\ slip$

$F_z : normal\ load \qquad \gamma : camber\ angle$

$F_x : longitudinal\ force \qquad F_y : lateral\ force$

$M_z : yawing\ moment$

The tire has several functions as carrying and suspending the vehicle load, a more important feature is the load distributed through the tire. This has a big influence in the way the contact force will be generated.

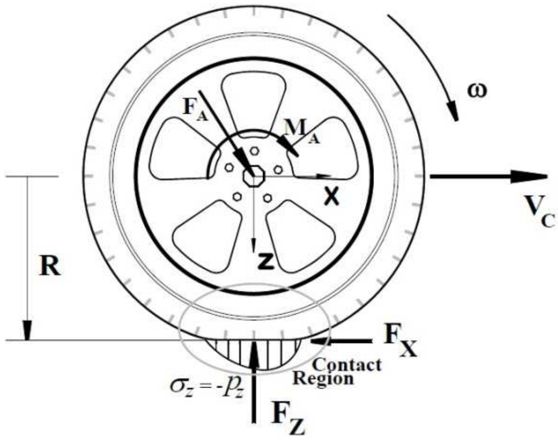


Figure 1.7 Forces applied to a rotating wheel and the effects over the contact area

The tire carries the load by the radial cords shown in Figure 1.3. Pretension of the radial cord is exerted by pressurized air inside the tire. A stationary tire on a flat and stiff ground will deflect under its weight and depending on the air pressure inside it. This generates a pressurized contact area to balance the vertical load. Due to geometry changes of the circular tire in contact with the ground, a three dimensional stress distribution will appear in the contact patch. The tire bending stiffness, inflation pressure and environmental conditions, wheel positions etc. influence the pressure distribution on the contact patch. The contact patch dimensions are also influenced by these factors. A common phenomenon in vehicle tire mechanics is the brake force (during wheel slip) before wheel lock can exceed the force level achieved at a wheel-lock. Peak forces are fundamental for the functioning of ABS systems. The longitudinal force $F_x$ is generated by friction. Friction can be described as the resistance to relative tangential motion during braking at the compressive contact interface between a tire and the road surface [14]. According to figure 1.7 force $F_A$ and moment $M_A$ are applied to the wheel. The normal force between the tire and the ground is $F_Z$ and the frictional force between the tire and the ground is $F_X$. Force $F_X$ and $F_Z$ are point-contact forces used to represent the effects of distributed forces over the contact area. In reaction to the applied force $F_A$ and moment $M_A$, the forces $F_X$ and $F_Z$ are developed. The ratio of the longitudinal force $F_X$ to the compressive force $F_Z$ is defined as the friction coefficient $\mu$ .

## 1.4.1 General Tire Kinematics

Tire kinematics can be visualized as different velocity components of a tire. Figure 1.8 shows the velocity vector V, which is the direction of the wheel travel. Lateral tire motion is produced by the wheel plane at an angle $\alpha$ to the direction of travel.

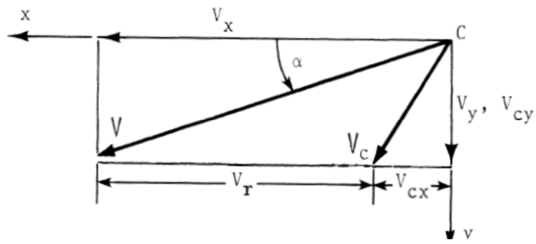

Figure 1.8 Kinematics of tire motion when braking is applied [8]

The travel velocity is composed of two components in the $x, y$ coordinate system. *The longitudinal component*: $V_x = |V|\cos\alpha$ is composed of the wheel velocity $V_r$ and the velocity $V_{cx}$, produced by the longitudinal slip and the contact region. *The lateral component*: $V_y = |V|\sin\alpha$ consists of entirely lateral elastic slip or sliding, generally termed the lateral slip velocity $V_{cy}$. *The tire slip velocity vector* $V_c$ is defined by the slip velocity components $V_{cx}$ and $V_{cy}$ as shown in figure 1.8.
The rolling velocity of a free rolling tire is equal to the velocity $V_x$.

$$V_r = V_x \qquad \text{(Free rolling)} \qquad (1)$$

The effective rolling radius $R_e$ is defined as the ratio of the free rolling velocity to the wheel spin velocity $\omega$ .

$$R_e = \frac{V_r}{\omega} \qquad \text{(Free rolling)} \qquad (2)$$

The effective rolling radius value lies between the loaded and unloaded radius.

$$V_r = \omega R_e \qquad (3)$$

During braking the longitudinal velocity $V_x$ and rolling velocity $V_r$ are reduced by a certain amount each instant in time. The difference is the longitudinal slip velocity $V_{cx}$ shown in figure 1.8 at a certain instant in time.

$$V_{cx} = V_x - V_r \qquad (4)$$

In case of applying driving torque, the elastic deformation and sliding cause the rolling velocity $V_r$ to exceed the longitudinal velocity and $V_{cx}$ becomes negative.

The longitudinal slip parameter $\lambda$ is defined as the fraction of longitudinal velocity which indicates the amount of braking torque is applied [8].

$$\lambda = \frac{V_{cx}}{V_x} \rightarrow \lambda_b = \frac{V_{cx}}{V_x} = \frac{V_x - V_r}{V_x} = 1 - \frac{\omega R_e}{V_x} (braking) \quad (5)$$

For braking, the wheel slip takes on values $0 \le \lambda_b \le 1$.

A free rolling wheel is represented with $\lambda_b = 0$. A locked wheel is indicated by $\lambda_b = 1 \; (V_{cx} \neq 0 \; and \; \omega = 0)$. All other values of $\lambda_b$ represent intermediate values of slip of the contact point of the tire relative to the ground surface. Figure 1.9 visualizes the longitudinal tire force as a function of the wheel slip during acceleration and braking.

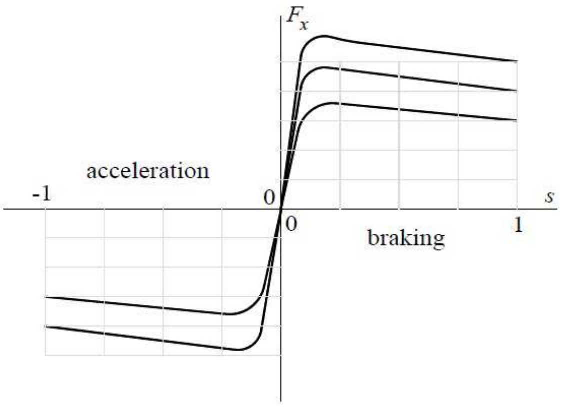


Figure 1.9 Typical longitudinal tire force curves as a function of wheel slip s (= $\lambda$ )

For *the lateral slip parameter* $\lambda_y$ it is defined to be

$$\lambda_y = \frac{V_{cy}}{V_x} = \tan\alpha \quad (6)$$

$V_{cy}$ is *the lateral slip velocity* as can be seen in figure 1.8. By eliminating $V_{cx}$ and substituting the result into (7) for $V_x$ [8]:

$$\frac{V_{cy}}{V_r} = \frac{\lambda_y}{1 - \lambda_x} \quad (7)$$

*The slip velocity magnitude* $V_c = |V_c|$ is computed from components $V_{cx}$ and $V_{cy}$

$$V_c = \sqrt{V^2{}_{cx} + V^2{}_{cy}} \rightarrow \frac{V_c}{V_r} = \frac{\sqrt{\lambda_x{}^2 + \lambda_y{}^2}}{1 - \lambda_x} \quad (8)$$

In case of wheel-lock $(\lambda_x \rightarrow 1, V_r \rightarrow 0)$ the slip velocity approaches the travel velocity and full sliding develops in the contact region [8].

At wheel-lock:

$$\begin{aligned} V_{cx} &= V_x && (equation\ (4), V_r = 0) \\ V_{cy} &= V_y && (always) \\ V_s &= V_c = V \end{aligned}$$

ABS controllers are optimized at the transition of the rising and falling slope as shown in figure 1.10. The wheel slip value $\lambda_{\max}$ which corresponds to the peak-value of the tire-road friction curve $\mu_{\max}$ is the stability boundary for the wheel braking dynamics [22]. The linearized wheel braking dynamics are stable for values of the wheel slip smaller than the peak value $\lambda_{\max}$ (left side) and unstable for those beyond the peak $\lambda_{\max}$ (right side).

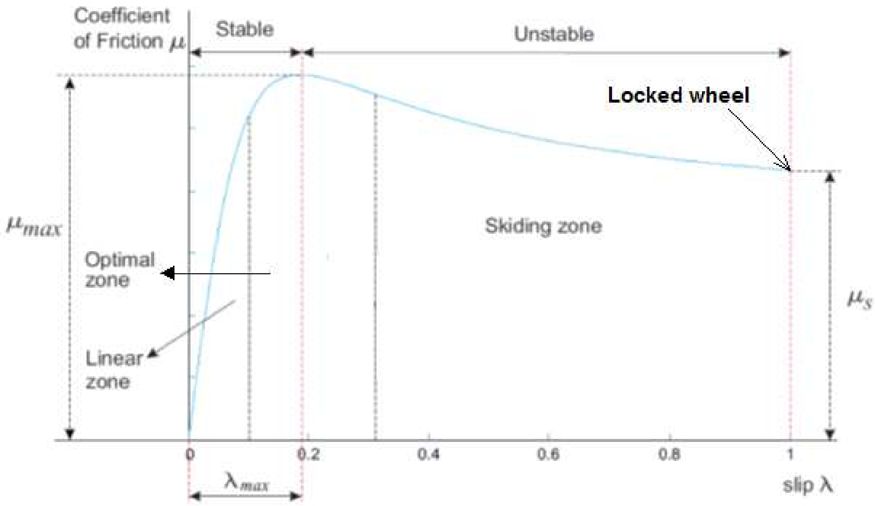

Figure 1.10 Typical pseudo-static tire/road friction model during braking [10].

Identification of the algorithm for estimating the peak-value $\mu_{\max} - \lambda_{\max}$ can provide a reliable estimation for ABS activation. This enhances greatly safety properties of active control systems and allows optimizing the closed loop performance of ABS system.

## 1.5 Tire Friction Models

Tire models are used to describe tire responses under various loading and operation conditions. A tire model should fit measurement data and is used to predict the dynamic response of the tire beyond the test range with an acceptable physical interpretation by optimal choice of included parameters [4], [9].
***Steady state*** and ***transient dynamic responses*** are the two primary aspects researched in friction mechanics. These two aspects are switching continuously during driving. ***Steady-state*** and ***transient dynamic response*** investigations focus on *out-of-plane* cornering forces, like slip angles changes, self-aligning torque, lateral deformation and stiffness analysis which are resulting from steering. These aspects are focused on pure tire characteristics and are related to vehicle drivability and controllability. The steady state and transient dynamic response focus also at the *in-*

*plane* vertical, like longitudinal, tangential and tractive force at the tire-ground interface region or at the centre of the tire assembly. This largely arises from road roughness or tire assembly non- uniformities. These aspects cover more the whole vehicle integrity response and more related to vehicle ride comfortability. Transient dynamic response situations can reach steady state during slipping. By using ***Empirical*** or ***Quasi-Physical model*** approaches these mentioned aspects may be derived.
Empirical models are based on experimental data and generally do not have a physical interpretation of friction and are more suitable for control purposes. Quasi-Physical models are expressed based on physical interpretation of friction. The Feed-Forward ABS control uses a Quasi-Physical model approach and will be explained.

### 1.5.1 Quasi-Physical model approach LuGre based tire friction model

Canudas de Wit et. al. [1], [5], [27] has proposed an alternative dynamic model for longitudinal tire force, based on the previously developed LuGre (Lund and Grenoble Universities) dynamic tire friction model. This model combines the advantages of the earlier dynamic tire models; it is originally expressed in the distributed “brush” form and it can be transformed into a simple lumped form. It includes more accurate tire friction description than the brush model proposed by Van Zanten et. al. [5] and has a compact form which is convenient for different tire dynamics analysis and estimation purposes [1], [9], [27].Authors of [1] and [27] claimed that this alternativefriction model is able to accurately capture the transient behaviour of the friction force observed during transitions between braking and acceleration. It is expected that this model will be very helpful for tire friction modelling as well as Anti-lock Braking System (ABS) and traction control design. The proposed model has the advantage that it is developed starting from first principles, based on a simple point-contact dynamic friction model see the left part of figure 1.13. The parameters entering the model describe the physical behaviour. This allows the designer to tune the model parameter using experimental data. The proposed friction model is also velocity dependent and has a simple parameter to capture the road surface characteristics. In contrast to many other stationary models, this model is shown to be well-defined everywhere, even at zero rotational or linear vehicle velocities. Also appropriate for any vehicle motion situations as well as for control law design, especially important during transient phases of the vehicle operation such as braking or acceleration [1].
Before going into the dynamic friction models, the basic static friction and the dynamic friction will be explained.

### ***Stationary models***

Static friction is determined by the friction coefficient $\mu$ and the normal force $F_n$. In general it is supposed that friction opposes motion and its magnitude is independent of velocity and contact area. The friction force can be described as a function of the Coulomb force and velocity as shown in figure 1.11 [26].

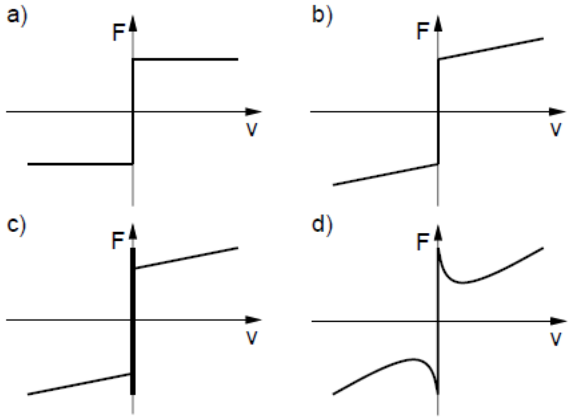


Figure 1.11 Evolution approach Coulomb friction as function of the velocity [26]

Where:

| | |
|---|---|
| $F_c = \mu F_n$ | (Coulomb friction force) |
| | $F_c = 0$ or any value between $-F_c$ and $F_c$ |
| a) $F = F_c \operatorname{sgn}(\upsilon)$ | (Coulomb friction force as function of the velocity) |
| b) $F = F_\upsilon \upsilon$ | (Linear viscous friction force) |
| c) $F = F_s \operatorname{sgn}(F_e) + F = F_\upsilon \upsilon$ | (Stiction and linear viscous friction force) |
| | $F_s$ varies between $-F_s$ and $F_s$ |
| d) $F = F_\upsilon \lvert\upsilon\rvert^{\delta_\upsilon} \operatorname{sgn}(\upsilon)$ | (Coulomb friction with the Stribeck function), |
| | $\delta_v$ depend on geometry of the application |

For a more accurate stationary friction model approach, the standard Coulomb friction (a) undergoes an evolution shown in figure 1.11. At first added with a linear viscous friction (b) and with stiction (c), finally the viscous friction and stiction is described by the Stribeck function (d). The Stribeck function forms an important feature in the LuGre tire model to approach the viscous behaviour of tire rubber. A common form of the friction law is [26]:

$$F(\upsilon) = F_c + (F_s - F_c)e^{-\left|\frac{\upsilon}{\upsilon_S}\right|^{\delta_S}} + F_\upsilon \upsilon \qquad (1)$$

where $\upsilon_s$ is the Stribeck velocity. Function $F$ is easily obtained by measuring the friction force for motions with a constant velocity, the curve is often asymmetrical. Stationary tire models can explain the physical deflections of the tire-road interaction. Because of the assumption that the deformation reaches its steady-state, the dynamic friction behavior is not described.

***Dynamic models***

Dynamic friction behaviour is of importance for studying the transient behaviour of the tire friction and has direct influence on vehicle dynamics and stability. In reality the development of tire forces is much a dynamic phenomenon. Dynamic tire friction models which are *quasi-physical* can capture transient behaviour of the friction forces and are thus more suitable for vehicle control applications. An example is the LuGre tire friction model; it is used to predict the friction forces during transient situations [1]. This quasi-physical friction model is developed from several dynamic models, which will be explained first.

*Dahl model*

The Dahl model [1] is developed for simulating control systems with friction and is used for adaptive friction compensation. Dahl modelled the stress-strain curve by a differential equation. In the Dahl model *the friction force* is only a function of the *displacement* ($F - x_r$ plane) and *the sign of the relative* velocity $\upsilon_r$ , (the direction of motion) but not on the magnitude of the relative velocity $\upsilon_r$ .This implies rate-independent hysteresis loops in the $F - x_r$ plane [1], [26]. Let $x_r$ be the relative displacement of the two contact surfaces and $\upsilon_r = \frac{dx_r}{dt}$ is the relative velocity between the two surfaces, the maximal force (Coulomb force) $F_c$ and the Friction force $F$ ; the Dahl's model becomes:

$$\frac{dF}{dx} = \sigma \left( 1 - \frac{F}{F_c} \operatorname{sgn} \upsilon \right)^{\alpha} \qquad (2)$$

$\sigma$ is the stiffness coefficient and $\alpha$ is the shape parameter of the stress-strain curve, value $\alpha = 1$ is most commonly used. For this specific situation, the friction force $|F|$ is never larger than the Coulomb force $F_c$ .To obtain a time domain model, [1]:

$$\frac{dF}{dt} = \frac{dF}{dx_r} \frac{dx_r}{dt} = \frac{dF}{dx_r} \upsilon_r = \sigma \left( 1 - \frac{F}{F_c} \operatorname{sgn} \upsilon_r \right)^{\alpha} \upsilon_r \qquad (3)$$

*Bristle Model*

According to [26] Haessig and Friedland introduced a friction model which attempts the behaviour of microscopically contact points between two surfaces. The location of the contact points is random due to irregularities in the surfaces. Each point can be thought of as a bond between flexible bristles. In case of surfaces moving relative to each other, the strain bond increases and the bristles act as springs giving rise to a friction force. The next equations (4) show the similarity in the spring force and bristle force.

$$F_{SPRING} = \sum_{i=1}^{N} ku \equiv F_{BRISTLE} = \sum_{i=1}^{N} \sigma_0 \left( x_i - b_i \right) \qquad (4)$$

Where:

- k: the stiffness of the spring
- u: displacement
- N: the number of the bristles
- $\sigma_0$: the stiffness of the bristles
- $\sigma_1$: the damping of the bristles (stiction case)
- $x_i$: the relative position of the bristles
- $b_i$: the location where the bond was formed

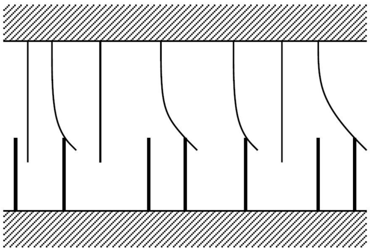

Figure 1.12a bristle interpretation [26]

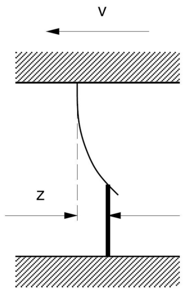


Figure 1.12b single bristle interpretation [26]

As $|x_i - b_i| = \delta_s$ the bond snaps and a new one is formed at a random location, relative to the previous location. In [26] it is claimed that good results are found with 20-25 bristles, but even a single bristle gives reasonable qualitative behaviour. The stiffness of the bristles $\sigma_0$ can be made velocity dependent. Capturing the random nature of friction is an advantageous property of the bristle model. The model is inefficient in simulations due to its complexity. Because of no damping of the bristles, motion in sticking may be oscillatory. To overcome this problem, Haessig and Friedland proposed the *reset integrator* [26]. Instead of snapping a bristle, *the bond is kept constant* by shutting off the increase of the strain at the point of rupture.
The friction force than becomes:

$$F = (1 + a(z))\sigma_0(\upsilon)z + \sigma_1 \frac{dz}{dt} \qquad (5)$$

Where $\sigma_1$ is the *damping term* and is only active in a *stiction* situation.
The damping coefficient can be chosen to give a desired relative damping of the resulting spring-mass-damper system [26].

*LuGre Friction Model*
The LuGre friction model is the extended version of the Dahl's model, which can capture friction phenomena. The main drawbacks of Dahl's model are eliminated with the extension of the Dahl model with the Stribeck effect. The constant Coulomb friction force $F_c$ in Dahl's model is replaced by the speed dependent sliding friction function $g(\upsilon_r)$. Such as a *varying break-away force* and *frictional lag* is included in this model. Moreover the linear stiction damping term as well as the linear viscous friction term is introduced. These modifications lead to the LuGre friction model [1], [5], [9] and [27]. This total LuGre model is related to the *bristle* interpretation of friction. *Friction is modelled as the average deflection force of elastic springs*. By applying a tangential force the bristles deflect like springs.

The force is given by: $$F = \sum_{i=1}^{N} \sigma_0 (x_i - b_i) \tag{6}$$

The LuGre model can capture the Stribeck effect, hysteresis, spring-like characteristics for stiction and varying break-away force. Because of these properties, authors of [5] introduced the LuGre tire model. The advantage is that all these friction phenomena are unified into a first-order nonlinear differential equation. Figure 1.13 shows a schematic interpretation of the bristle contact of the tire with the road.

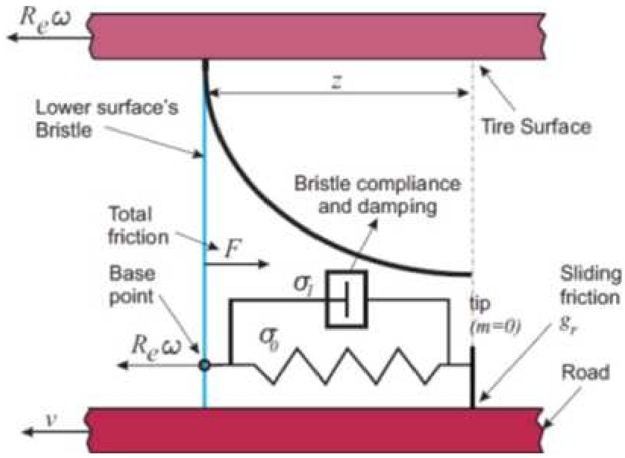


Figure 1.13 a schematic bristle contact between two surfaces according to the LuGre model

The model has the form:

$$\begin{aligned} \frac{dz}{dt} &= \upsilon - \sigma_0 \frac{|\upsilon|}{g(\upsilon)} z \\ F &= \sigma_0 z + \sigma_1(\upsilon) \frac{dz}{dt} + f(\upsilon) \end{aligned} \tag{7}$$

where: $\sigma_0$: stiffness of the bristles
$\sigma_1(\upsilon)$: damping of the bristles
$g(\upsilon)$: shaping factor, it models the Stribeck effect
$f(\upsilon)$: models the viscous friction

$z$ denotes the *average bristle deflection*; this model behaves like a *spring for small displacements.* Linearization around *zero velocity and zero state* gives:

$$\begin{aligned} \frac{d(\delta z)}{dt} &= \delta\upsilon \\ \delta F &= \sigma_0 \delta z + (\sigma_1(0) + f'(0))\delta\upsilon \end{aligned} \tag{8}$$

For constant velocity, the *steady state friction force* is given by:

$$F = g(\upsilon)\operatorname{sgn}(\upsilon) + f(\upsilon) \tag{9}$$

The friction force as a function of velocity for *constant velocity motion* is called the *Stribeck curve*. In particular the dip in the force at low velocities is called the *Stribeck effect.* In [26] a reasonable choice of $g(\upsilon)$ a good approximation of the Stribeck effect:

$$g(\upsilon) = \alpha_0 + \alpha_1 e^{-\left(\frac{\upsilon}{\upsilon_0}\right)^2} \tag{10}$$

The sum $\alpha_0 + \alpha_1$ corresponds to the *stiction force* and $\alpha_0$ to the *Coulomb friction force*. Parameter $\upsilon_0$ determines how $g(\upsilon)$ vary within its boundaries:

$$\alpha_0 < g(\upsilon) \le \alpha_0 + \alpha_1$$

There is a special case of the model, which is called the *standard parameterization*. Within this model the *viscous friction is linear and $\sigma_1$ is constant* [26].

$$\begin{aligned}
&\frac{dz}{dt} = \upsilon - \sigma_0 \frac{|\upsilon|}{g(\upsilon)} z \\
&g(\upsilon) = \alpha_0 + \alpha_1 e^{-\left(\frac{\upsilon}{\upsilon_0}\right)^2} \\
&F = \sigma_0 z + \sigma_1 \dot{z} + \alpha_2 \upsilon
\end{aligned} \tag{11}$$

It is further claimed by authors of [26] that a decreasing damping $\sigma_1$ with an increasing velocity is useful.

$$\sigma_1(\upsilon) = \sigma_1 e^{-\left(\frac{\upsilon}{\upsilon_d}\right)^2} \tag{12}$$

This is physically motivated by the *change of the damping characteristics as velocity increases,* due to more lubricant being forced into the interface. Another reason is that it gives a *dissipative* model (dissipating energy from its system) [26].

*Types of LuGre models*
The basic idea of the quasi-physical tire friction model is to assume friction dynamics reach their steady state between the tire and the ground.

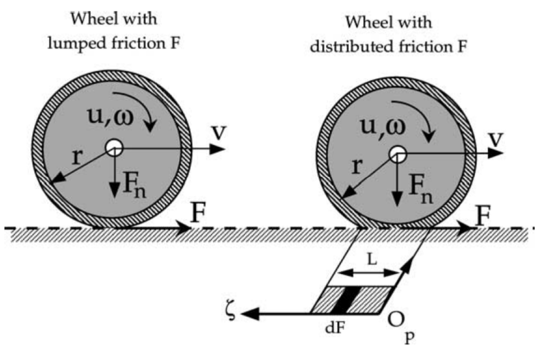


Figure 1.14 One-wheel models with lumped friction (left) and distributed friction (right) [1]

Generally speaking, dynamic models can be formulated as *lumped* or as *distributed models* as can be seen in figure 1.14. A lumped friction model is based on a point tire-road friction contact. The mathematical model describes such friction model, which contains ordinary differential equations that can be solved easily by time integration. Distributed friction models are based on the existence of a contact patch between tire and ground with an associated normal pressure distribution. This results in a partial differential equation that needs to be solved both in time and space [1].

Lumped LuGre model
A lumped friction model assumes point tire-road friction contact. From [1], [9], [23], and [26] the lumped LuGre model can be modelled by an ordinary differential equation:

$$\dot{z} = -\sigma_0 \frac{|\upsilon_r|}{g(\upsilon_r)} z + \upsilon_r$$

With
$$g(\upsilon_r) = \mu_C + (\mu_S - \mu_C) e^{-\left|\frac{\upsilon_r}{\upsilon_S}\right|^{\alpha_g}} \tag{13}$$

$$F = (\sigma_0 z + \sigma_1 \dot{z} + \sigma_2 \upsilon_r) F_n$$

$$F_{Steady\ State} = \left( \frac{g(\upsilon_r)}{|\upsilon_r|} + \sigma_2 \right) \upsilon_r F_n \tag{14}$$

With defined $z$ during steady state as: $-\frac{\mu_S}{\sigma_0} \leq z \leq \frac{\mu_S}{\sigma_0}$

The LuGre friction model is transformed into a more attractive form. The stiffness, damping coefficients and conductance are in physical units as a function of $F_n$ $[N]$. Where $\sigma_0$ is the normalized rubber longitudinal lumped stiffness $\left[\frac{1}{m}\right]$, $\sigma_1$ the normalized rubber longitudinal damping $\left[\frac{s}{m}\right]$, $\sigma_2$ the normalized viscous relative damping $\left[\frac{s}{m}\right]$, $g(\upsilon_r)$ the tire/road friction as function of the sliding velocity $[-]$, $\mu_c$ the normalized Coulomb friction $[-]$, $\mu_s$ the normalized static friction, $(\mu_C \leq \mu_S)$ $[-]$, $\upsilon_S$ the Stribeck relative velocity $\left[\frac{m}{s}\right]$, $\upsilon_r = (r\omega - \upsilon_x)$ the relative velocity $\left[\frac{m}{s}\right]$, $\alpha_g$ the shaping factor $[-]$, $F_n$ the normal force $[N]$ and $z$ the internal friction state $[m]$. The constant parameter $\alpha_g$ $[-]$ can be used to capture the steady-state friction/slip characteristic [1], [26], [27].

*Distributed LuGre Model*
Changing the lumped LuGre model to approach the distributed LuGre model a 'convection-loss' property is inserted. This property is needed to indicate the distortion in the rolling model during entering the contact patch and restoring the patch after passing the contact with the road. The distributed friction models assume the existence of an area of contact or patch in between the tire and road, as shown in figure 1.15. The contact patch represents the projection of the part of the tire that is in contact with the road, coloured in green. The contact patch area is discretized to a series of elements and the microscopic deformation effects are studied in detail by Bliman et. al. [5]. They characterize the elastic and Coulomb friction forces at each point of the contact patch. The lumped friction model (13) can be extended to a distributed friction model along the patch by letting $z(\varsigma, t)$. Denote the friction state (deflection) of the bristle/patch element located at point $\varsigma$ along the patch at a certain time $t$ [1], [27].

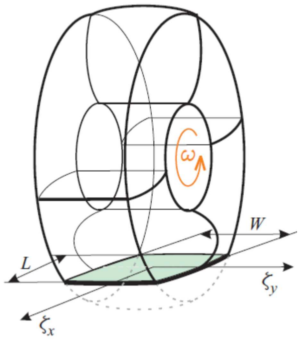

Figure 1.15 A distributed bristle deflection function $(\varsigma_x \; and \; \varsigma_y)$ on the contact patch

The lumped friction model:

$$\dot{z} = -\sigma_0 \frac{|\upsilon_r|}{g(\upsilon_r)} z + \upsilon_r$$

$$g(\upsilon_r) = \mu_C + (\mu_S - \mu_C) e^{-\left|\frac{\upsilon_r}{\upsilon_S}\right|^{\alpha_g}} \qquad (15)$$

$$F = (\sigma_0 z + \sigma_1 \dot{z} + \sigma_2 \upsilon_r) F_n$$

Model (15) can be written as:

$$\frac{dz}{dt}(\varsigma, t) = \upsilon_r - \frac{\sigma_0 |\upsilon_r|}{g(\upsilon_r)} z \qquad (16)$$

$$F = \int_0^L dF(\varsigma, t) \qquad (17)$$

Where $$dF(\varsigma,t) = \left( \sigma_0 z(\varsigma,t) + \sigma_1 \frac{\partial z}{\partial t}(\varsigma,t) + \sigma_2 \upsilon_r \right) dF_n(\varsigma,t)$$

$dF(\varsigma, t)$ is the *differential friction force* developed in the element $d\varsigma$ and $dF_n(\varsigma,t)$ is the *differential normal force* applied in the element $d\varsigma$ at time $t$. In this model the *contact velocity* is assumed to be equal to the *relative velocity* $\upsilon_r$ .

# Chapter 2
# Anti-lock Braking System

## 2.1 Introduction

Braking performance is a main issue for road vehicles. In case of an emergency, vehicle safety relies on the braking system which must provide maximum friction force and maintain directional control. However, excessive brake level results in locked wheels and loss of vehicle controllability [1]. This phenomenon is well known, due to nonlinearity and uncertainty between tire/road friction force and wheel slip. The friction force at the tire/road interface is the main mechanism for converting wheel angular acceleration or deceleration into forward acceleration of deceleration (longitudinal force). The first solutions to improve braking efficiency simply consisted in preventing wheel-lock and to ensure steerability of the vehicle by means of Anti-lock Braking Systems (ABS). ABS intends to prohibit wheel-lock and skidding during braking by regulating the pressure applied on the brakes, increasing lateral stability and steerability, especially in wet and icy road conditions.

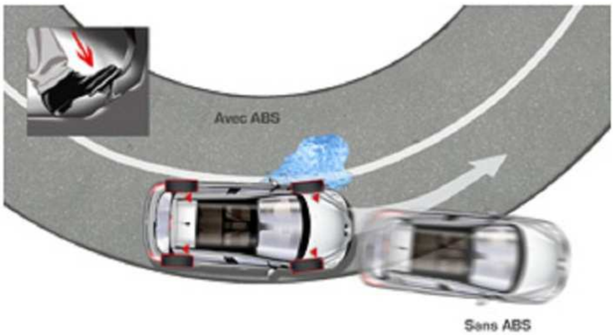


Figure 2.1 ABS activates during cornering and braking, with (avec) and without (sans) ABS

The control strategy was quite simple at the beginning: the braking effort was increased or reduced based on the analysis of the dynamical behaviour of the wheel. Such systems were far from perfect, because they produced noticeable vibrations. In addition, strong oscillations of the brake level were harmful to the friction force maximization. Consequently many theories and design methods have been proposed for decades, focused on ABS improvements according to [31].

## 2.2 Anti-lock Braking System Control

ABS control has to limit the longitudinal slip in order to maintain steerability and lateral stability during heavy braking. There are extremely difficult situations for ABS control where tire characteristics do not present a sharp maximum at a limited slip. Therefore an alternative ABS controller is proposed to handle extremely difficult situations.

### 2.2.1 Introduction Feed-Forward Braking Control

Initially this forms the main ABS control to test during this thesis project, but due to practical problems during research the assignment description is adapted. The basics of the Feed-Forward Control will be explained. One of the alternative ABS controllers is the Feed-Forward Braking Control, first introduced by Vermeer [16] and further developed by De Vries et. al. [15], and patented by Fehn et. al. [17]. The Feed-Forward Braking Control is based on a quarter car model with the LuGre tire model. The single wheel with the tire model is inverted. It is a brake actuation algorithm for each individual wheel, which can respond to both driver inputs and artificial vehicle deceleration set points. Optimal behaviour of the vehicle under braking is ensured by the feed forward control within the brake actuation algorithm. The highest achievable brake force will be reached in the shortest amount of time. This will lead to a minimal braking distance and no wheel lock [11], [15], [23].

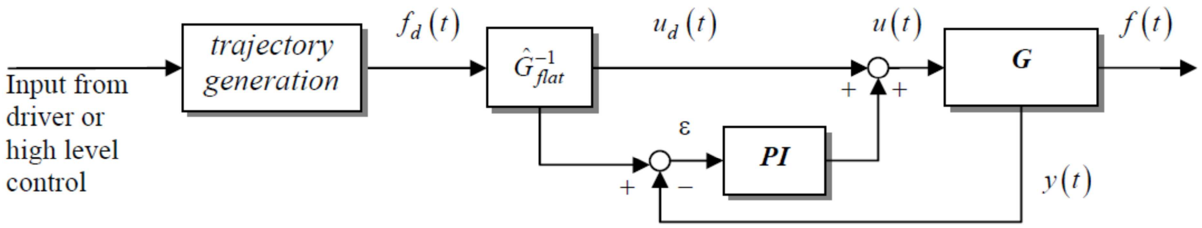


Figure 2.2 Procedure of Feedforward Control including feedback according to [23]

The plant shown in figure 2.2 is denoted by block G with input $u(t)$ and output $y(t)$ this is based on a ¼ car with LuGre tire model. Flat output $f(t)$ is a specific output of $G$, based on this flat output, a flat input is needed to inverse model $\hat{G}$ into $\hat{G}_{flat}^{-1}$. The plant input $u_d(t)$ can be calculated based on the desired response given by $f_d(t)$. All inputs such as the vehicle speed and its first three derivatives need to be continues and therefore the driver input has to be filtered. Earlier analysis reported in [11] showed that a real poles filter should be used.

## Quarter Car with LuGre tire model

For designing and testing braking control algorithms, a simple but effective quarter-car model is typically used, the model looks like figure 2.3. For this analysis the lumped LuGre Tire model is included to determine the brake force.
The model is given by the following equations:

$$m\dot{v} = -F_x$$
$$I\dot{\Omega} = r_e F_x - T_b \qquad (1)$$

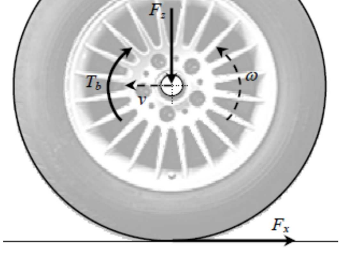


Figure 2.3 Quarter-car model

Where $\Omega\ (=\omega)\left[\frac{rad}{s}\right]$ is the angular speed of the wheel, $v\left[\frac{m}{s}\right]$ is the longitudinal speed of the vehicle, $M_b(=T_b)\ [Nm]$ is the brake torque, $F_b\ (=F_x)\ [N]$ is the longitudinal road-tire contact force, $I\ [kg\,m^2]$ is the momentum of inertia of the wheel, $m\ [kg]$ is the quarter-car mass and $r_e\ [m]$ is the effective wheel radius respectively. The dynamic behaviour of the system is hidden in the expression of $F_b[N]$, depending on the state variables $v\left[\frac{m}{s}\right]$ and $\Omega\left[\frac{rad}{s}\right]$. According to the LuGre tire model, the brake force $F_b[N]$ depends on the relative velocity $\upsilon_r=(\upsilon_x-\Omega\, r_e)\left[\frac{m}{s}\right]$ [1], [23]. The lumped LuGre tire model has an internal friction state $z$ which represents the deformation. 'Convection-loss' forms the difference between a standing, rolling and a slipping tire. This loss is included by means of $\kappa$ [23] to equivalent the distributed LuGre model. As a nonlinear differential equation it is describing the time varying deformation of the contact patch:

$$\dot{z}=\upsilon_r-\sigma_0\frac{|\upsilon_r|}{\mu(\upsilon_r)}z-\kappa\Omega\, r_e\, z \tag{2}$$

$$\mu(\upsilon_r)=\mu_C+(\mu_S-\mu_C)e^{-\left|\frac{\upsilon_r}{\upsilon_S}\right|^{\alpha_g}} \tag{3}$$

Vermeer proposed in [16] equation (4) as alternative for the exponential or Gaussian description (3) [23]:

$$\mu(\upsilon_r)=\mu_c+\frac{\mu_s-\mu_c}{1+\left(\frac{v_r}{v_{stribeck}}\right)^q} \tag{4}$$

The tire/road friction as function of the sliding velocity $\mu(\upsilon_r)$, is known as the Stribeck effect. The friction force in a contact point is:

$$F_b=(\sigma_0 z+\sigma_1\dot{z}+\sigma_2\upsilon_r)F_n \tag{5}$$

Where $\sigma_0$ is the normalized rubber longitudinal lumped stiffness, $\sigma_1$ the normalized rubber longitudinal damping, $\sigma_2$ the normalized viscous relative damping, $\mu_c$ the normalized Coulomb friction, $\mu_S$ the normalized Static friction, $(\mu_C\le\mu_S)$, $\upsilon_S$ and $v_{stribeck}$ are the Stribeck relative velocity, $\upsilon_r=(\upsilon-\Omega\, r_e)$ is the relative velocity, $\alpha_g$ respectively $q$ are the shaping factors, $F_n$ is the normal force and $z$ is the internal friction state. There is a special case, the steady-state tire characteristic: $v_x=v$ and the constant parameter $\alpha_g$ respectively $q$ can be used to capture the steady-state tire characteristic. Combining the LuGre tire friction description within the force equations, the equations of motion of model structure $G$ becomes:

$$m\dot{v}_x = -F_n\sigma_0 z \qquad (6)$$

$$I\dot{\Omega} = r_e F_n \sigma_0 z - M_b \qquad (7)$$

$$\dot{z} = v_r - \frac{\sigma_0 |v_r| z}{\mu(v_r)} - \kappa r_e \Omega z \qquad (8)$$

The term $-\frac{\sigma_0 |v_r| z}{\mu(v_r)}$ with $\mu(\upsilon_r)$ is the non-linearity of the limited tire/road friction according to [11], [23].

## Flatness-Based Model Inverse

The concept of flatness offers a way to parameterize the nonlinear dynamical behaviour of a system using flat outputs. The system is said to be flat if one can find a set of outputs (equal in number to the number of inputs) such that all states $x$ and inputs $u$ can be determined in differential functions of the flat output. When a system is flat, it is an indication that the nonlinear structure of the system is well characterized and one can exploit that structure in designing control algorithms for motion planning, trajectory generation and stabilization. A typical use of control theory in many modern systems is to invert the system dynamics to compute the inputs required to perform a specific task. The inverse dynamics problem assumes that the dynamics for the system are known and fixed [13], [18]. In case of Feed-Forward Braking control, the vehicle deceleration $\dot{v}_x$ at a given brake torque $M_b$ can be calculated with equations (6, 7 and 8) derived from the quarter car model. The inverse of this quarter car with LuGre tire model is used to get the desired deceleration (with sufficient derivatives of $\dot{v}_x$) as input and the required brake torque will be calculated, see figure 2.4. Due to non-linearities in the equations, the model is not simply invertible. The proof of flatness of the quarter-car with LuGre tire model can be found in [15], [23]. The equation for the desired brake torque becomes:

$$M_b = -r_e m \dot{v}_x - If\left(v_x, \dot{v}_x, \ddot{v}_x, \dddot{v}_x\right) \qquad (9)$$

Where $\dot{\Omega} = f(v_x, \dot{v}_x, \ddot{v}_x, \dddot{v}_x)$ is a function of the vehicle speed, acceleration, jerk and the third time derivative of the vehicle speed.

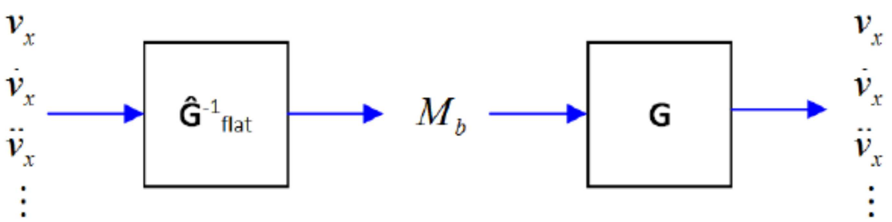


Figure 2.4 Representation of the relationship between the inverted flat system (left) and real system (right) [11]

## Trajectory Planning

In order to calculate the inverse, it is necessary to differentiate the flat output at least three times. The input of the inverted system, the flat output $f_d$, needs to be smoothened. A method to achieve from a steady state to the next requested state is trajectory planning [15], [23].

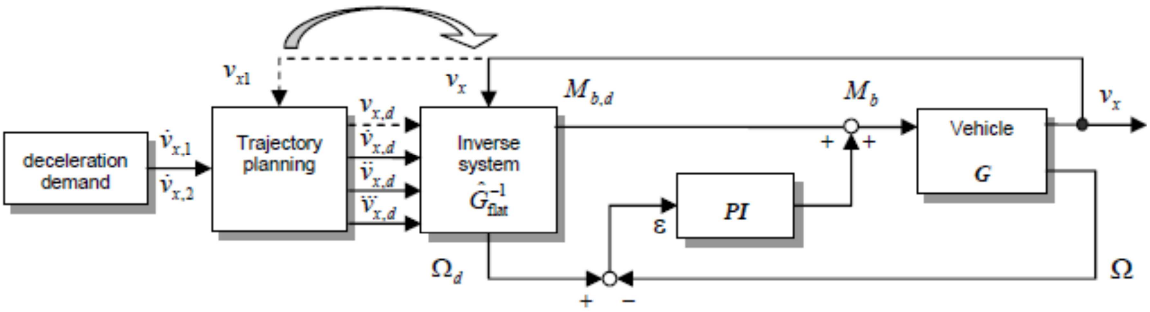


Figure 2.5 Calculation scheme with quarter car variables [23]

## 2.2.2 Previous research application Feed-Forward Braking

The used filter of the Feed-Forward Braking Control application in the VTL will shortly be described. This is done by Marien van Ditten and his work can be found in [11]. To be sure about the flat inputs to the inverse model, the trajectory planning have to be continues in the needed derivatives. A 4th order Real Poles filter is proposed by Marien van Ditten and explained in [11].

***Real Poles filter***:
A simple low pass filter is used with all its poles in the left half plane and on the same location. With this property the system provides a stable developed brake torque. This results into a less violent braking action with an improved time response, according to Marien van Ditten in [11].

$$H(s) = \left( \frac{1}{\frac{s}{\omega_0} + 1} \right)^4 \cdot \frac{1}{s} \qquad (10)$$

This proposed filter will be used during this research.

# Chapter 3
# Vehicle Test Lab and Data Acquisition

The Vehicle Test Lab (VTL) is used for testing several types of tire behaviour and for prototyping ABS strategies. Even if simulations show robust behaviour of controllers, the controllers' performance can be better observed in real life with this measurement setup. External disturbances on signals on the measurement setup are closer to a vehicle situation. Typical problems that are encountered in real life are delays, additive noise, drift, saturation and other system dynamics. The VTL is specifically suited to test and to see differences in performance between several developed ABS controllers.

## 3.1 Introduction VTL

The VTL of the Delft University of Technology (DUT) is located in the laboratory of the Mechanical, Maritime and Materials Engineering (3ME) faculty. The VTL consists of three parts; the basement, the measurement setup and the control room.

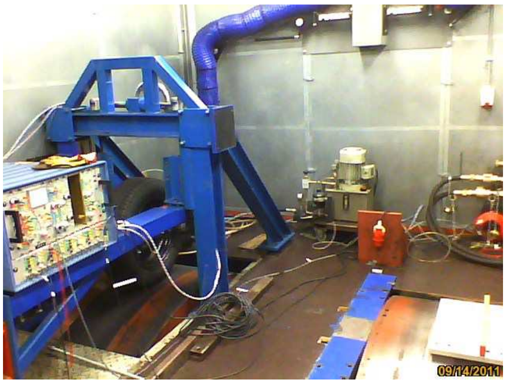


Figure 3.1 VTL measurement setup the control room

The basement contains a large rotating steel drum, which has a diameter of 2.5 meter. It is used to simulate the road and is the powertrain of the test wheel on top of it. Two steel drums are coupled to a gear box and powered by a 3-phase electromotor. In the measurement setup the test wheel is connected with the drum, which has sand-paper on it, intended to increase the friction coefficient and to decrease the slip sufficiently in between the wheel and drum. The axle of the wheel is supported in a frame by two bearings, on each side of the wheel one, see figure 3.3.



Figure 3.2 Setup of the wheel fixed in a frame the caliper with compressed air cooling

The frame is equipped with several sensors. To measure the force in x, y, z direction, the bearing housings are connected to the fixed frame by piezoelectric force transducers. In the axle of the wheel strain gauges are placed to measure the brake torque. Incremental encoders are used to measure the wheel and drum speed, which allows a precise estimation of the longitudinal slip. At the end of the axle is a hydraulic disc brake mounted, the brake pressure in the caliper is measured by a piezoelectric transducer.

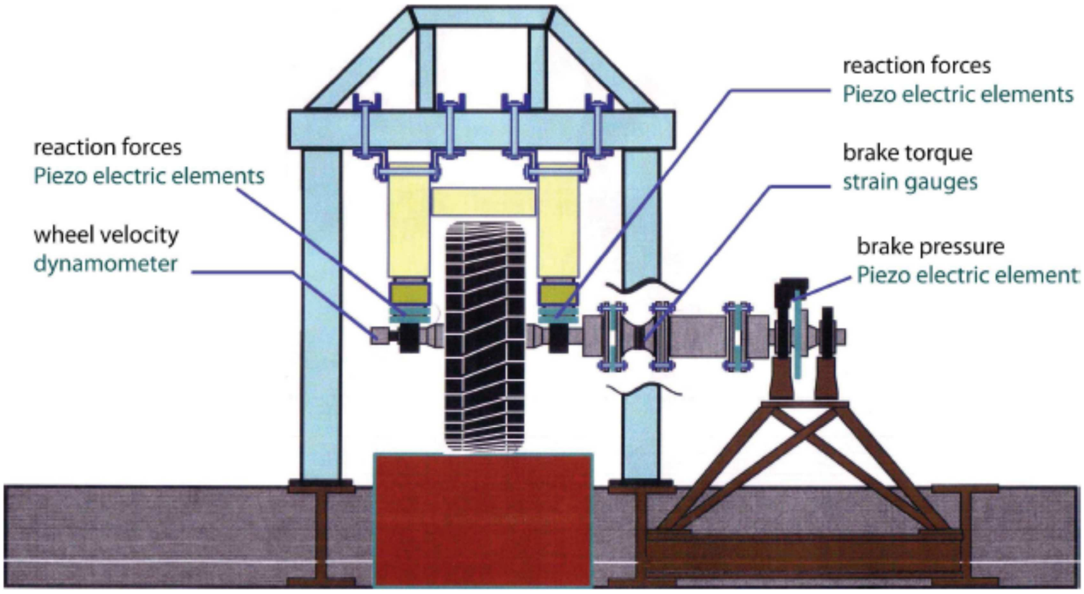


Figure 3.3 Measurement setup for tire and ABS control experiments, several sensors are implemented for sensing the wheel and brake dynamics. [7]

Figure 3.4 shows the interaction between the drum and the wheel, whereby the wheel in a fixed frame is powered by the rotating drum. This is in contrast to a moving vehicle on a stationary road, but does not affect the test results by defining the reference frame. But there is still something different with a vehicle situation, normally the engine torque is provided to the wheel by its axle and through tire dynamics connected to the road. In case of the measurement setup, the engine torque provided by the drum will be delivered as a force $F_x$ and the tire dynamics influences the wheel velocity. The difference between the vehicle situation and measurement setup can be neglected if the drum inertia is equivalent with the (quarter) vehicle mass.

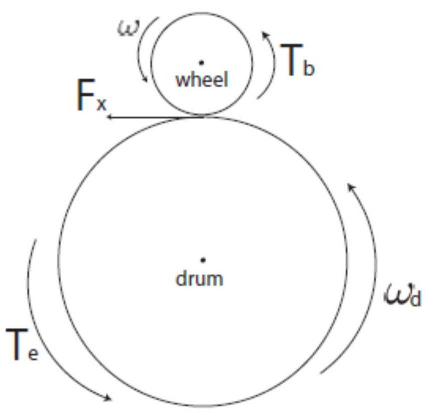


Figure 3.4 Forces, torques and the angular speeds of the drum and wheel. [7]

To control the brake caliper, a hydraulic pump, hydraulic line and an actuating servo-valve is used (see figure 3.5). These components limit the performance of the brake actuation. The controlled actuating valve will introduce a damped second-order (mass-spring) dynamics and a flow rate limit, the hydraulic line causes a transport time delay between the desired and the actual brake pressure.


Figure 3.5 hydraulic pump with by-pass valve

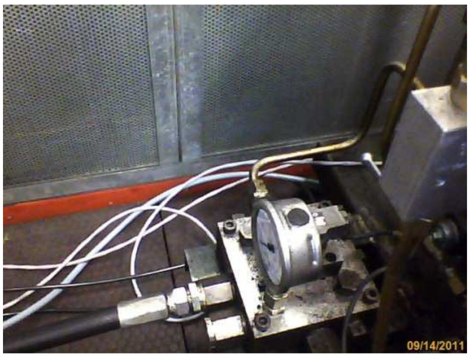


hydraulic line and the ABS servo-valve

From the control room the powertrain is controlled by sending a reference drum velocity signal. The frequency converter receives a signal and converts it into a 3-phase AC current which powers the electromotor. The electromotor is connected with a transmission and on its turn coupled to the drum. The rotational speed of the electromotor is controlled by using backward EMF and the attached hollow shaft encoder sends pulses to the control room [7].

Figure 3.6 the disc brake

piezoelectric transducer of the hydraulic pressure

The brake setup is controlled by sending a reference brake pressure signal. The servo-valve is actuated by this signal and on its turn it actuates the caliper hydraulically. The actual hydraulic pressure of the caliper is measured by a piezoelectric transducer. A small charge amplifier receives the piezoelectric signal from the piezoelectric transducer (see figure 3.6) and converts mechanical tension into an electric signal that represents the actual pressure. The analog control unit receives the measured brake pressure and send the actual brake pressure. Other signals like the brake torque, sensor signals from the force, wheel velocity; (sensor signals in figure 3.7) are also send to the control room. In appendix A-1 the sensors and belonging signals can be found in table A-1 VTL sensor signals.

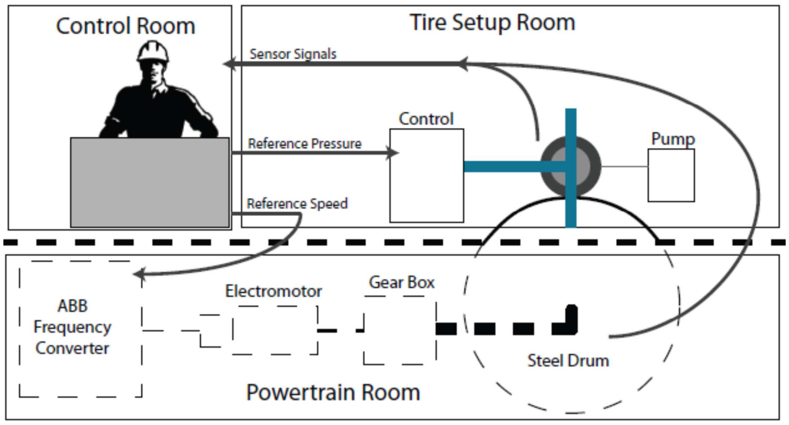


Figure 3.7 VTL: rooms; the control room, basement and the measurement setup. The basement (powertrain room) and measurement setup are controlled by software and signal actuation from the control room.
The basement contains the powered drum which simulates the road.
The measurement setup is equipped with wheel dynamics, brake hydraulics and its sensors. [7]

## 3.2 VTL Modifications

Because of research of Marien van Ditten, reported in [11], it is thought to modify the VTL by replacing the rubber brake hose with a stainless steel braided brake hose with a decreased diameter. This a relative simple change, to identify the possible effects on the brake pressure dynamics. Compared to the relative big rubber brake hose, the stainless steel braiding provides an increase in stiffness of the side wall and the decreased diameter. There will be a decrease in expansion during the brake pressure rise and an increase in compressing due to a smaller hose diameter. Due to the two mentioned effects, the brake pressure rise will be steeper. It should result into improved brake pressure dynamics. Thus improving the of-tracking of the desired brake torque and eventually improve the response time, but it is a hypothesis.

Figure 3.8 examples of stainless steel braided brake hoses
[Source: Goodridge]

Other modifications after the brake hose replacement could be:
1. Adjustment of the proportional gain of the big proportional control unit.
2. Checking if the reference pressure is calculated or measured.
3. Checking the effect of a filtered reference brake pressure.
4. Checking the effect of several cross-over frequencies.

This will lead to a different setting between the desired and measured value by the design improvement situation.

**Modified VTL with a stainless steel braided brake hose**

Figure 3.9 view new brake hose, silver-metal coloured and pointed by red arrows

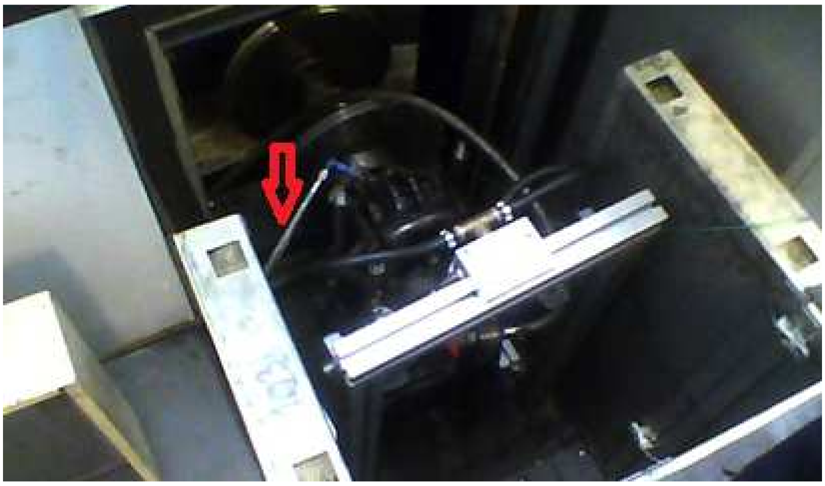

Figure 3.10 view new hose on the brake setup

Figure 3.11 view new hose mounted on the brake caliper

## 3.3 dSPACE Layout

The control room of the VTL is equipped with dSPACE data acquisition equipment, to link control functions and modelled dSPACE software to the experimental setup. In the VTL is the dSPACE type DS1103 used and consists of a controller board and a connector panel. Two actuator signals and ten measurement signals are linked to this connector panel. A Simulink block diagram, which is a platform of Matlab, is used to program the controller board fully in addition with a Real-Time Interface (RTI). Figure 3.12 shows a Simulink block diagram which represents the VTL control of the specific ABS system. The dSPACE input signals on the left as the dSPACE output signals on the right are connected to the connector panel. Within these blocks scaling factors convert the voltage received into a physical value and vice versa. The dSPACE connector blocks have a maximum dimensionless range in between ±1 [-] which represents a voltage range in between ±10 [V], on its turn a brake pressure range in between 0-100 [bar]. All signals should be scaled to this dimensionless range in order to obtain an optimal resolution. A list of scaling values can be found in table A-4. Considering the dSPACE simulation settings, there is a wide variety of choices such as the solver method and the sampling time. The solver method has to be set to the preferred dSPACE settings, a discrete-time first-order Euler method with an infinite running time. For a more accurate control, the sampling time is set on 1ms.

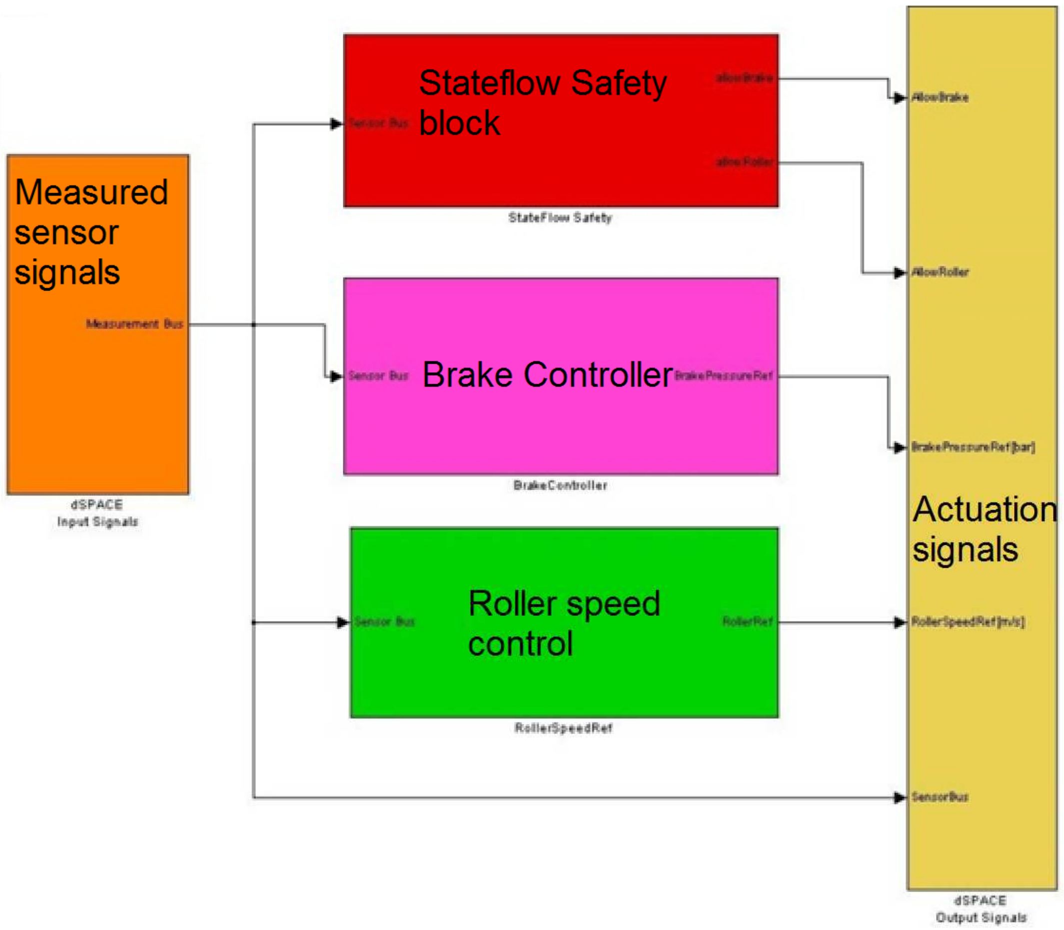


Figure 3.12 an example of a VTL control block diagram from Simulink in dSPACE

## 3.4 dSPACE applications

To perform brake pressure measurements, first a Simulink brake controller model has to be made. This brake controller model contains all control equations and calculations which are coming from a theoretical ABS controller model. In order to consume less time in building a brake controller model, an existing Feed-Forward ABS model is used as figure 3.13 shows. The blue block is the main part of the Feed-Forward control and this part is modified by a signal generator with a constant block in Simulink to actuate the control (servo) valve. By actuating the control (servo) valve and measuring the actual brake pressure, the difference can be monitored real-time. To monitor the brake pressure process, a control panel has been made within dSPACE ControlDesk. Several graphs, buttons, sliders, settings and the data acquisition can be chosen and the control panel design, like the location and shapes of the buttons and graphs is up to your own fantasy. It is important to choose the exact parameters and its dimensions which are needed to measure. In the Simulink brake controller model the parameters can be found in the block diagram and in the dSPACE ControlDesk the same parameters can be seen in a list.

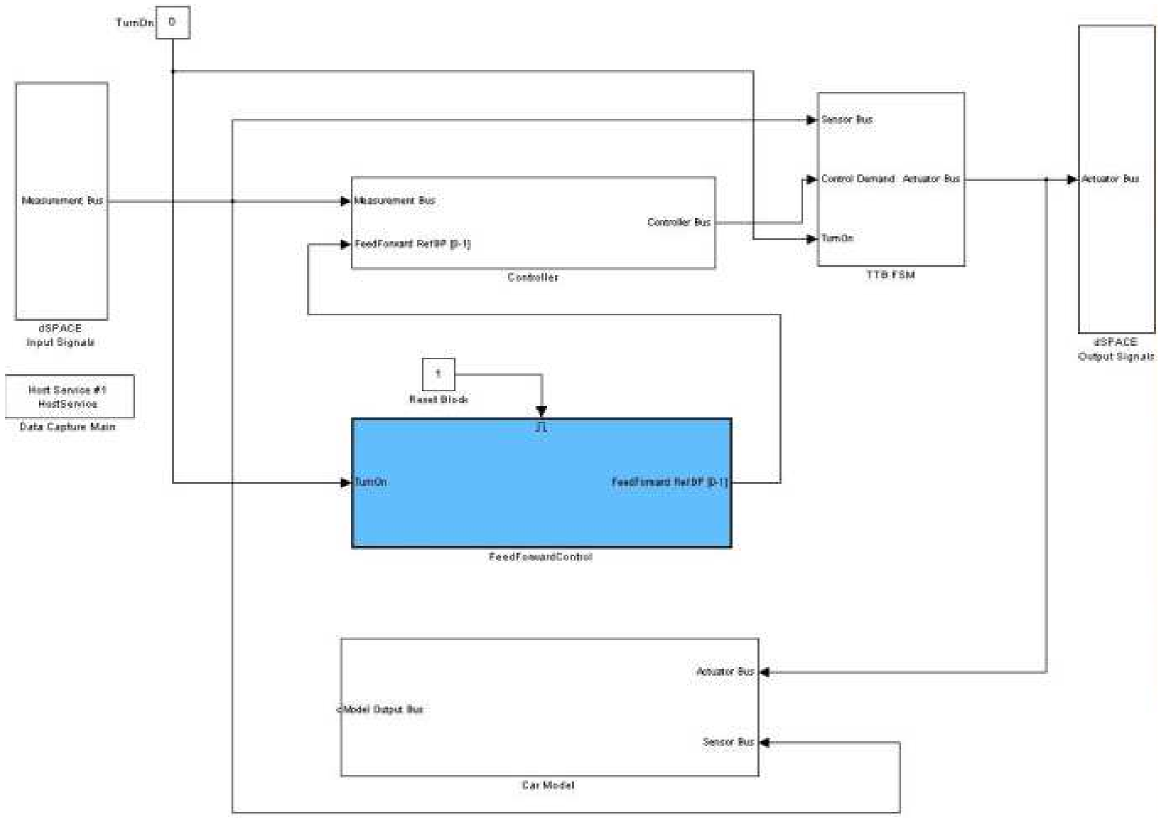


Figure 3.13 Highest level of the Feed-Forward ABS block diagram from Simulink in dSPACE

Clicking the mouse cursor on the blue block, which is the Feed-Forward control, its block diagram will be exposed as shown in figure 3.14. More parts and details of the controller can be seen. Clicking on each part will display the parameter settings.

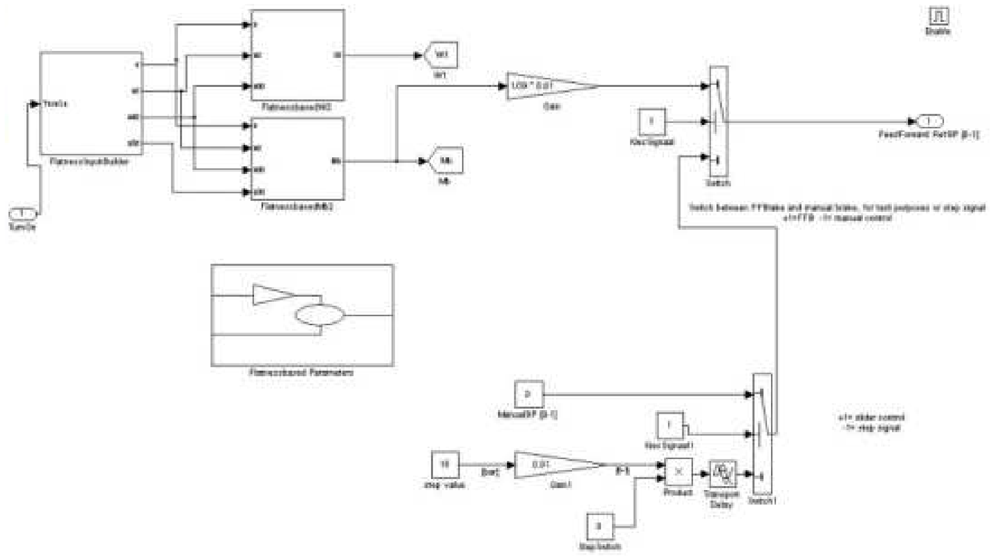

Figure 3.14 The Feed-Forward Control block diagram within the blue Simulink block of figure 3.13

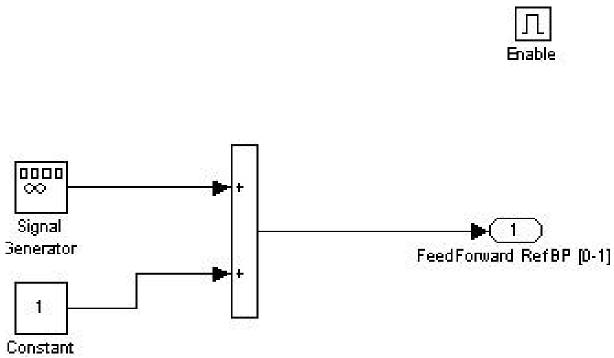


Figure 3.15 The Feed-Forward Control block diagram of figure 3.14 is replaced by a signal generator and a constant

To analyse the brake actuation performance, static brake pressure analysis is done by approaching it with a sinus wave actuation. This is realized by replacing the Feed-Forward control by a signal generator and a constant block, as shown in figure 3.15. The constant block is the part in which the desired pressure is set and the signal generator is sending the predefined wave signal varying around the constant average brake pressure value. Earlier sinus wave excitation measurements show a decrease in maximum brake pressure of 100bar at low frequencies.
In order to check the actual brake pressure of channel 5, a filtered analog reference pressure is added at channel 6, which is normally a free channel. This check is done to see if the actual brake pressure signal of channel 5 is natural as expected or is adapted by filters. In chapter 5 the result of channel 6 can be found. Figure 3.16 show the added actual brake pressure signal on channel 6.

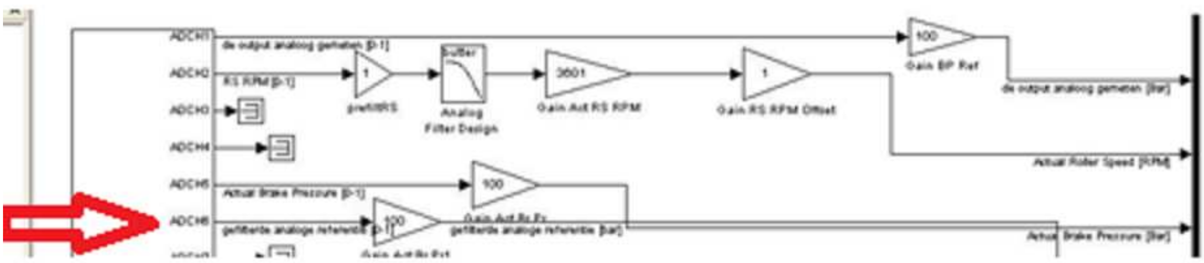

Figure 3.16 Channel 6 (red arrow) is added to check the actual brake pressure signal of channel 5

# Chapter 4
# Experimental Validation

Before experimenting on the VTL, some precautions have to be made. This can be done by modelling a system to get references or doing some measurements of the actual system if references are known. In this case the VTL brake setup has to be modified before doing some ABS controller measurements. Previous work of Marien van Ditten in [11] did several measurements to identify the problem of the brake setup. Due to delays during my thesis research, the research will focus on the system identification of the VTL measurement setup instead of testing ABS controllers.

## 4.1 VTL setup limitations

The actual VTL measurement setup has a disadvantage for testing ABS controllers. Van Ditten noticed that the actual maximum brake force and therefore the maximum brake torque are much too low. The brake torque did not reach its maximum within the desired time internal according to his measurements. To check if setup parts influenced the test results, the brake pads were replaced, the brake line was bleeded and the actuator gain was increased. But the problems remain the same. Due to this fact there were Fourier analysis done to check the measurement setup frequency responses (Fast Fourier Transforms). Zegelaar reported in [4] an experimental modal analysis of a free non-rotating tire to validate the modes of his tire model in the TU Delft VTL. The three modes showed to be in a frequency range of 0-80Hz. However Van Ditten shows in [11] test results with a bandwidth of about 20 Hz. Van Ditten concluded that the problems probably are within the flow rate limit of the control valve and the pressure build-up in the brake line.

## 4.2 Static brake pressure method

In order to see the effects about the brake pressure losses, static brake pressure measurements are done. Of-tracking a non-linear system as a local linear system will simplify the brake pressure measurements and the pressure losses become quick visible. The static method is based on exciting the brake pressure by a sinus wave with different frequencies and amplitudes, to identify the whole hydraulic system. This is including the brake line, the flow rate limit of the control valve and the movements of the caliper. By replacing the brake hose, relative simply static brake pressure measurements are possible. These measurements are able to show differences in brake pressure dynamics without the temperature dependent friction of the brake disc and pads, the viscosity of brake fluid and the dynamic tire behaviour during dynamic pressure measurements. Another advantage is the repeatability and therefore the reliability of the static measurements against the dynamic measurements.

## 4.3 Static brake pressure test description

The brake pressure measurements are achieved by setting the desired pressure, selecting the wave form with its amplitude and frequency around the constant average value in the ControlDesk panel before the measurements are taken. Most important VTL equipment for the static measurements is switched on, except the voltage supply of the by-pass valve. Before a test can be done, the charge amplifier has to be reset by a switch to calibrate at zero bar. This allows comparing several tests with each other. A measurement can be started by clicking on "Start" of the data acquisition panel followed by switching on the voltage supply of the by-pass valve. In the output graphs of the dSPACE ControlDesk panel the brake pressure rise is visible before the actual pressure of-tracking the desired pressure. Any difference between the output and the input indicates about the brake pressure dynamics. The duration of each test takes twenty seconds and each measurement contains two tests to see the brake pressure effects after the first test. In the data acquisition panel test data is saved on a pre-defined folder. The brake pressure data is converted into Excel sheets, to display the actual and reference brake pressure versus the time graphs. To show the brake pressure differences, the data can be compared in many ways. In Appendix A-3 the brake pressure measurement sequence description can be found. Appendix A-4 describes the dSPACE ControlDesk measurement sequence. Appendix A-5 shows the data preparation order form dSPACE to Excel.

## 4.4 Repeatability static brake pressure results

First the repeatability of the original situation including the rubber brake hose, the constant average **50bar** with varying amplitude of **10bar** @ **0.1Hz** measurements are taken into account. As a first example, measurements of two identical tests are compared. The amount of data are coming from the 40 and 60 bar values, 1328 data points showed to be sufficient at this frequency. 1328 Data points at 40, 50 and 60bar of both tests are compared; these three pressure areas are taken to see the deviations. From the top, bottom and middle pressure values ±664 data points are taken. The maximum deviations are computed by Excel. This method shows in which way the deviations are constant.

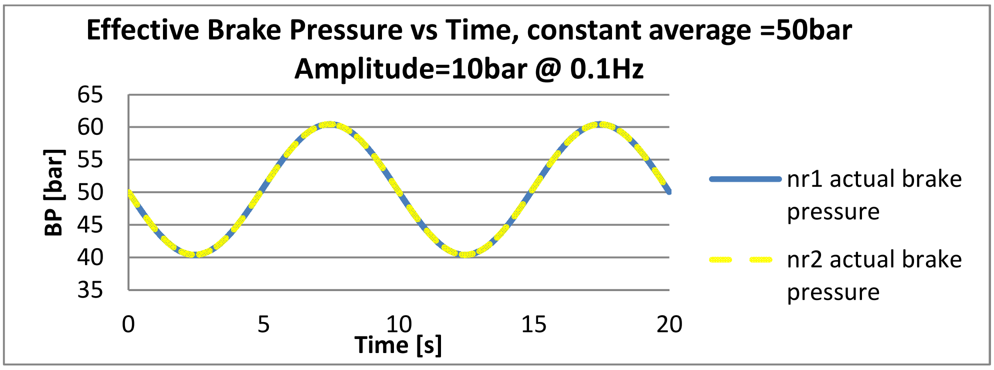


Figure 4.1 The actual brake pressure nr1 and nr2 results to check the repeatability

| [bar] | 50,00 | 40,00 | 50,00 | 60,00 | 50,00 | 40,00 | 50,00 | 60,00 |
|---|---|---|---|---|---|---|---|---|
| max | 0,29 | 0,09 | 0,31 | 0,04 | 0,31 | 0,11 | 0,27 | 0,06 |
| % | 0,58 | 0,23 | 0,62 | 0,67 | 0,62 | 0,28 | 0,54 | 1,00 |

Table 4-1 maximum deviations in [bar] and [%] between two identical tests
Constant average 50bar, A=10 bar @ 0.1Hz

The repeatability results are presented in table 4-1. The deviations of the 40 and 50 bar are comparable to the values of the two other 40 and 50bar. The 60bar results have a difference of 0,02 bar and 0,38% respectively. This difference seems to be large, but such difference is also seen with the 40 and 50bar values. Based on the results this measurement is repeatable. To check the repeatability at other situations, the same is done with **80bar** with varying amplitude of **20bar at 1 Hz**.

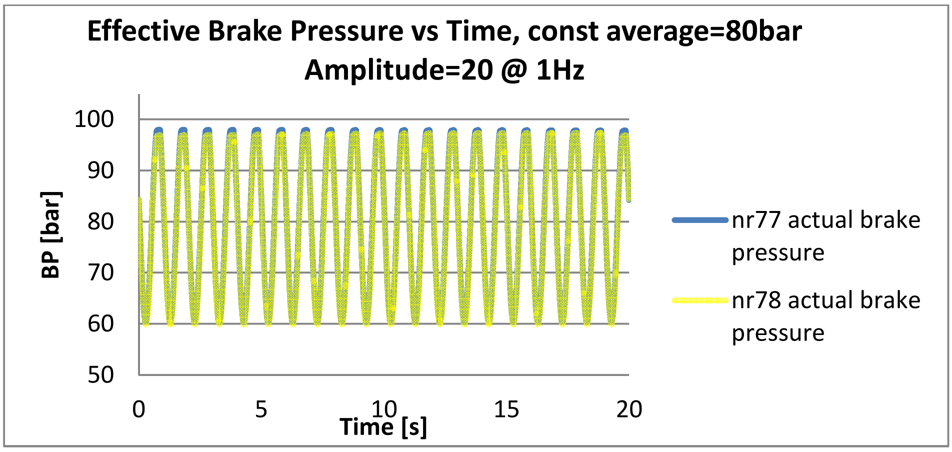


Figure 4.2 the actual brake pressure nr77 and nr78 results to check the repeatability

| [bar] | 60,00 | 80,00 | 97,00 | 80,00 | 60,00 | 80,00 | 97,00 | 80,00 |
|---|---|---|---|---|---|---|---|---|
| max | 2,11 | 3,05 | 4,07 | 4,41 | 2,13 | 3,06 | 4,14 | 4,41 |
| % | 3,52 | 3,81 | 4,19 | 5,51 | 3,55 | 3,83 | 4,27 | 5,51 |

Table 4-2 maximum deviations in [bar] and [%] between two identical tests of the last 2 whole waves
Constant average 80bar, A=20 bar @ 1Hz

The second repeatability test is done at a constant average of 80bar with a varying amplitude of 20bar @ 1Hz (see figure 4.6), in the same way as the previous repeatability tests. Compared to the previous result here are more waves involved due to 10 times higher frequency. Less data is within a small amount of time of one wave to focus on. The following consequence is taking ± 200 data points at each pressure value instead of ± 664 data points of the previous repeatability test. The repeatability results are taken from the last two whole waves. The results of table 4-2 show also an iterating deviation, with much higher differences than the results of table 4-1. This caused by the increased frequency, constant average pressure and amplitude. The results of measurement nr 77 and nr 78 show a comparable repeatability as measurement results nr 1 and nr 2. Based on the repeatability test, there can be concluded that this method of measuring the brake pressure of the VTL is repeatable, if relative small varying amplitude around a relative high constant average pressure is chosen. Reaching the maximum pressure values becomes difficult due to pressure dynamics and may vary more than the other lower pressure values.

## 4.5 Static brake pressure results original situation

Earlier measurements showed a significant decrease in brake pressure dynamics at its maximum reaching pressure. To see the effects for reaching its maximum, the following measurements are done with low as high frequencies with different amplitudes.

***Original situation with rubber brake hose:***

Most important to monitor is the maximal reaching brake pressure and possibly phase shifts between the actual and reference brake pressure. First observing the situation of measurement nr 8, see figure 4.7

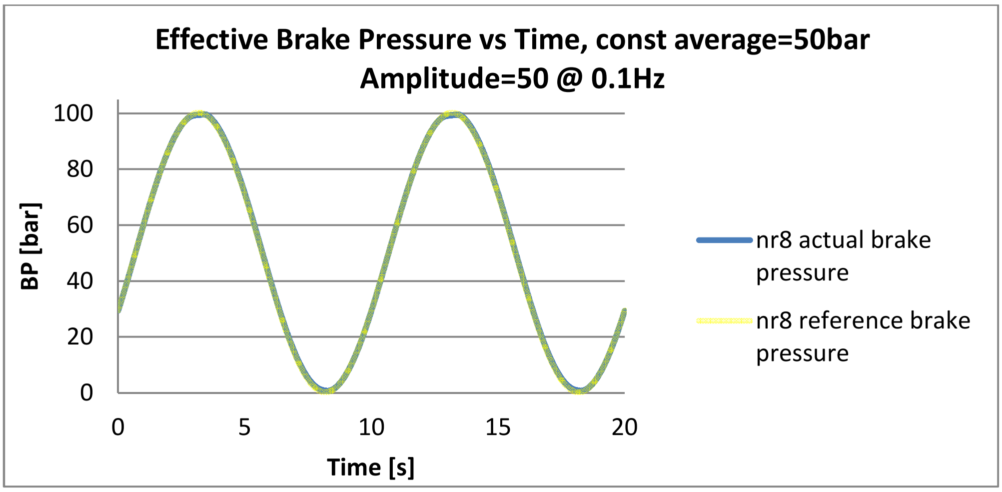


Figure 4.3 the deviation between the actual and reference brake pressure nr8 results

| [bar] | 50,00 | 100,18 | 50,00 | 0,18 | 50,00 | 100,18 | 50,00 | 0,18 |
|---|---|---|---|---|---|---|---|---|
| max | 0,09 | 0,65 | 0,47 | 0,53 | 0,10 | 0,78 | 0,47 | 0,56 |
| % | 0,18 | 0,65 | 0,94 | - | 0,20 | 0,78 | 0,94 | - |

Table 4-3 maximum deviations in [bar] and [%] between the actual and reference brake pressure nr8 Constant average 50bar, A=50 bar @ 0.1Hz

Both pressure peaks are concerned to check the deviation between the reference and actual pressure. The first peak shows a maximal deviation of 0,65 bar. While the second peak shows a maximal deviation of 0,78 bar, see table 4-3. This can be caused by fluctuation within the accuracy of the whole measurement set up. The curves of both peaks of the actual pressure at its maximum are oblique shaped compared to the reference pressure. Pressure dynamics are influenced when reaching the maximum pressure with large amplitudes

The next results of measurement nr 47 are with the settings: *constant average 80bar, amplitude of 10bar @0.1Hz*, see figure 4.4. In this case the reference pressure curve is lower than the actual pressure. The lower reference is caused by the lower reference pressure setting in the ControlDesk panel. It is not clear why the actual pressure curve show higher values than the reference pressure. In Matlab the same phenomenon can be seen. Table 4-4 shows decreased top-top values, this is also coming from the slider constant average value setting in ControlDesk.
Compared to the previous results of nr 8, the deviations of measurement 47 are in the order of 0,3 to 0,4 and shows a more stable progress. This improved pressure dynamic behaviour is caused by the much lower amplitude.
The same pressure dynamics check is done with a frequency increase to 1Hz, showed in figure 4.9. Again in this situation the reference pressure curve is lower than the actual pressure. Table 4-5 shows increasing the frequency, results into comparable deviations as table 4-4. This parameter change is not affecting the pressure dynamics.

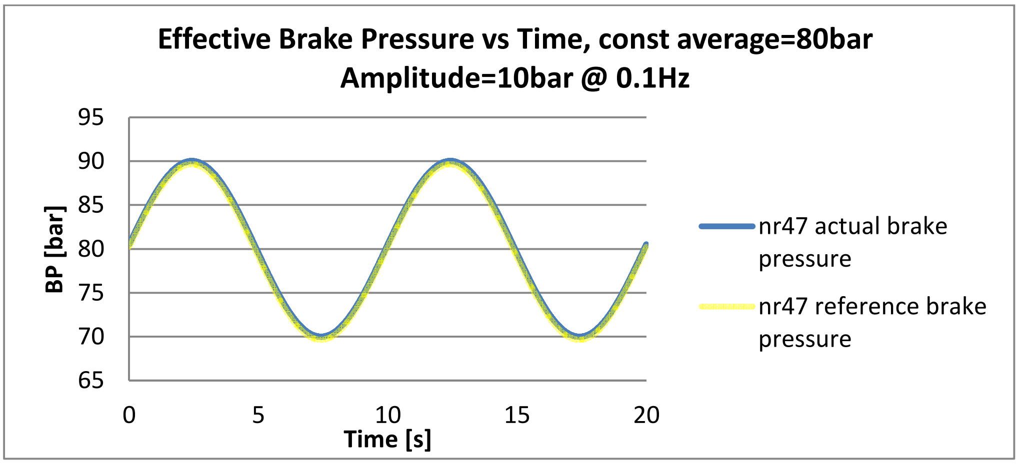

Figure 4.4 the deviation between the actual and reference brake pressure nr47 results

| [bar] | 80,00 | 89,65 | 80,00 | 69,65 | 80,00 | 89,65 | 80,00 | 69,65 | 80,00 |
|---|---|---|---|---|---|---|---|---|---|
| max | 0,29 | 0,38 | 0,43 | 0,33 | 0,28 | 0,35 | 0,42 | 0,33 | 0,27 |
| % | 0,36 | 0,42 | 0,54 | 0,47 | 0,35 | 0,39 | 0,53 | 0,47 | 0,34 |

Table 4-4 maximum deviations in [bar] and [%] between the actual and reference brake pressure nr47 Constant average 80bar, A=10 bar @ 0.1Hz

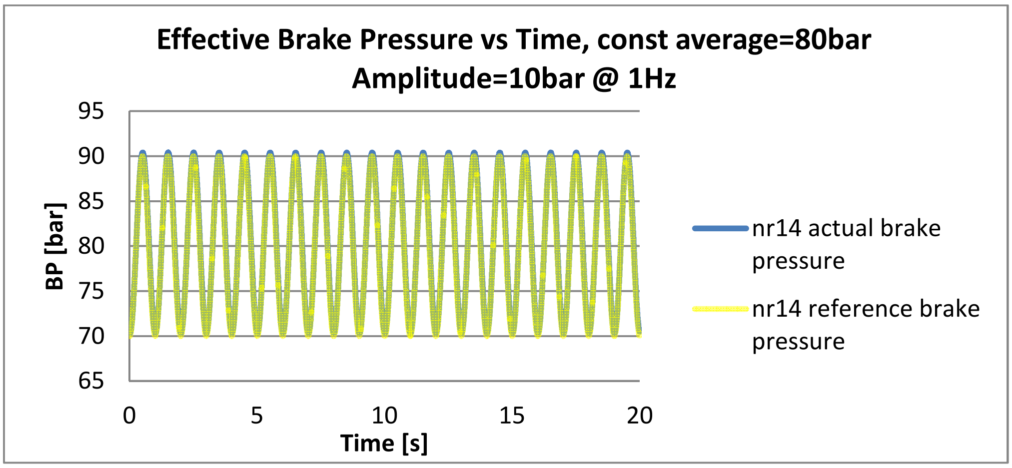

Figure 4.5 the deviation between the actual and reference brake pressure nr14 results

| [bar] | 70,00 | 80,00 | 90,00 | 80,00 | 70,00 | 80,00 | 90,00 | 80,00 | 70,00 |
|---|---|---|---|---|---|---|---|---|---|
| max | 0,35 | 0,08 | 0,35 | 0,78 | 0,34 | 0,07 | 0,36 | 0,76 | 0,34 |
| % | 0,50 | 0,10 | 0,39 | 0,98 | 0,49 | 0,09 | 0,40 | 0,95 | 0,49 |

Table 4-5 maximum deviations in [bar] and [%] between the actual and reference brake pressure nr14 of the first two waves, Constant average 80bar, A=10 bar @ 1Hz

Figure 4.10 shows the brake pressure results from the *constant 80bar amplitude of 20bar* @ 0.1Hz situation. Compared with the measurement of nr 47, see figure 4.4, the amplitude is increased with 10bar. The results of nr 49 have an increase in deviations. Also shows the peaks to be oblique shaped like measurement nr 8, an amplitude of 20bar is already influencing the pressure dynamics at its maximum.

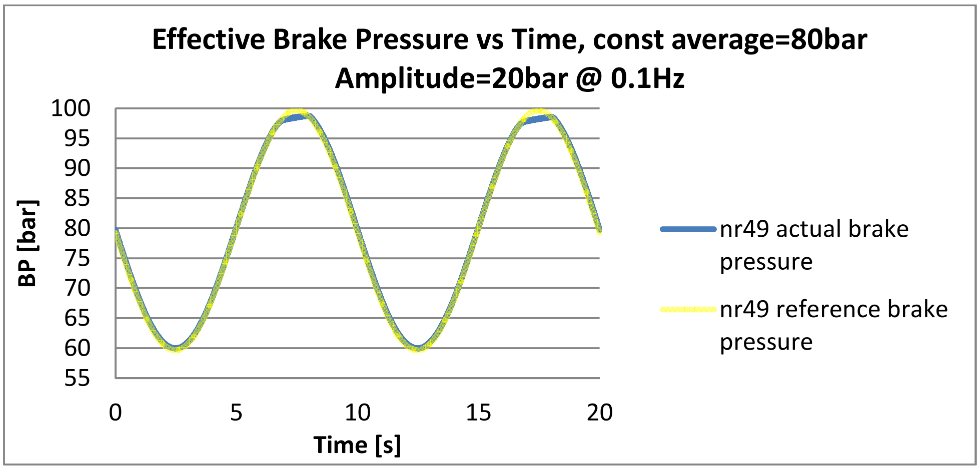

Figure 4.6 the deviation between the actual and reference brake pressure nr49 results

| [bar] | 80,00 | 60,00 | 80,00 | 100,00 | 80,00 | 60,00 | 80,00 | 100,00 | 80,00 |
|---|---|---|---|---|---|---|---|---|---|
| max | 0,48 | 0,34 | 0,21 | 1,09 | 0,48 | 0,31 | 0,21 | 1,38 | 0,48 |
| % | 0,60 | 0,57 | 0,26 | 1,09 | 0,60 | 0,52 | 0,26 | 1,38 | 0,60 |

Table 4-6 maximum deviations in [bar] and [%] between the actual and reference brake pressure nr49 of the first two waves, Constant average 80bar, A=20 bar @ 0.1Hz

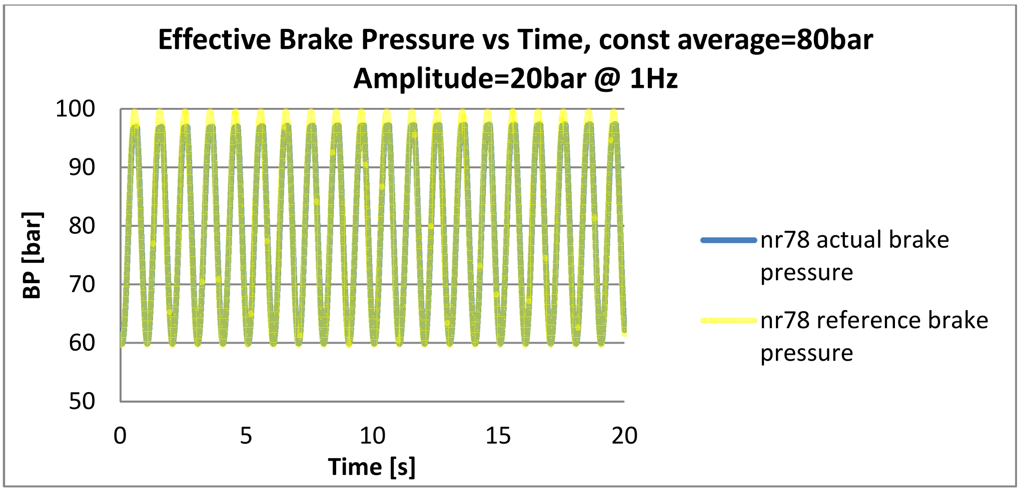

Figure 4.7 the deviation between the actual and reference brake pressure nr78 results

| [bar] | 59,65 | 80,00 | 99,65 | 80,00 | 59,65 | 80,00 | 99,65 | 80,00 | 59,65 |
|---|---|---|---|---|---|---|---|---|---|
| max | 0,24 | 1,23 | 2,87 | 1,32 | 0,25 | 1,22 | 2,84 | 1,33 | 0,25 |
| % | 0,40 | 1,54 | 2,88 | 1,65 | 0,42 | 1,53 | 2,85 | 1,66 | 0,42 |

Table 4-7 maximum deviations in [bar] and [%] between the actual and reference brake pressure nr78 of the first two waves, Constant average 80bar, A=20 bar @ 1Hz

In measurement nr 78 the frequency is increased to 1Hz compared to nr 49. This results into an increase of the deviations. The relative high amplitude of 20 bar influences the pressure dynamics, compared to measurement nr 14. Figure 4.8 to 4.10 shows a visible pressure drop when the frequency s increased more. Figure 4.8 shows a deviation of the actual and reference pressure of about 8bar with an increased to 8Hz. Up to 10Hz the deviation is about 12bar. Increasing to 15Hz, the deviation is about 15bar, see figure 4.10.

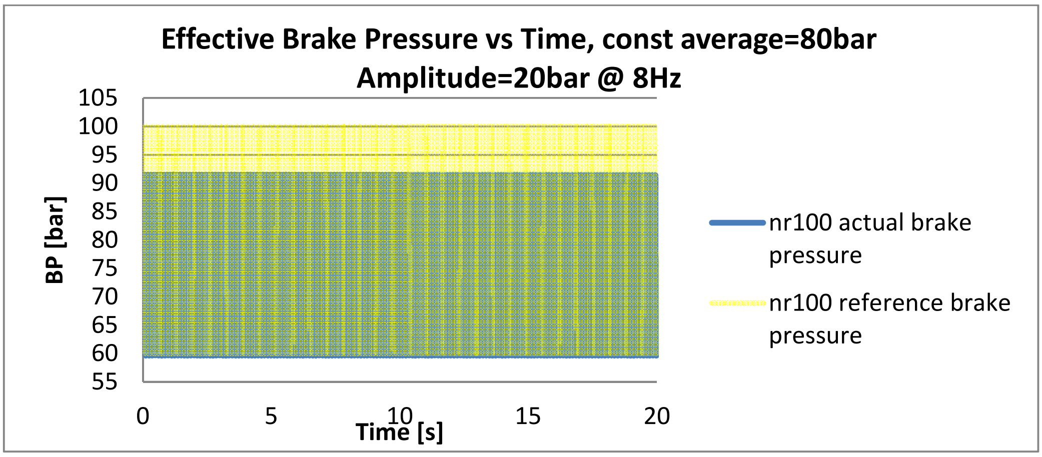


Figure 4.8 the deviation between the actual and reference brake pressure nr100 results

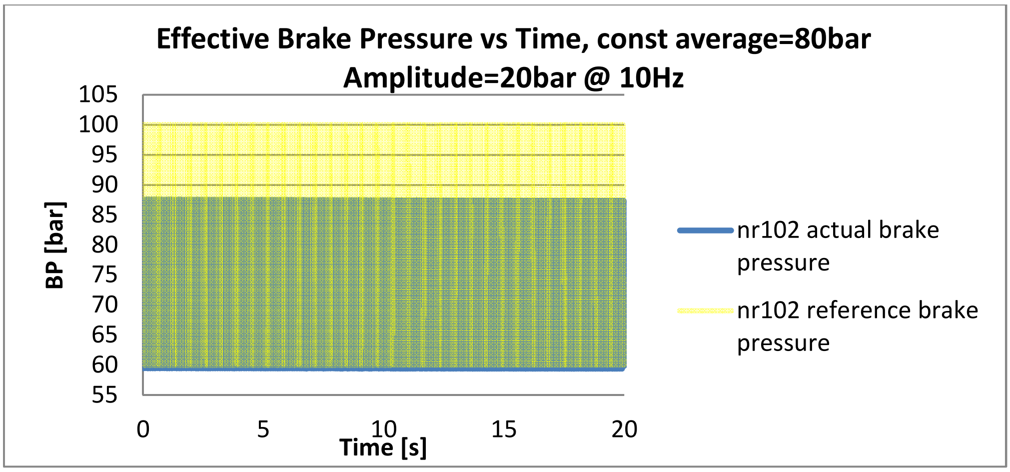


Figure 4.9 the deviation between the actual and reference brake pressure nr102 results

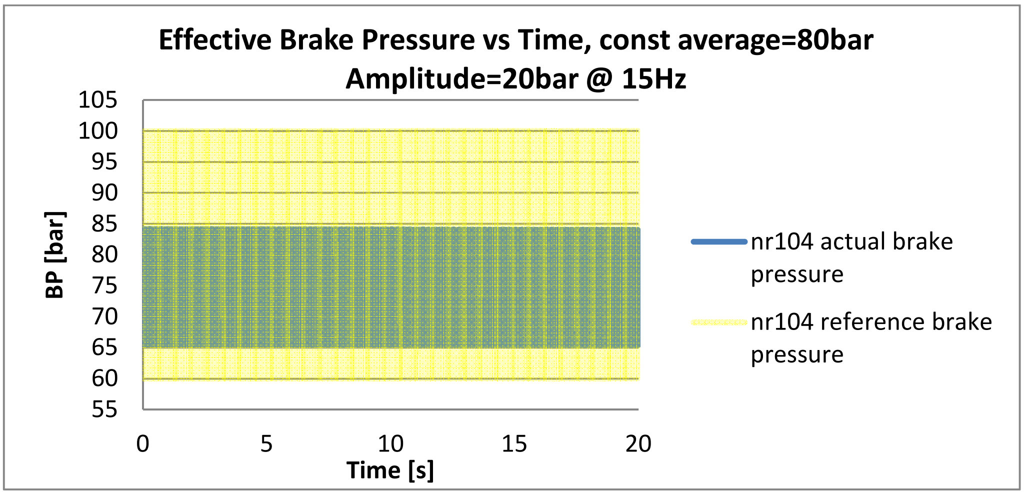


Figure 4.10 the deviation between the actual and reference brake pressure nr104 results

These static brake pressure measurement results show a significant brake pressure dynamics regression by increasing the frequency of the measurement setup. There is almost a linear relationship between the frequency change and pressure dynamics. This indicates a large damping or restriction of the measurement setup, especially in the relatively large and flexible rubber brake hose, as well as a flow rate limit within the actuating brake valve.

***Design improvements: Stainless steel braided brake hose situation:***

It is a hypothesis to improve this limited bandwidth property by replacing the original brakes hose with a stainless steel braided brake hose. The advantage of increased hose material stiffness and the decreased diameter should result into an increase of the fluid pressure build-up within the same amount of time. An improvement in time response of the brake actuation is expected.

Figures 4.15 and 4.16 show the result of the brake pressure dynamics with the stainless braided hose. The results of measurement nr 60 show a well iterated progress of the deviations compared to the results with the original situation. Probably are amplitudes of 30bar still influencing the pressure dynamics negatively.

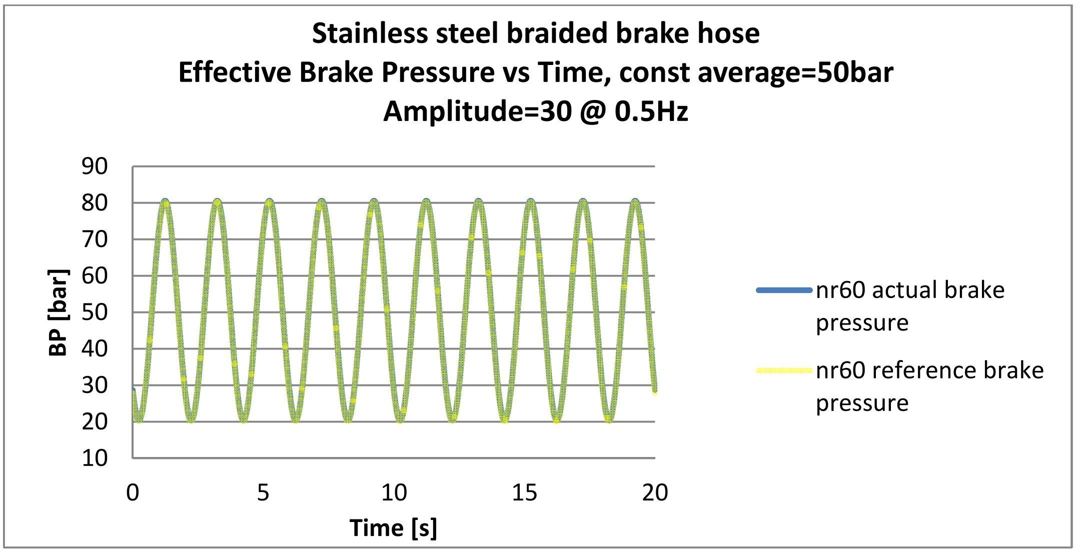

Figure 4.11 the deviation between the actual and reference brake pressure nr60 results

| [bar] | 20,19 | 50,00 | 80,26 | 50,00 | 20,19 | 50,00 | 80,26 | 50,00 | 20,19 |
|---|---|---|---|---|---|---|---|---|---|
| max | 0,24 | 0,37 | 0,28 | 0,76 | 0,23 | 0,37 | 0,28 | 0,76 | 0,24 |
| % | 1,19 | 0,74 | 0,35 | 1,52 | 1,14 | 0,74 | 0,35 | 1,52 | 1,19 |

Table 4-8 maximum deviations in [bar] and [%] between the actual and reference brake pressure nr60 of the first two waves, Constant average 50bar, A=30 bar @ 0.5Hz

Let's observe measurement nr 134, again a well iteration can be seen in table 5-0, achieved by the design improvement. The maximum achievable actual brake pressure is 97,91bar, while the reference reaches 100bar.
There is still a pressure loss of 100bar - 97,91bar =2,09bar decrease, compared to the results of nr 78 with the original situation: 99,65bar - 96,81bar =2,84bar decrease. There is 0,75bar increase reached. This low increase is an improvement, but this is not the finally solution for the VTL measurement setup.

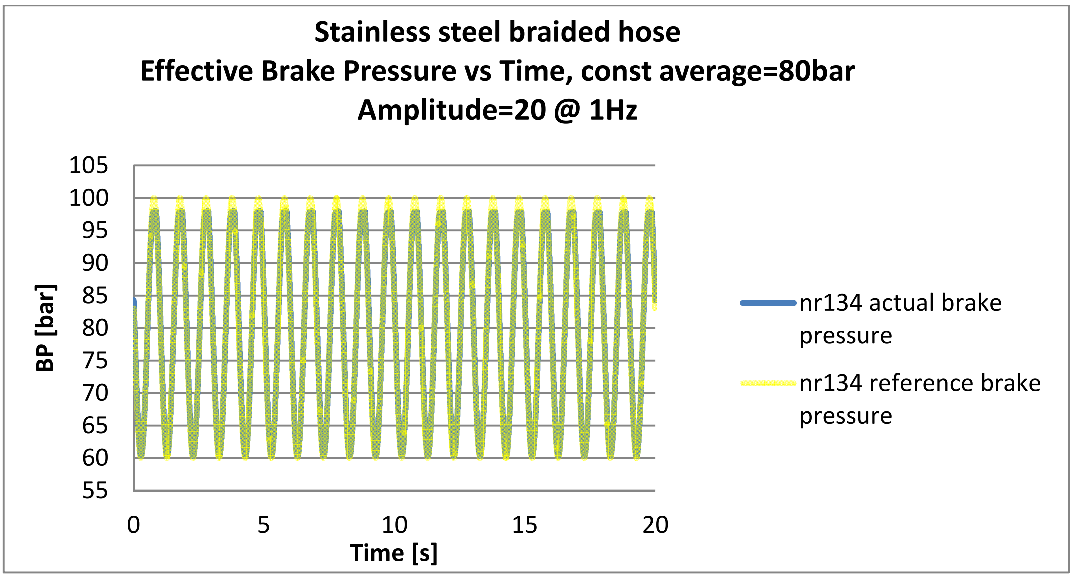


Figure 4.16 the deviation between the actual and reference brake pressure nr134 results

| [bar] | 80,00 | 60,00 | 80,00 | 100,00 | 80,00 | 60,00 | 80,00 | 100,00 | 80,00 |
|---|---|---|---|---|---|---|---|---|---|
| max | 1,23 | 0,32 | 0,80 | 2,09 | 1,23 | 0,31 | 0,80 | 2,11 | 1,22 |
| % | 1,54 | 0,53 | 1,00 | 2,09 | 1,54 | 0,52 | 1,00 | 2,11 | 1,53 |

Table 4-9 maximum deviations in [bar] and [%] between the actual and reference brake pressure nr60 of the first two waves, Constant average 80bar, A=20 bar @ 1Hz

# Chapter 5
# System Identification

Initially the static brake pressure measurements by the sinus wave excitation are done to observe the differences in pressure dynamics. It is a relatively simple and a quick measurement method to show the effects between the original and new brake hose situation. This information was too poor to identify which system parameters might have to be changed for bandwidth improvement. In order to check changes in the dynamical behaviour of the system, system identification of the whole measurement setup is needed.

## 5.1 Introduction identification Measurement Setup

Identification of the measurement setup has been done by exciting the brake pressure by random noise; this is a random non-deterministic signal. A random signal contains several signal values within a certain range, see figure 5.1. The range is described by means of statistical distributions that give the probability that the value is within the range. Also the *frequency spectrum*, which is the distribution of these frequencies can only described in statistical terms. Noise can be indicated by a colour term to indicate their frequency spectrum. Like *white noise*, this has an equal presence of all frequencies over the entire frequency spectrum [28].

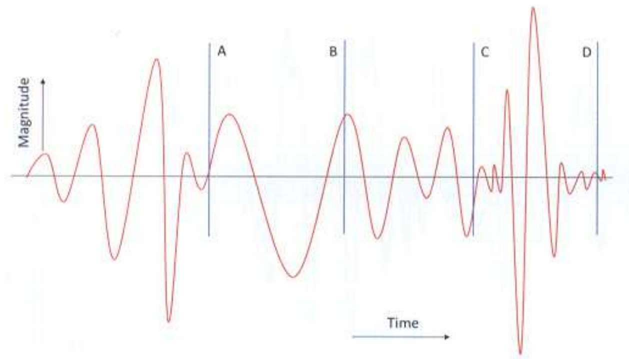


Figure 5.1 example of a random waveform in the time domain with low frequency area A-B and high frequency C-D [28]

Due to much larger frequency content, a random signal has an advantage above a sinus signal to calculate the systems' transfer function, i.e. the output signal (actual brake pressure) divided by the input signal (reference brake pressure). The transfer function contains information about the resonance frequency and bandwidth of the system, in this context it is about the measurement setup. Matlab is used to estimate its transfer function (*tfestimate*) and coherence (*mscohere*). The length of the measurement is doubled from 20 seconds to 40 seconds ($t_m$) to improve the calculations with more data, with a sampling rate ($f_s$) of 1024 Hz. The choice of this frequency will be explained on page 47 in section coherence.

**FFT**
Fast Fourier Transform (FFT) is applied on the measured data by the *tfestimate* Matlab function. The basic idea of a Fourier transform is that a periodic signal can be

decomposed into harmonically related frequencies and inverse. Only under the condition that the function contains no discontinuities as these would lead to a non-converging series. This mathematical method transforms a function from the time domain into the frequency domain, see figure 5.2.

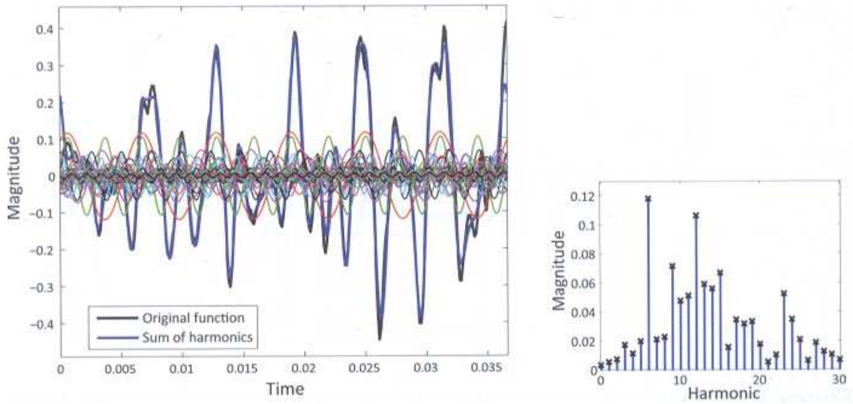


Figure 5.2 example of a random waveform approximated by the sum of several harmonic terms corresponding Fourier series. On the right the discrete version is displayed [28]

When a sample of a signal is taken over the defined time span, this sample is multiplied with a series of sine and cosine frequencies to cover the spectrum of interest. The outcome of each multiplication results in the amplitude of each of these frequencies and represented graphically in the form of a frequency spectrum. This is achieved by the algorithm Fast Fourier Transform (FFT) and with this, the frequency responses (which are the responses of the dynamic system) can be shown in Bode plots, see figure 5.3.

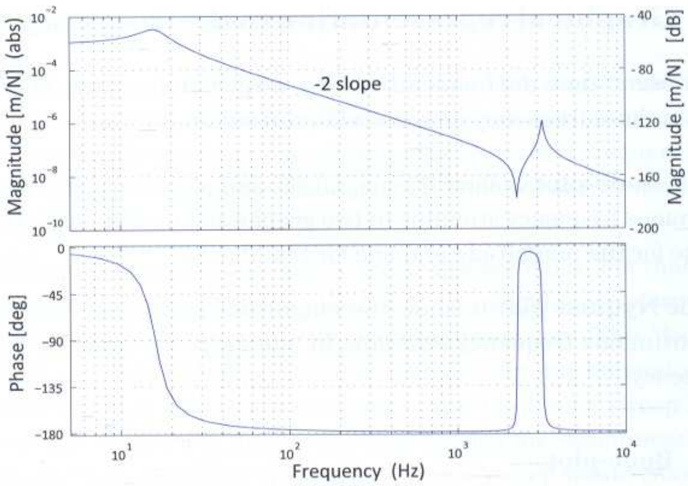


Figure 5.3 example of a Bode-plot of a motion system, the upper graph shows the magnitude of the position response by the magnitude of the force stimulus. The lower graph shows the phase relation between the position response and the force stimulus [28].

The Bode plots shows the magnitude and phase response upon a continuous frequency stimulus in two graphs as a function of the frequency, one for the magnitude and one for the phase. The upper part is the magnitude plot with the ratio between the magnitude of the *response* and the magnitude of the *stimulus* on the vertical axis [28]. Figure 5.4 shows an example of a (closed-loop) Bode-plot. This example includes different damping ratios $\varsigma$ [-] and belonging quality factors $Q$ [-], when these parameters are increasing then the resonance peak of the natural frequency will decrease. See Appendix A-2 for some related Laplace basics.

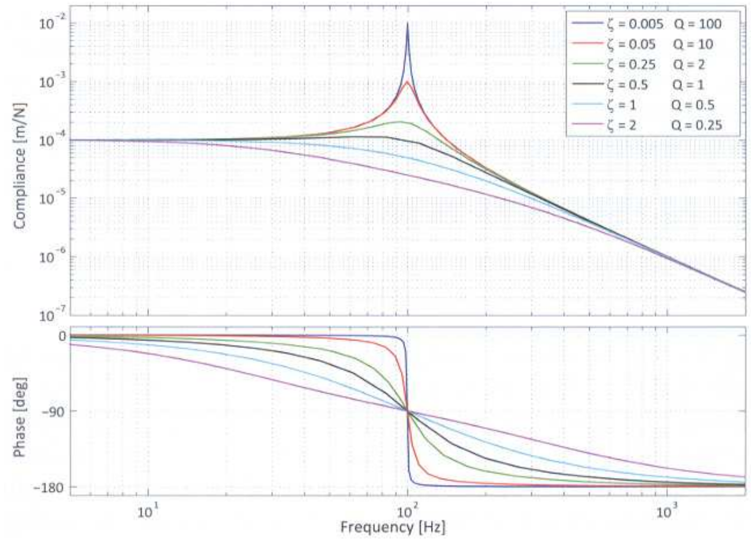


Figure 5.4 an example of a (closed-loop) Bode-plot of a damped mass-spring system, giving a natural frequency $f_0$ of 100Hz for different damping ratios $\varsigma$ and quality factors $Q$ [28]

The exact curve of the magnitude response can be thought of consisting two asymptotes. The frequency at which the two asymptotes meet is called the *corner or cut-off frequency* $\omega_0$. This frequency divides the frequency-response curve into two regions: a low-frequency $\left[\omega < \frac{1}{T}\right]$ and a high frequency $\left[\omega > \frac{1}{T}\right]$ region see figure 5.5.

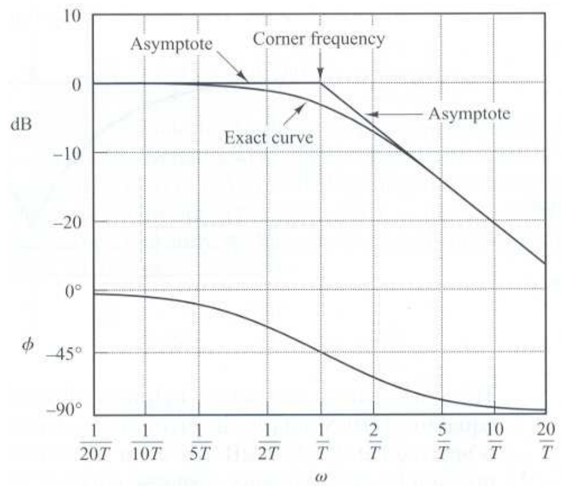


Figure 5.5 log-magnitude curve, with the asymptotes and phase-angle curve [29]

In engineering is the term *bandwidth* often used. Defined as the frequency band where the power of the output signal of a system becomes less than half the desired power level. In terms of signal amplitude the corresponding value is equal to $1/\sqrt{2} \approx 0.7$. In decibels this value is equal to -3 dB (see figure 5.6), a well-known definition for the bandwidth of filters and other frequency dependent functional devices like loudspeakers [28].

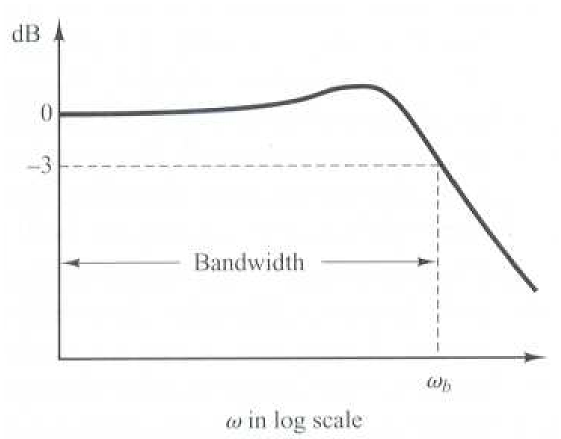

Figure 5.6 a closed-loop frequency response curve with the frequency $\omega_b$ and bandwidth [29]

**Coherence**
The coherence shows the reliability between the output and input signal waves. How well correlated the output and input signal waves are as quantified by the cross-correlation function. This is visualized by values from zero to one as a function of the frequency, see figure 5.7. Perfectly coherent is when two waves are combined they can be completely constructed interfered/super positioned at all times, this agrees to value one.

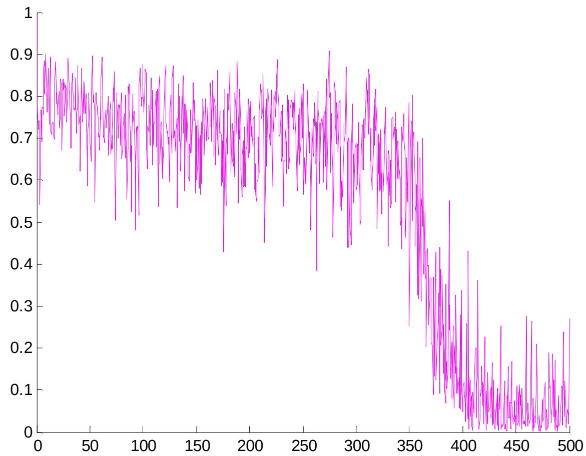

Figure 5.7 example coherence of two random noise waves

There is a relationship between the coherence time and bandwidth. If the coherence is high, the transfer function becomes reliable. A perfect coherence will not automatically lead to a desired transfer function. A low coherence results into sensitivity to disturbances uncorrelated to the input. To improve the calculation of the coherence, a larger number of transfer function blocks are preferred to average. For a given dataset this can be achieved by reducing the block size and consequently also the frequency resolution. There is a trade-off found by earlier research presented in [11]. A value nFFT=1024 is chosen and according to this work, this value is the best compromise between the coherence and the resolution. This value is also used for this research. The transfer functions begin at 0,5Hz and end at the Nyquist frequency of 500 Hz: $\omega_N = \frac{1}{2} f_s$ with $f_s = 1000 Hz$.

## 5.2 Coherence measurements

These test results are from the stainless steel braided brake hose situation and the original settings. To check the coherence increase, very low amplitudes of 0.1 to 0.9bar are used at a constant average of 50 and 80bar. These results show the influence of amplitudes on the coherence, but these very low amplitudes are not useful for practical applications. Random noise excitation is used to show the magnitude, the phase shift of the transfer functions, the bandwidth, and coherence. The best coherence results are shown below, the rest of the results can be found in appendix A-4 Signal analysis.

**Transfer function and time delay at a constant average of 50bar and an amplitude of 0.3bar, cross over frequency of 150Hz**

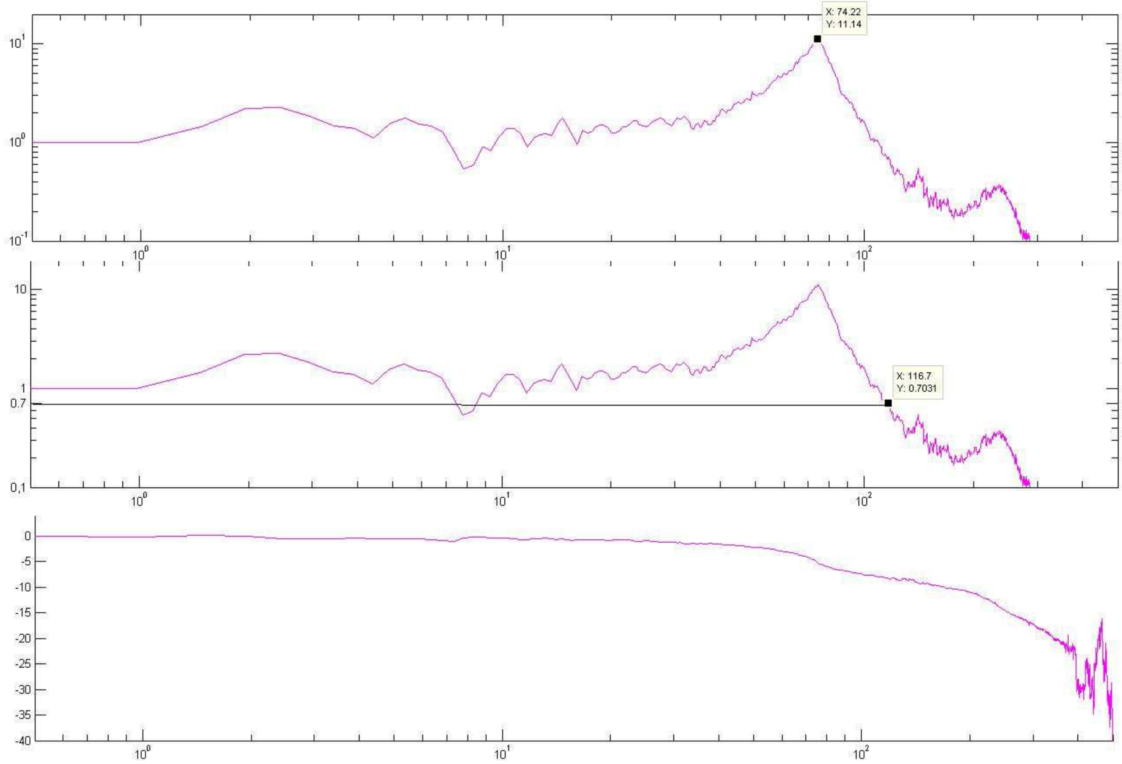


Figure 5.8 A-0.3bar_50bar, resonance frequency at 74.22 Hz, bandwidth at approx. 116Hz and a time delay till approx. 400Hz

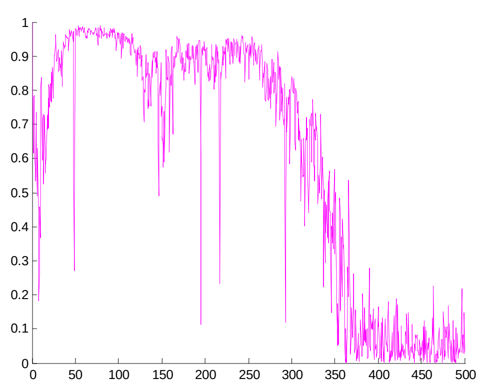

Figure 5.9 Coherence A-0.3bar_50bar

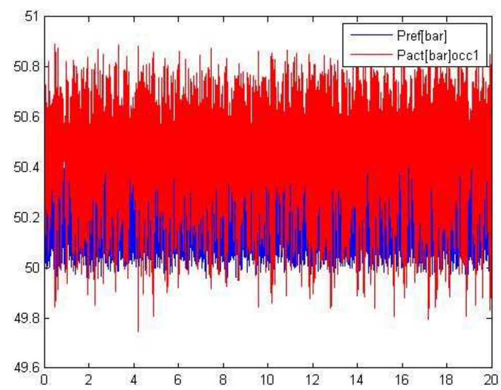


Figure 5.10 reference (std.=0.0939bar) and actual pressure [bar] during measurement

The best coherence results of the constant average of 50bar are coming from the varying amplitude of 0.3bar and 0.8bar. These results show a reasonable resonance frequency of approx.75Hz and a relative high bandwidth of approx.115Hz. The time delay keeps steady till approx. 200Hz and allows relative high pressure dynamics. The standard deviation of the varying amplitude 0.3bar is 0.0939bar and for the 0.8 bar 0.2498bar. In most cases the resonance frequency is around 75Hz.

**Transfer function and time delay at a constant average of 50bar and an amplitude of 0.8bar, cross over frequency of 150Hz**

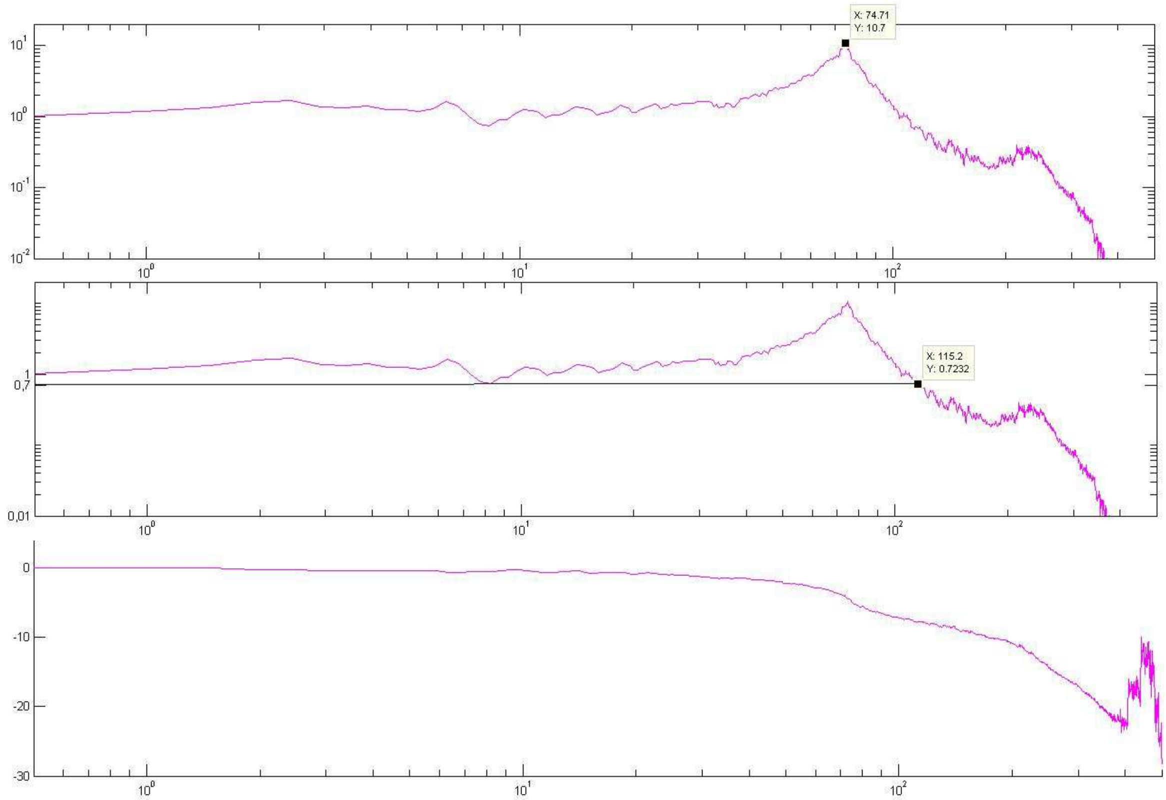


Figure 5.11 A-0.8bar_50bar, resonance frequency at 74.71 Hz, bandwidth at approx. 115Hz and a time delay till approx. 400Hz

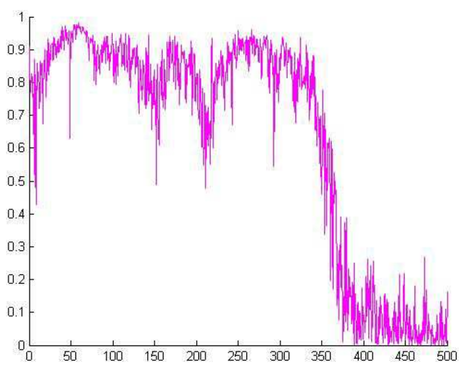

Figure 5.12 Coherence A-0.8bar_50bar

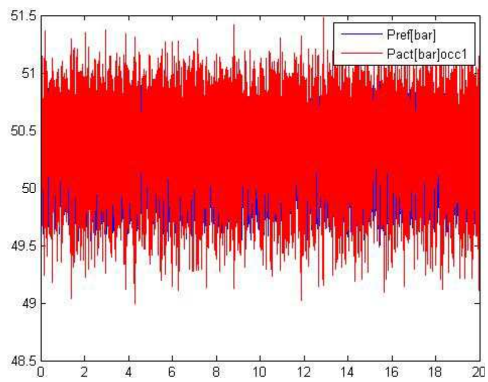


Figure 5.13 reference (std.=0.2498bar) and actual pressure [bar] during measurement

**Transfer function and time delay at a constant average of 80bar and an amplitude of 0.3bar, cross over frequency of 150Hz**

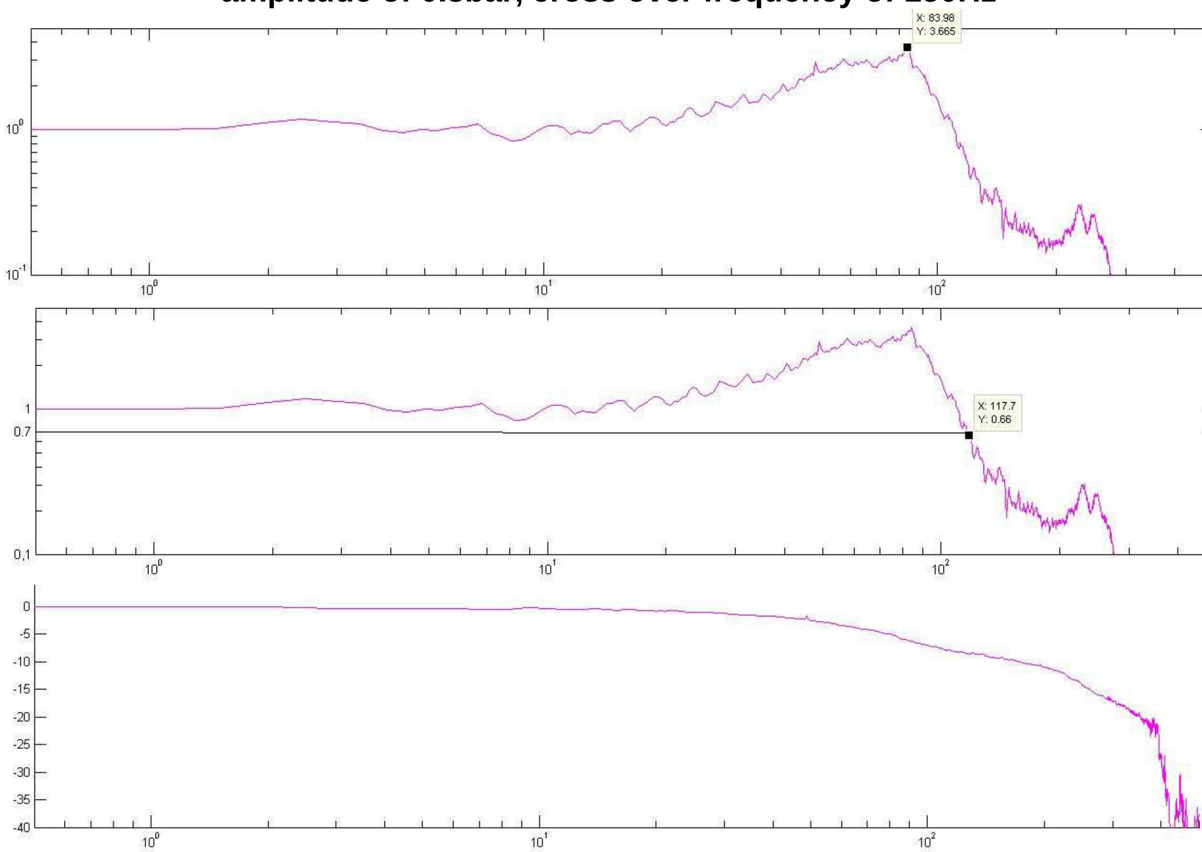


Figure 5.14 A-0.3bar_80bar, resonance frequency at 83.98 Hz, bandwidth at approx. 118Hz and a time delay till approx. 300Hz

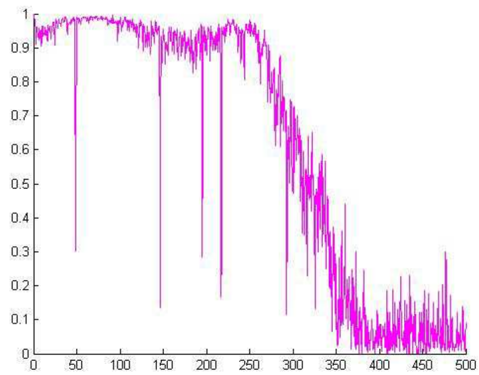

Figure 5.15 Coherence A-0.3bar_80bar

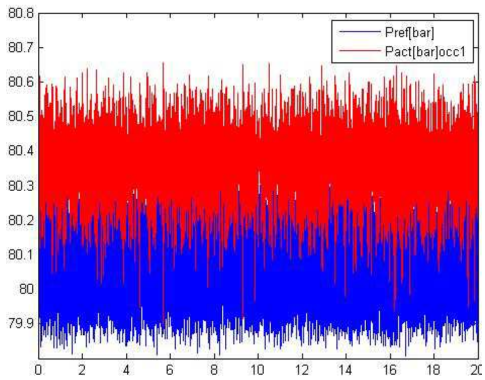


Figure 5.16 reference (std.=0.0939bar) and actual pressure [bar] during measurement

The constant average of 80bar shows the best coherence result with the varying amplitude of 0.3bar. . In most cases the resonance frequency is around 84Hz. This is increased compared to constant average of 50bar results. There is a comparable relative high bandwidth of approx.118Hz. The time delay keeps steady till approx. 250Hz and is increased compared to the constant average 50bar results, which also allows relative high pressure dynamics. The standard deviation of the varying amplitude 0.3bar is 0.0939bar.

## 5.3 Measurements with design improvements

These test results are from the measurement setup with the stainless steel braided brake hose with the original as well as new settings. Random excitation is used to show the magnitude and phase shift of the transfer functions and the coherence with amplitudes of 20bar at a constant average of 50 and 80bar. These amplitude measurements are done to see the effects on the resonance frequency and the bandwidth.

**Transfer function and time delay at a constant average of 50bar and an amplitude of 20bar, cross over frequency of 150Hz**

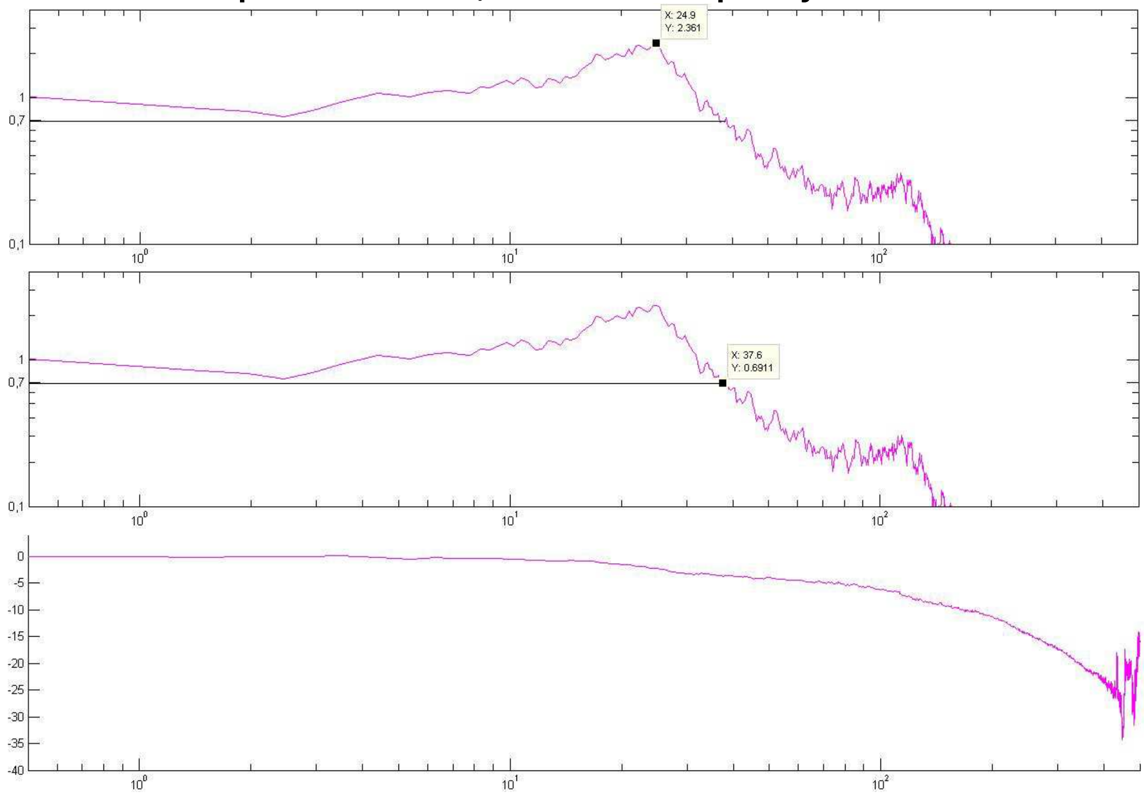


Figure 5.17 A-20bar_50bar, resonance frequency at 24.9 Hz, bandwidth at approx. 40Hz and a time delay till approx. 350Hz

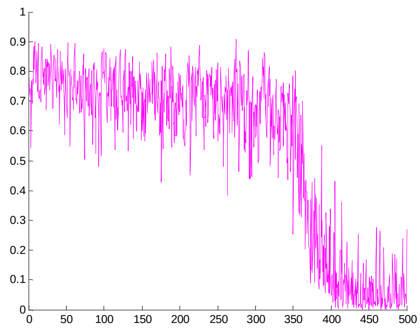

Figure 5.18 Coherence A-20bar_50bar

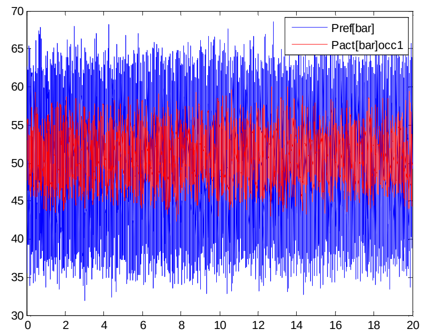


Figure 5.19 reference (std.=6.2561bar) and actual pressure [bar] during measurement

The curve of the transfer function shows a resonance peak with a relative low amplitude which could be indicated by the large damping or restriction within the measurement setup. This is physically visualized in figure 5.19 where the actual brake pressure (red) is decreased compared to the reference brake pressure (blue). The varying amplitude of 20bar has a standard deviation of 6.2561bar. This indicates the varying amplitude much better than the presumed 20bar setting. The decrease at approx.10Hz of the time delay showed in the phase shift plot indicates a decrease in pressure dynamics at low frequencies. The coherence shows to approximately 350Hz well, see figure 5.18. After this frequency the time delay displays disturbances.

**Transfer function and time delay at a constant average of 80bar and an amplitude of 20bar, cross over frequency of 150Hz**

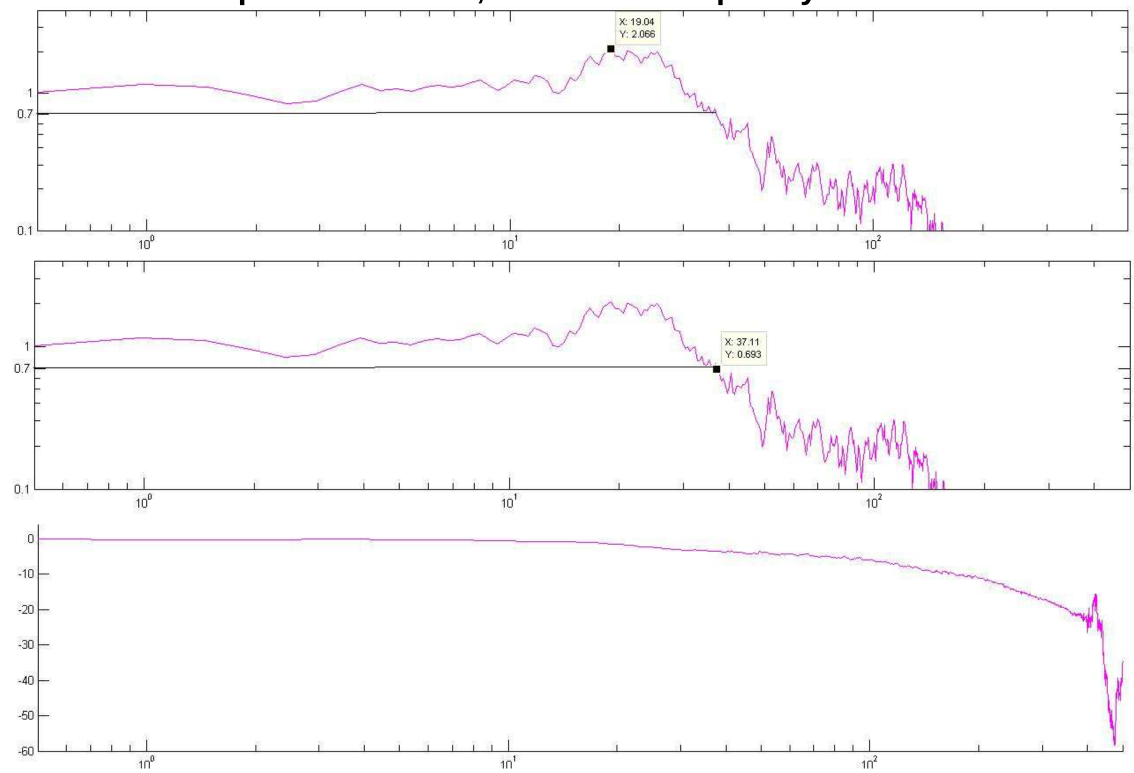


Figure 5.20 A-20bar_80bar, resonance frequency at 19.04 Hz, bandwidth at approx. 40Hz and a time delay till approx. 400Hz

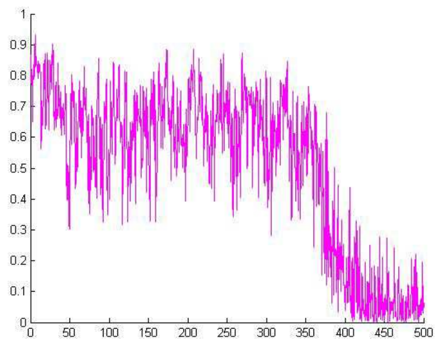

Figure 5.21 Coherence A-20bar_80bar

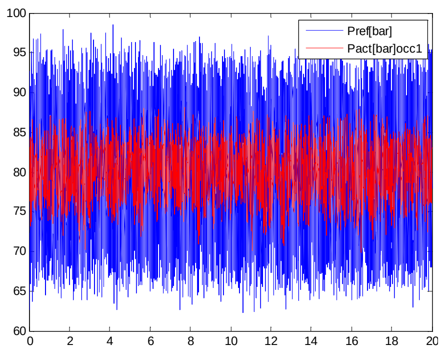


Figure 5.22 reference (std.=6.2560bar) and actual pressure [bar] during measurement

The resonance frequency is decreased by approx. 6Hz compared with the previous measurement at a constant average of 50bar. There is no obvious resonance peak, but multiple peaks. The decrease in pressure dynamics with the original settings indicates an increase in counteracting of the damping or restriction in the brake line. Reaching the presumed maximum of 100bar is not possible, see figure 5.22. This is confirmed by the standard deviation of 6.2560bar. The coherence shows higher peaks but shows well to 350Hz, see figure 5.21. The bandwidth is the same, there is no improvement by increasing the brake pressure from 50bar to 80bar with the same varying amplitude. The results of the research described in [11] found a bandwidth of around 20Hz. This result was based on an average brake pressure of 10bar with a small variance of 0.5bar.The measurements including the stainless steel braided brake hose situation show a bandwidth of approximately 40Hz, an increase of 20Hz is achieved with the original settings. The next results have a cross over frequency from 150Hz to 300Hz to see the effects on the bandwidth.

The rest of the results are obtained by a failure in the FeedForwardBrakingJP dSPACE model, the reference pressure is not visible and is affecting the magnitude of the transfer functions. The filtered analog output signal in dimensionless dSPACE [1-0] as well as in [bar] was not displayed on the ControlDesk panel. After searching the problem, it seems to be in the FeedForwardBrakingJP dSPACE model, which is not sending the dSPACE signal anymore. This is solved by copying the signal generator with the constant blocks at the output of the model. In Matlab the plots are scaled, because the transfer functions begin at a magnitude of 100 instead of 1.

**Transfer function and time delay at a constant average of 80bar and an amplitude of 20bar, cross over frequency of 300Hz**

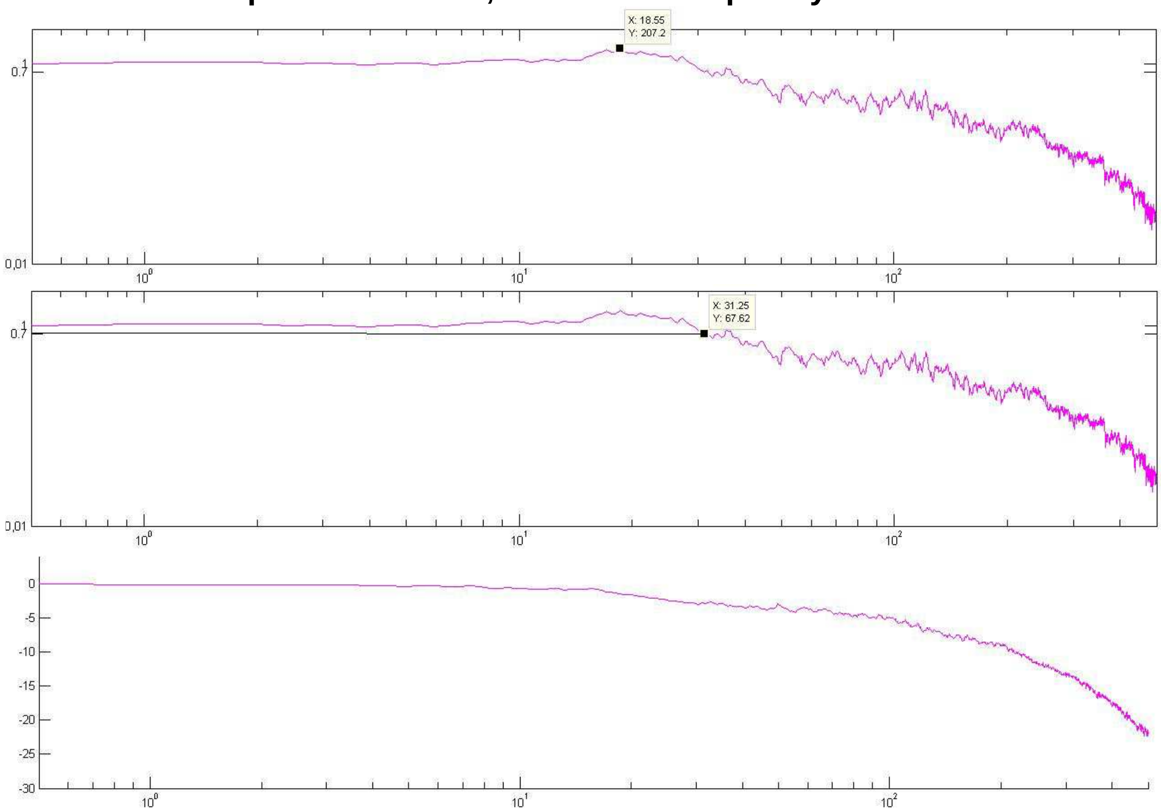


Figure 5.23 A-20bar_80bar, resonance frequency at 18.5 Hz, bandwidth at approx. 31.25Hz and a time delay till approx. 500Hz

Compared to the previous result with the cross over frequency of 150Hz, the bandwidth is decreased with approx.10Hz. The relative high amplitude of 20 bar is causing this phenomenon. Only the time delay ends at 500Hz instead of 400Hz. Increasing the cross over frequency show no bandwidth improvement.

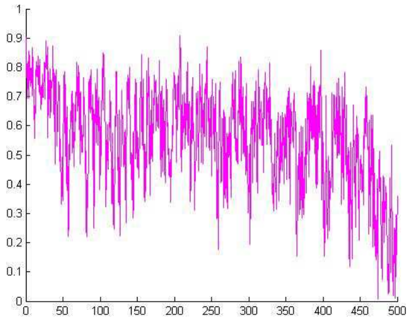

Figure 5.24 Coherence A-20bar_80bar

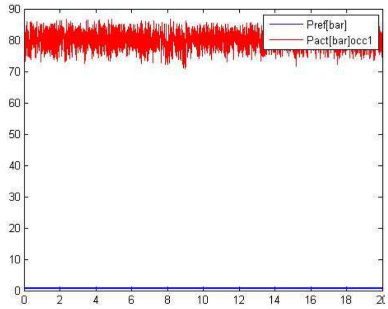


Figure 5.25 reference (std.=0.0626bar) and actual pressure [bar] during measurement

**Transfer function and time delay at a constant average of 80bar and an amplitude of 0.5bar, cross over frequency of 300Hz**

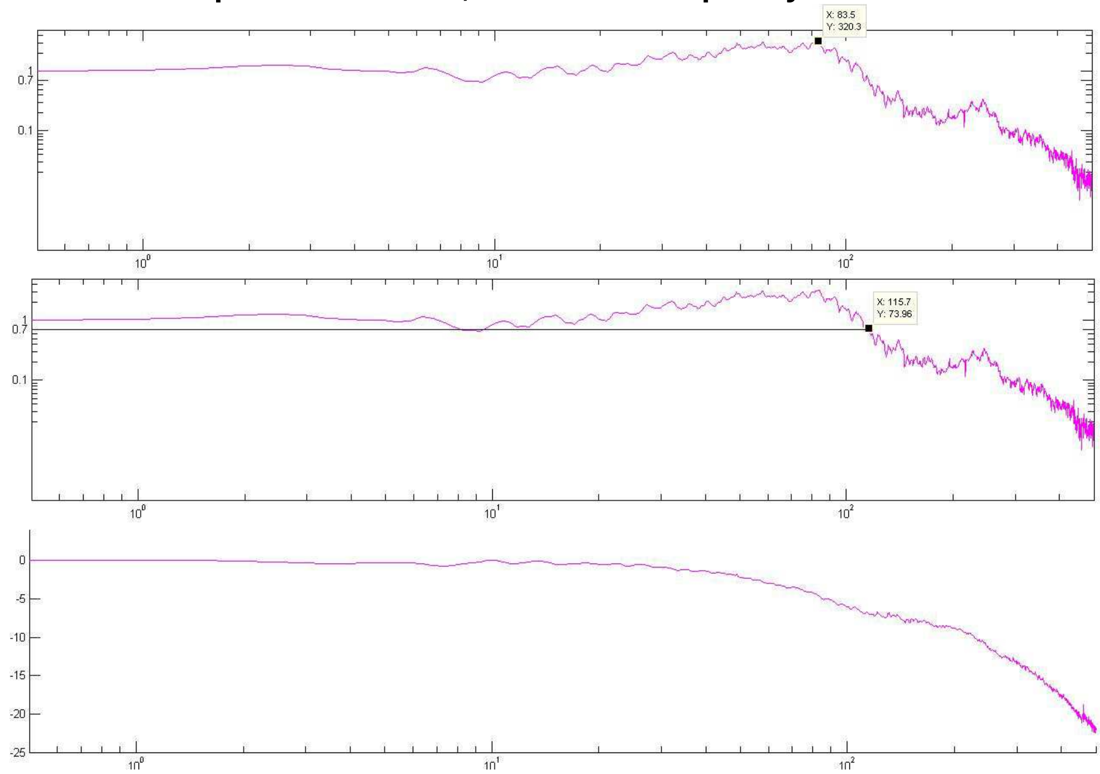


Figure 5.26 A-0.5bar_80bar, resonance frequency at 75.2 Hz, bandwidth at approx. 119Hz and a time delay till approx. 400Hz

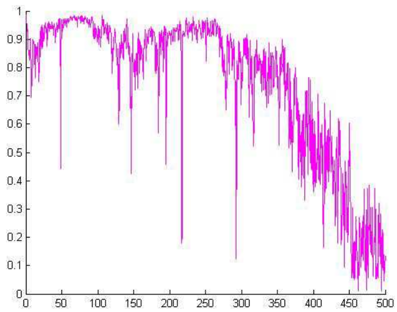

Figure 5.27 Coherence A-0.5bar_80bar

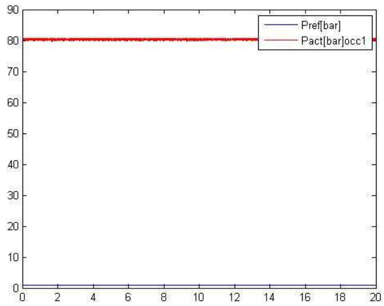


Figure 5.28 reference (std.=0.0016bar) and actual pressure [bar] during measurement

Observing the result with varying amplitude of 0.5bar, an increased resonance frequency as a relative high bandwidth is displayed in figure 5.26. The bandwidth is comparable with the bandwidth displayed in figure 5.14.

**Transfer function and time delay at a constant average of 80bar and an amplitude of 5bar, cross over frequency of 40Hz**

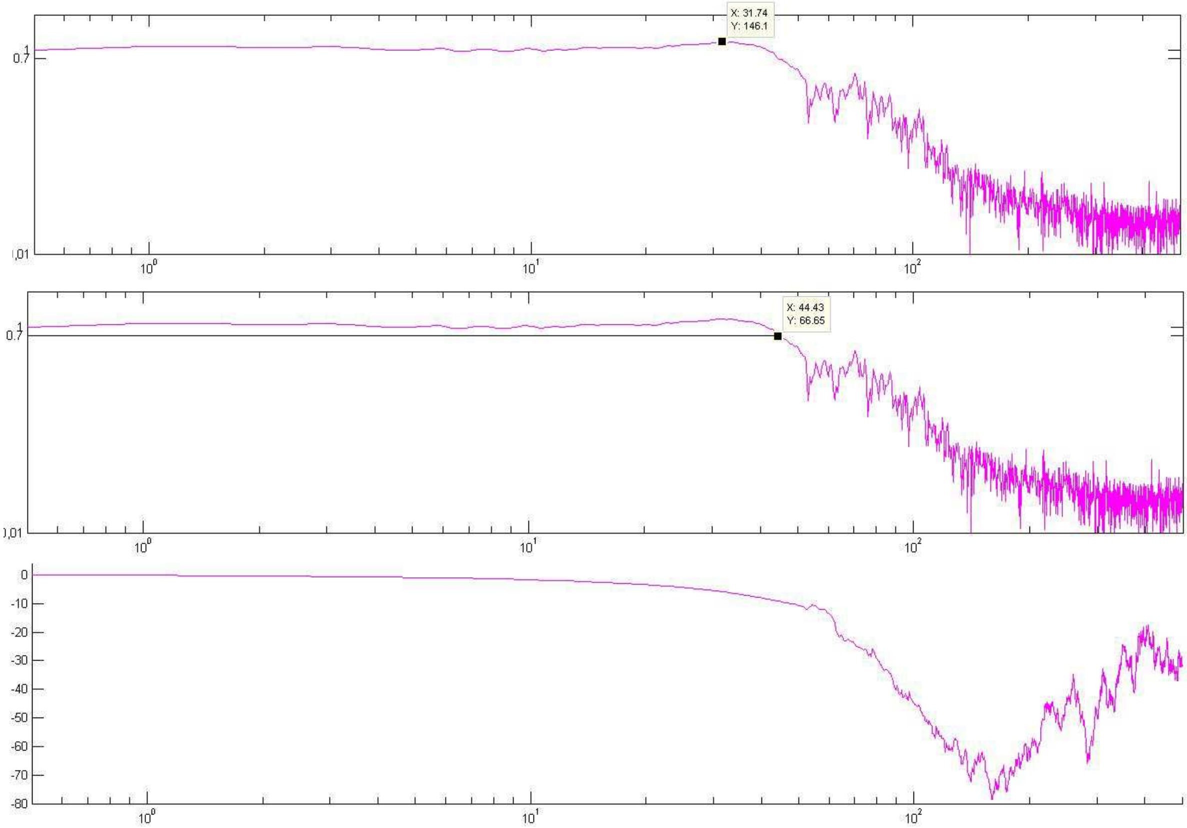


Figure 5.26 A-5bar_80bar, resonance frequency at 31.74 Hz, bandwidth at approx. 44.43Hz and a time delay till approx. 50Hz

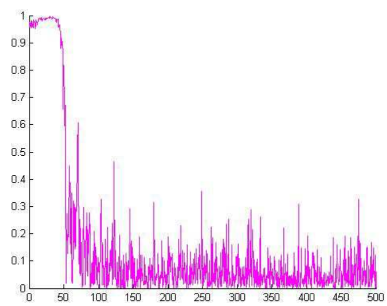

Figure 5.27 Coherence A-5bar_80bar

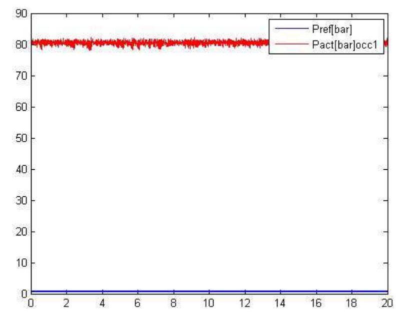


Figure 5.28 reference (std.=0.0156bar) and actual pressure [bar] during measurement

The measurement above is executed with varying amplitude of 5bar and a cross over frequency of 40Hz. The results display decreased dynamics with a resonance frequency of 31.74Hz and a bandwidth of 44.43Hz. The coherence displays well from 0 to 50Hz, for the remaining frequencies the coherence is decreased. The time delay curve shows an agreement with these frequencies.

**Transfer function and time delay at a constant average of 80bar and an amplitude of 1bar, cross over frequency of 300Hz**

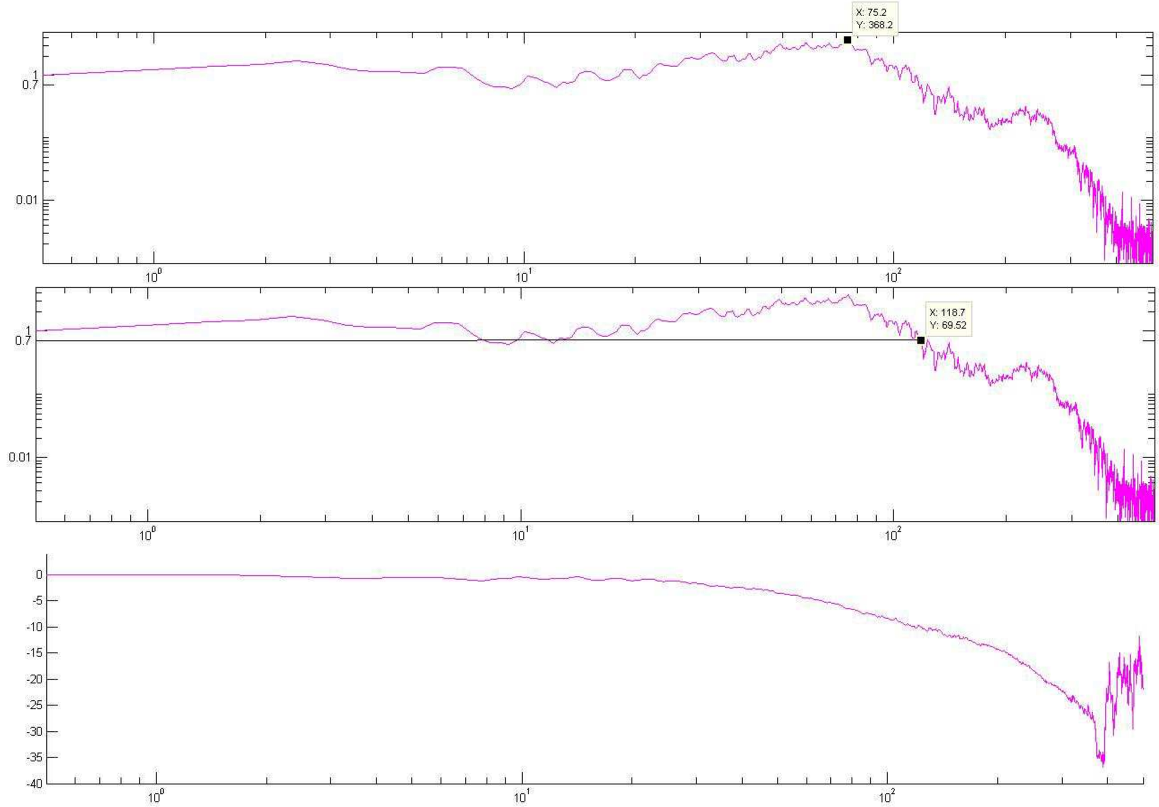

Figure 5.29 A-1bar_80bar, resonance frequency at 75.2 Hz, bandwidth at approx. 119Hz and a time delay till approx. 400Hz

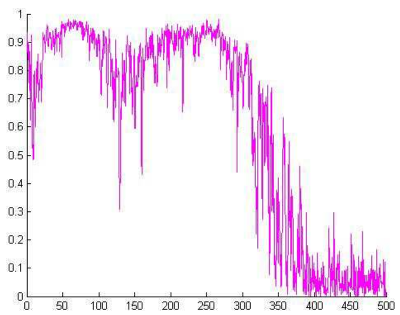
Figure 5.30 Coherence A-1bar_80bar

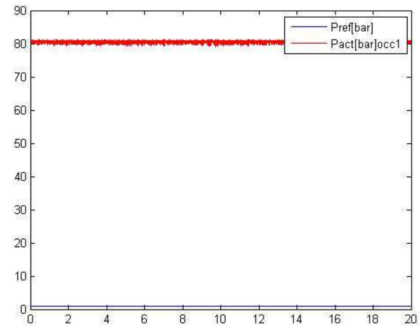

Figure 5.31 reference (std.=0.0031bar) and actual pressure [bar] during measurement

These results are comparable with results of the varying amplitude of 0.5bar. The time delay ends earlier at approx. 300Hz. The coherence shows a steeper dip at 150Hz than the coherence of the 0.5bar amplitude. This could be related to the little resonance peak at 150Hz, visible in the magnitude plot of the transfer function. The bandwidth is comparable with the bandwidth showed in figure 5.14 and 5.26.

**Transfer function and time delay at a constant average of 80bar and an amplitude of 1bar, cross over frequency of 300Hz, filtered input channel 6**

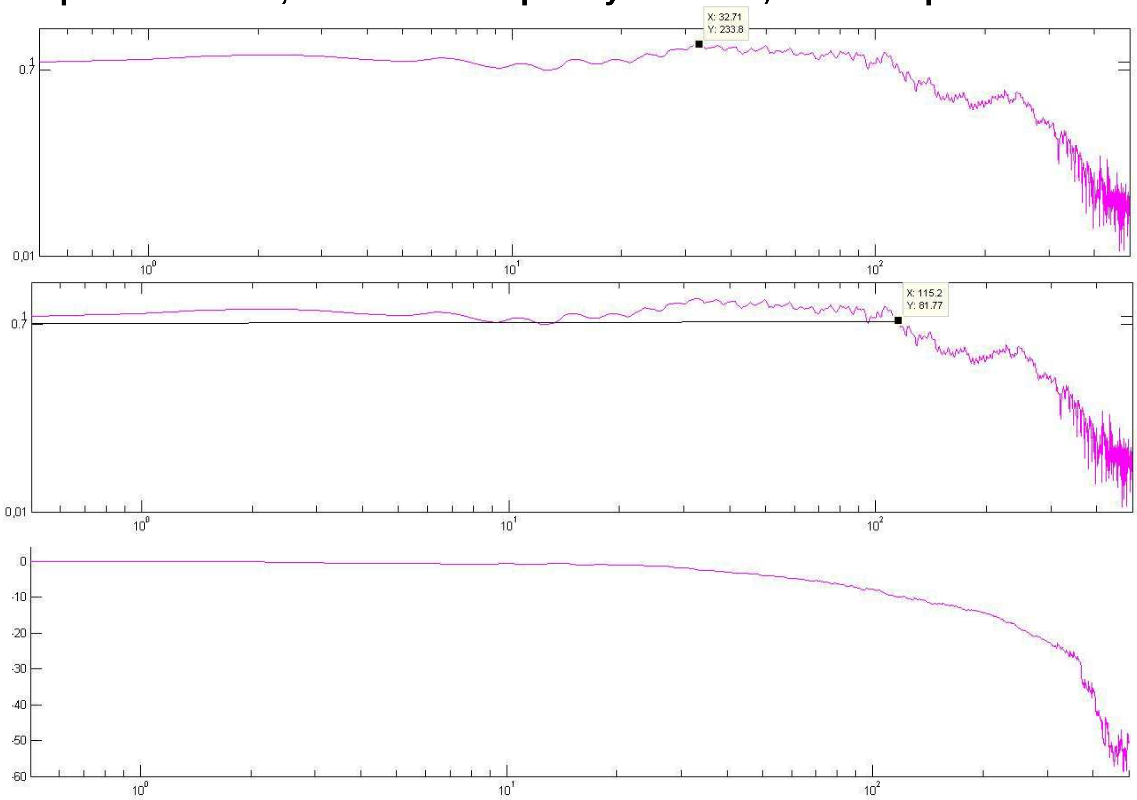


Figure 5.32 A-1bar_80bar, resonance frequency at 32.71 Hz, bandwidth at approx. 115Hz and a time delay till approx. 350Hz

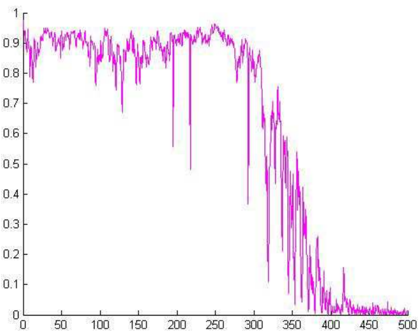

Figure 5.33 Coherence A-1bar_80bar

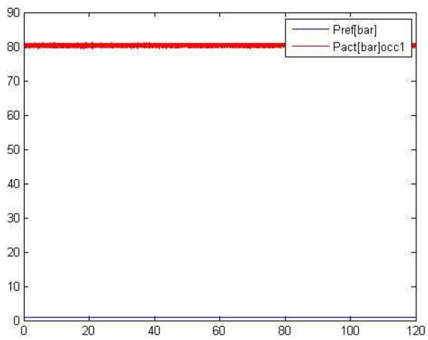


Figure 5.34 reference (std.=0.0031bar) and actual pressure [bar] during measurement

In order to check the effects in filtering of signals from the dSPACE data equipment towards the controller equipment, channel 6 of the amplifier is added in the input of the model. Channel 6 is equipped with a filter to send an input signal with limited frequency content instead of white noise of channel 5. This is done to compare the filtered input signals in a fair way. The reference input wire is connected between the analog controller and the filtered reference channel 6.
From above a decreased resonance frequency with a flattened curve can be seen. The bandwidth is almost the same as the previous result; there is a similarity with the channel containing white noise. The coherence is increased and the curve is flat to approx.350Hz.
So the original input channel 5 using white noise provides a correct input signal which is not positively biased by filters.

**Transfer function and time delay at a constant average of 80bar and an amplitude of 1bar, cross over frequency of 300Hz, upper gain knob: 2.00**

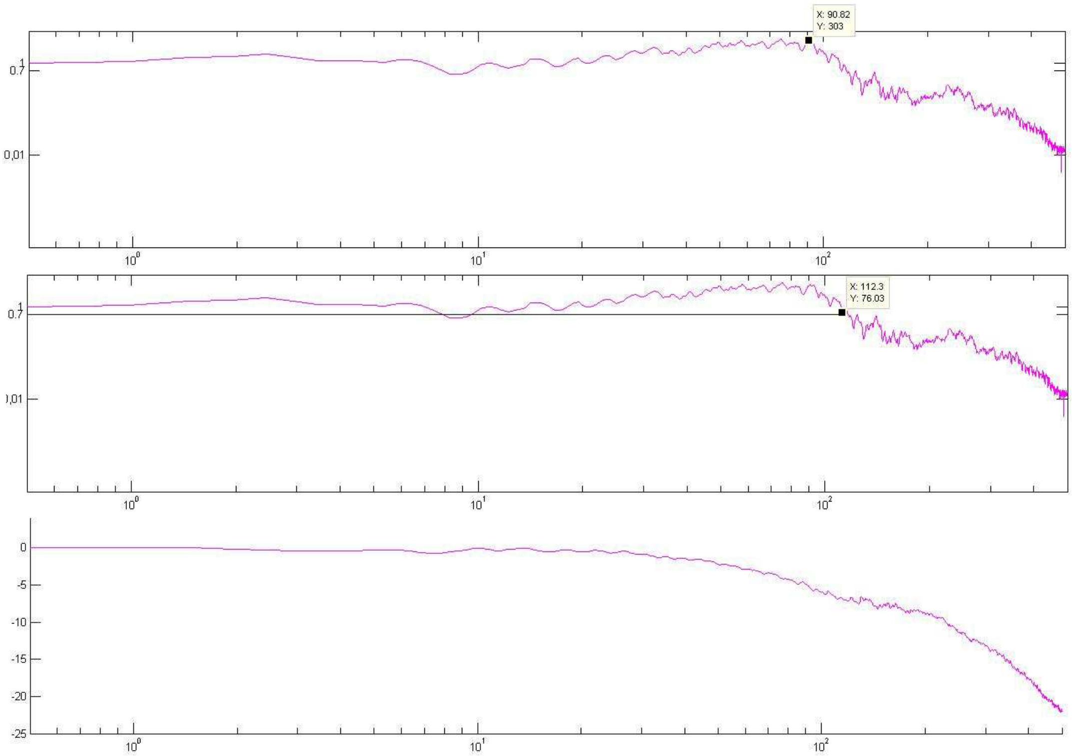

Figure 5.35 A-1bar_80bar, resonance frequency at 90.82 Hz, bandwidth at approx. 112 Hz and a time delay till approx. 500Hz

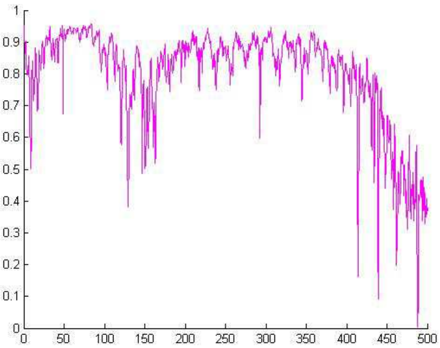
Figure 5.36 Coherence A-1bar_80bar

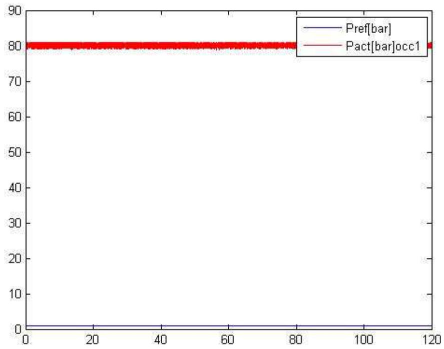

Figure 5.37 reference (std.=0.0031bar) and actual pressure [bar] during measurement

In the following measurement results the proportional gains of the analog controller are changed to see the effects. The analog controller contains two vertically placed proportional gain knobs. The upper knob is connected to measured error, where the actual and reference signal are compared and adjusted by the analog controller. The above result is coming from the situation where the upper gain knob setting is decreased from the standard 7.95 to 2.00. The results display an increased resonance frequency of 90.82Hz and an improved time delay to 500Hz. The bandwidth remains approx. 112Hz. The coherence has a dip around 150Hz and remains flat to approx. 400Hz.

**Transfer function and time delay at a constant average of 80bar and an amplitude of 1bar, cross over frequency of 300Hz, upper gain knob: 5.00**

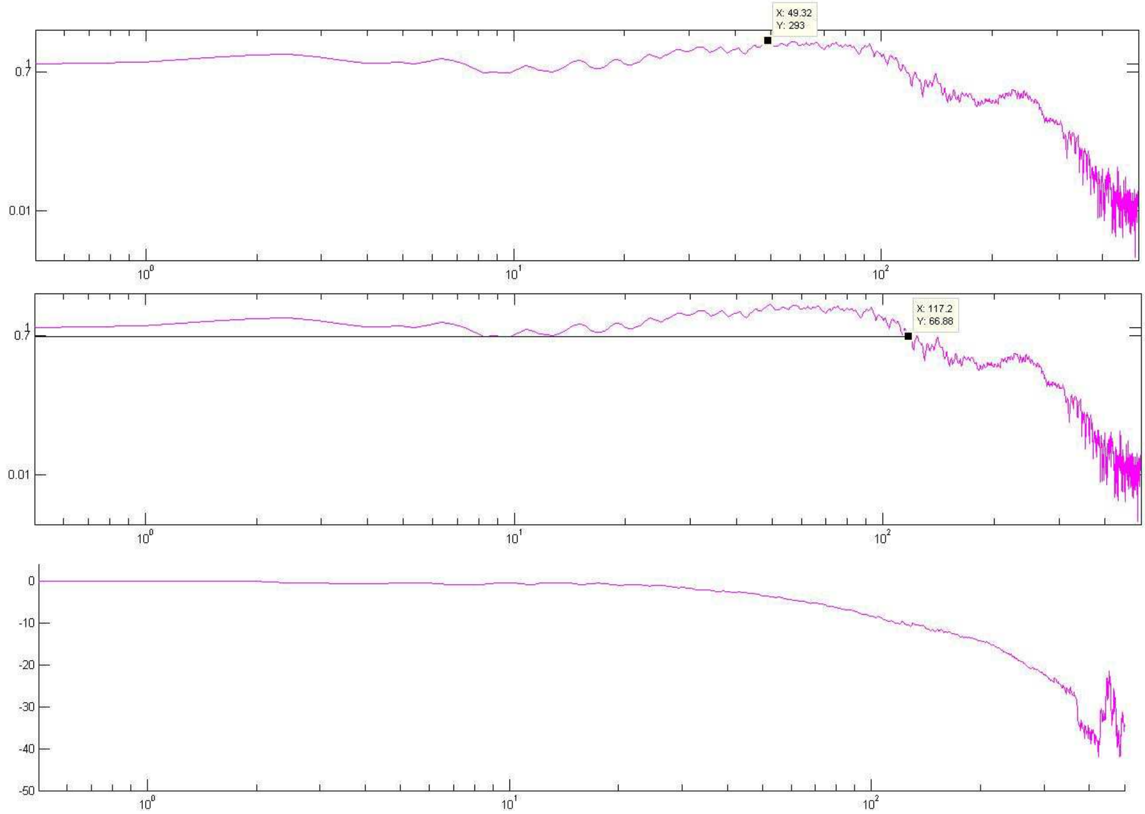


Figure 5.38 A-1bar_80bar, resonance frequency at 49.32 Hz, bandwidth at approx. 117Hz and a time delay till approx. 300Hz

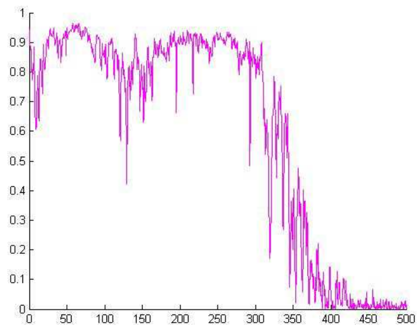

Figure 5.39 Coherence A-1bar_80bar

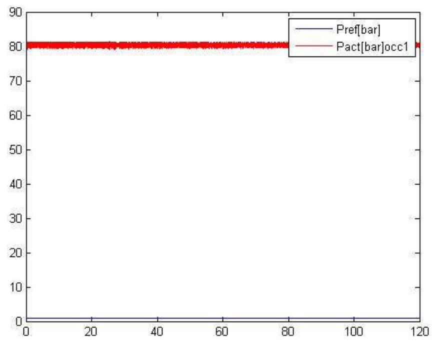


Figure 5.40 reference (std.=0.0031bar) and actual pressure [bar] during measurement

The upper gain knob is turned to 5.00, a decrease in the resonance frequency and coherence can be seen in figure 5.38 and 5.39 when comparing with the previous result with the gain setting 2.00. Also a little increase of the bandwidth and a little decrease of the time delay are observed.

**Transfer function and time delay at a constant average of 80bar and an amplitude of 1bar, cross over frequency of 300Hz, upper gain knob: 9.90**

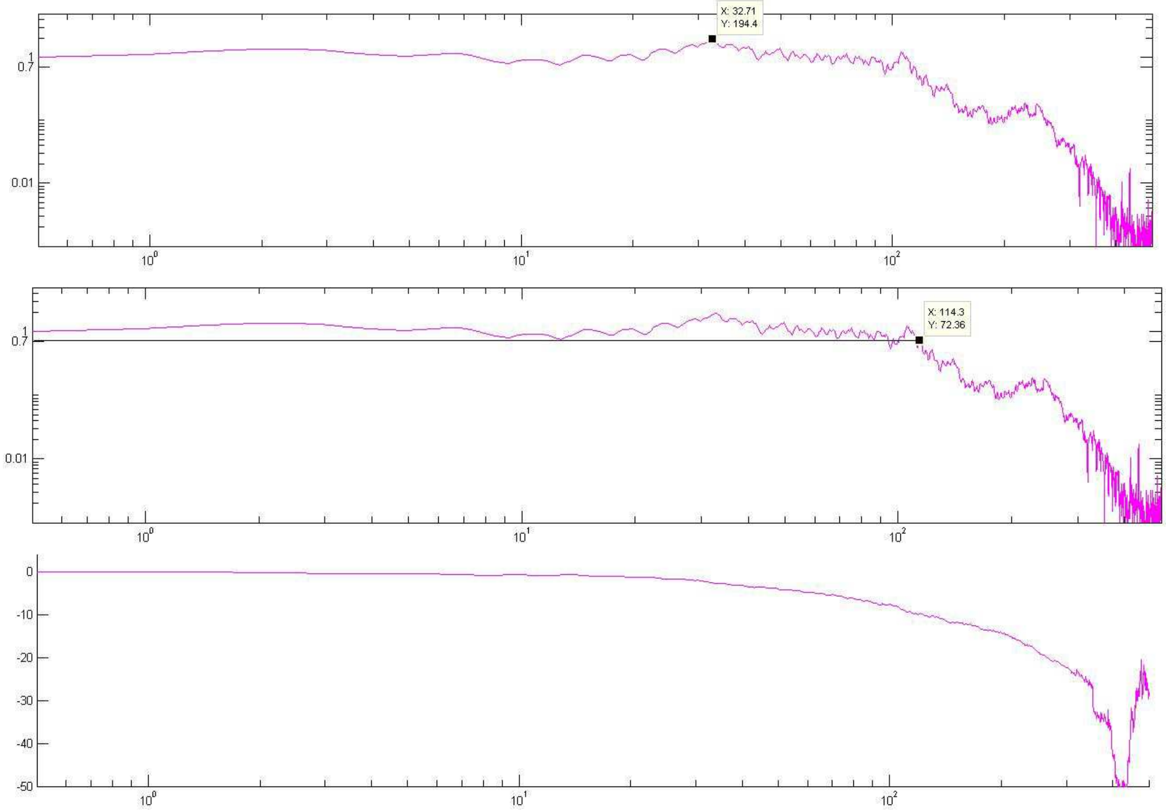


Figure 5.41 A-1bar_80bar, resonance frequency at 32.71 Hz, bandwidth at approx. 114Hz and a time delay till approx. 300Hz

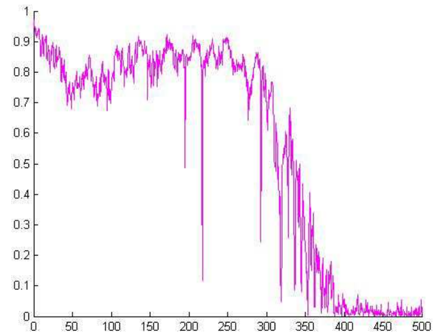

Figure 5.42 Coherence A-1bar_80bar

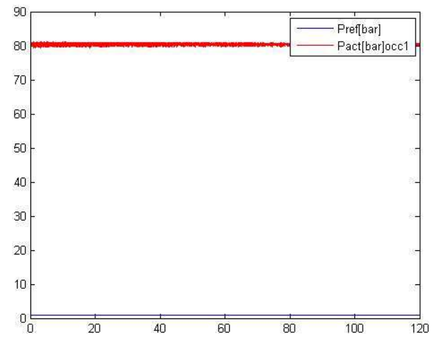


Figure 5.43 reference (std.=0.0031bar) and actual pressure [bar] during measurement

The gain is set on 9.90; the resonance frequency and time delay are decreased, the bandwidth remains roughly the same. The coherence stays flat till approx. 300Hz. No improvements are noticed with this upper gain knob setting.

**Transfer function and time delay at a constant average of 80bar and an amplitude of 1bar, cross over frequency of 300Hz, lower gain knob: 2.00**

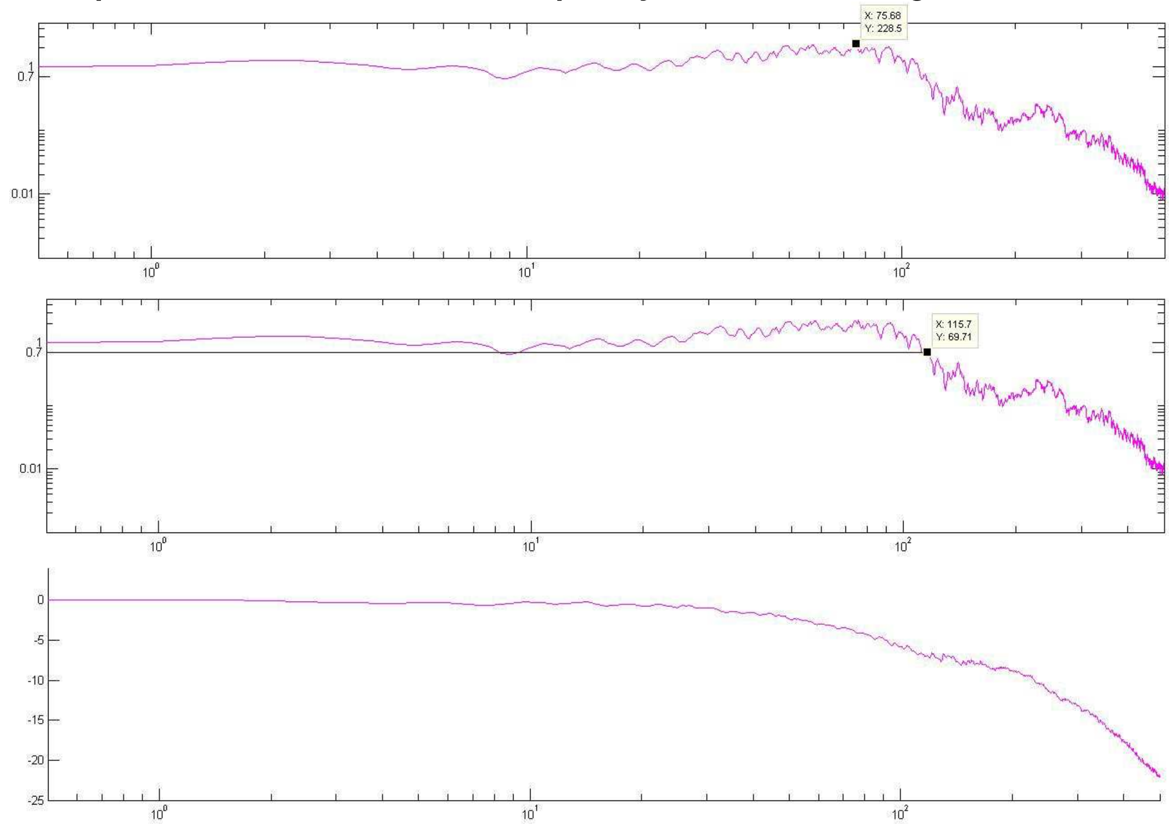


Figure 5.44 A-1bar_80bar, resonance frequency at 75.68 Hz, bandwidth at approx. 115Hz and a time delay till approx. 500Hz

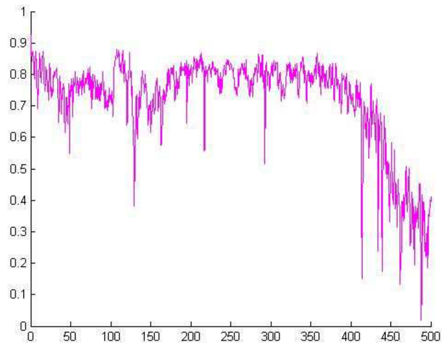

Figure 5.45 Coherence A-1bar_80bar

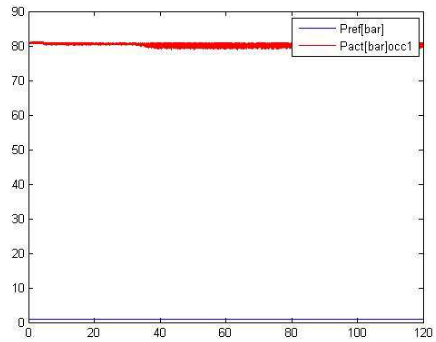


Figure 5.46 reference (std.=0.0031bar) and actual pressure [bar] during measurement

In this case the upper gain knob is back to its original setting of 7.95 and the lower gain knob decreased from 4.50 to 2.00. This is another proportional gain setting knob of the analog controller. A resonance frequency of 75.68Hz and a bandwidth of approx. 115Hz can be seen from figure 5.44. Just like the setting of 2.00 with the upper gain knob, the time delay goes to 500Hz and the coherence remains flat till 400Hz.

# Chapter 6
# Conclusion

Based on research presented in [11], system identification of the brake measurement setup in the VTL is done to show if its bandwidth can be improved. A stainless steel braided brake hose in addition with other settings are used to measure differences in brake pressure dynamics.

Sinus wave excitation results of the original situation show clearly decreased brake pressure dynamics when increasing the frequency. Also relative small maximum pressure increase of 0,75bar for the stainless steel braided brake hose situation is observed, in case of applying relative high amplitudes with relative low frequencies. Decreasing the varying amplitude will improve the dynamical behaviour of the measurement setup.

Random noise excitation results are used to estimate the magnitude and phase shift of the transfer function, the bandwidth and coherence. Increasing the coherence by using very low amplitudes is useful for measurement results, but is not practical for the measurement setup. However these results show relative high bandwidth values of approx. 115 to 120Hz.
Comparable bandwidth values are also found by applying 0.5 and 1bar varying amplitudes. Increasing the cross over frequency from 150Hz to 300Hz shows no differences in bandwidth. Decreasing the cross over frequency from 150Hz to 40Hz shows a decreased bandwidth. By adding amplifiers' channel 6, which analog reference input signal contains limited frequency content, the original reference input channel 5 shows to deliver its white noise input signal in almost the same way. When changing the proportional gains, little difference in bandwidth is noticed. The upper knob gain setting of 5.00 shows the best bandwidth of approx. 117Hz.

The stainless steel braided brake hose in the VTL measurement setup including relative low varying amplitudes of 0.5bar and 1 bar show bandwidth increase to approx. 120Hz. A bandwidth of about 20Hz was found by Van Ditten reported in [11] and a frequency range of 0-80Hz observed by Zegelaar which can be found in [4].

It is recommended to investigate the design of the remaining measurement setup components, especially the actuating brake pressure valve. Applying increased varying amplitudes will probably be inhibited due to possible flow rate limit of this valve.

# References

[1] Canudas-de-Wit C., Tsiotras P., Velenis E., Basset M., Gissinger G.: Vehicle System Dynamics, International Journal of Vehicle Mechanics and Mobility, 2003

[2] http://autorepair.about.com/library/a/1h/bl623h.htm

[3] Harned J., Johnston L. and Scharpf G.: Measurement of tire Brake Force Characteristics as Related to Wheel Slip (Antilock) Control System Design, SAE Paper 690214, 1969, pp. 909-925.

[4] Zegelaar P.W.A.: The Dynamic Response of Tyres to Brake Torque Variations and Road Unevennesses, 1998.

[5] Canudas de Wit C., Tsiotras P.: Dynamic tire Friction Models for vehicle Traction Control, Laboratoire d'Automatique de Grenoble St. martin d'Heres, France, School of Aerospace Engineering Deorgia institute of Technology Atlanta, USA, 1999.

[6] Mavros G., Rahnejat H., King P.D.: Transient analysis of tire friction generation using a brush model with interconnected viscoelastic bristles. Wolfson School of Mechanical and Manufacturing Engineering, Loughborough University UK, October 2004.

[7] De Bruijn E.: Force Sensing in Wheel Slip Control, Master of Science Thesis, 11th February 2009.

[8] Tielking J.T., Mital N.K.: A comparative Evaluation of Five Tire Traction Models, Interim Document 6, Highway Safety Research Institute/University of Michigan, January 1974.

[9] Deur J.: A Brush-type dynamic tire friction model for non-uniform normal pressure distribution, Faculty of Mechanical Engineering and naval Architecture, University of Zagreb I. Lucica 5, HR-10000 Zagreb, Croatia, 2002.

[10] Yi J., Alvarez L., Claeys X., Horowitz R. : Emergency Braking Control with an Observer-based Dynamic Tire/Road Friction Model and Wheel Angular Velocity Measurement, Vehicle System Dynamics, 2003, Vol. 39, No. 2, pp. 81-97. Swets & Zeitlinger

[11] Van Ditten M.: Measurements on Feed-Forward Braking, 1st research assignment 7th April 2010

[12] Gustafsson F.: Slip-based Tire-Road Friction Estimation, Department of Electrical Engineering, Linköping University, S-581 83, Linköping, Sweden, 28 nov.1996

[13] Seydou R., Tarek R., Zolghadri A., Henry D.: Change detection in flat systems by constraint satisfaction techniques, 18th FAC World Congress Milano (Italy) August 28 September 2 2011

[14] Brach R.M.: Adhesion, Hysteresis and the Peak Longitudinal Tire Force, PE Brach Engineering, LLC University of Notre Dame, 3-2007

[15] De Vries E., Fehn A., Rixen D., Flatness-Based Model Inverse for Feed-Forward Braking Control, 8-2009

[16] Vermeer E., Model Based Wheel Speed Controller Design, MSc thesis, TU Delft, July 2005

[17] Fehn A., Vermeer E., European patent DE 10 2005 053 863 A1, February 2007

[18] Martin Ph., Murray R.M., Rouchon P., Flat systems, Mini-source ECC97 European Control Conference, Brussels, 1-4 July 1997.

[19] Petrella R., Tursini M., Peretti L., Zigliotto M., Speed Measurement Algorithms for Low-Resolution Incremental Encoder Equipped Drives: a Comparative Analysis, University of Udine, Faculty of Engineering, University of L'Aquila, Faculty of Engineering, University of Padova, Faculty of Engineering, Italy, 17-07-2007.

[20] Kavanagh R.C. improved Digital Tachometer With Reduced Sensitivity to Sensor Nonideality", *IEEE Transactions on Industrial Electronics*, Vol. 47, No. 4, August 2000.

[21] Petrella R., Tursini M., "An embedded System for Position and Speed Measurement Adopting Incremental Encoders", *IEEE Transactions on Industry Applications*, in press.

[22] http://rb-kwin.bosch.com/nl/nl/safety_comfort/drivingsafety/abs/brakemoresafely.html

[23] De Vries E., Fehn A., Rixen D., Flatness-Based Model Inverse for Feed-Forward Braking Control, IAVSD2009Flatness_review03032010, TU Delft, Robert Bosch GmbH, Postfach 13 55, 74003 Heilbronn Germany 6-9-2011

[24] http://www.stausaonline.com/tire-manufacturing/process.html

[25] Tanelli M., Piroddi L., Piuri M. and Savaresi S.M.: Real-time identification of tire-road friction conditions, 17th IEEE International Conference on Control Applications Part of 2008 IEEE Multi-conference on Systems and Control San Antonio, Texas, USA, September 3-5, 2008.

[26] Olsson H., Aström K.J., Canudas de Wit C., Gäfvert M., Lischinsky P.: Friction Models and Friction Compensation, Department of Automatic Control, Lund Institute of Technology, Lund University Sweden, Laboratoire d'Automatique de Grenoble, France, Control Department EIS ULA, Merida, Venezuela 28-11-1997.

[27] Canudas de Wit C., Tsiotras P., Velenis E., Basset M. and Gissinger G.: Dynamic Friction Model for Road-Tire Longitudinal Interaction Vehicle System Dynamics Draft Article October 14, 2002.

[28] Munnig Schmidt, R., Schitter G. and Van Eijk J.: The Design of High Performance Mechatronics, Delft University Press 2011.

[29] Ogata K.: Modern Control Engineering, fourth edition, University of Minnesota, 2002.

# Appendix A
Vehicle Test Lab

## A-1 Signal Specifications

| Sensor Signals VTL | | | |
|---|---|---|---|
| Signal | Sensor | Type | Comment |
| Wheel speed | Hollow shaft encoder | Hengstler RI 58 | $5000 \frac{pulses}{cycle}$ |
| Drum speed | Hollow shaft encoder | | A counting box in between the encoder and dSpace. dSpace receives a 0-10V signal. |
| Electromotor speed | | | Estimation of the electromotor rotational frequency, obtained from ABB frequency converter. |
| Brake pressure | quartz high pressure sensor | Kistler 701A | After charge amplifier $10 \frac{bar}{V}$ |
| Brake torque | infrared rotating Torque sensor | Sendev 01251 | $2712,6 \frac{Nm}{V}$ |
| Force $F_x$ (4x) | Piezo force sensor | Kistler 9251 | After summing box $1036,3 \frac{N}{V}$ and $1027,5 \frac{N}{V}$, one for each side of the steel wheel frame. |
| Force $F_y$ (4x) | Piezo force sensor | Kistler 9251 | After summing box $1013,4 \frac{N}{V}$ |
| Force $F_z$ (4x) | Piezo force sensor | Kistler 9251 | After summing box $2176,2 \frac{N}{V}$ and $2102,6 \frac{N}{V}$ |
| Temperature | IR temp sensor | | $25 \frac{°C}{V}$ |

Table A-1: VTL sensor signals

## A-2 Transfer function Caliper

The transfer function equation of the brake caliper provides a basic insight in terms of damping and amplitude. This is the brake actuator, one small component of the whole brake measurement setup. Before explaining the transfer function of the caliper, first a general Laplace transform will described. Laplace is fundamental in engineering, important to understand the results presented in this thesis and also basics of the transfer function equation of a brake caliper.

***Laplace transform***:
This transform is used to solve differential equations in the *time domain* by solutions in the *frequency domain* [28].
When $f(t)$ is a function of the time variable $t$, the Laplace transform is

$f(s) = \int_0^\infty e^{-st} f(t)dt$. Laplace variable $s$ is a complex number: $s = \sigma + j\omega$, where $j^2 = -1$, $\sigma$ and $\omega$ are real numbers.

Laplace transform of a differential of a variable $x(t)$ over time is in the following expression in the frequency domain: $L\left\{\frac{dx(t)}{dt}\right\} = sx(s) = j\omega x(s)$

The integration action gives: $L\left\{\int_0^t x(t)dt\right\} = \frac{x(s)}{s} = \frac{x(s)}{j\omega} = -j\frac{x(s)}{\omega}$

The term $s$ results due to the differentiation both in a proportional magnitude increase of the variable with increasing frequency by the multiplication with $\omega$ and a positive phase shift of 90°. Which corresponds with the positive imaginary term $j$.
For the integration of a variable over time gives both a proportional magnitude decrease with increasing frequency, by the division of $\omega$ and a phase shift of -90°. This corresponds to the $-j$ term. The phase angle is determined by the arctangent of the ratio of their imaginary and real terms, where the quadrant of the angle is given by the signs of the terms. For a positive real and imaginary value the angle equals: Phase=$\phi = \arctan\left(\frac{\text{Im}}{\text{Re}}\right)$. See figure A-2.1 for the real and imaginary axis representation.

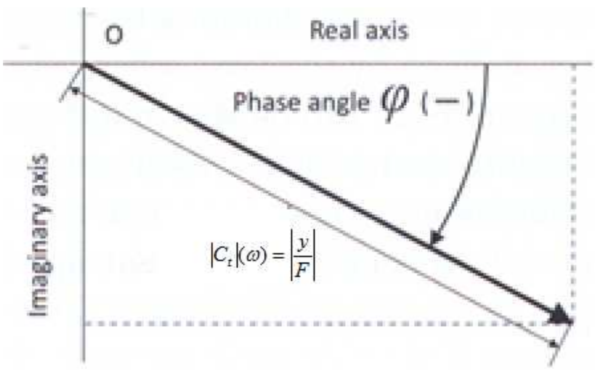


Figure A-2.1: Nyquist representation of the response of a damped mass-spring system at one frequency [28]

In order to analyse the transfer function of the caliper, the piston of the caliper with the brake pad can be simplified to a damped mass-spring system as figure A-2.2 shows.

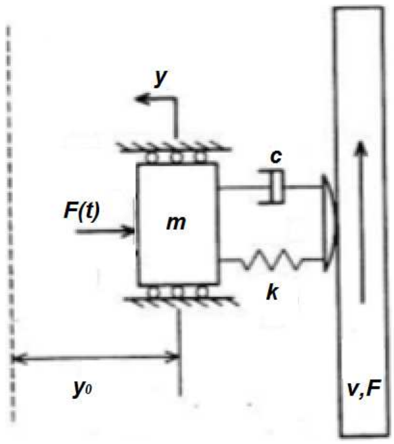


Figure A-2.2: Caliper piston and brake pad as damped mass-spring system pushing on the rotating brake disc [3]

With:

| | | |
|---|---|---|
| $y_0$: | start position mass caliper piston | $[m]$ |
| $y$: | displacement caliper piston | $[m]$ |
| $m$: | mass caliper piston | $[kg]$ |
| $k$: | spring stiffness of the brake pad | $\left[\frac{N}{m}\right]$ |
| $c$: | damping coefficient of the brake pad | $\left[\frac{Ns}{m}\right]$ |
| $F(t)$: | brake force depending on time | $[N]$ |
| $F$: | brake force on disc | $[N]$ |
| $v$: | velocity brake disc | $\left[\frac{m}{s}\right]$ $(v = \omega \cdot r)$ |

Force equation in time domain:

$$F(t) = m\frac{dy^2}{t^2} + c\frac{dy}{dt} + ky$$

Using Laplace transform, this differential equation can be written in the frequency domain:

$$F(s) = ms^2 y + csy + ky = y(ms^2 + cs + k)$$

The transfer of displacement $y$ as a result of force $F$ becomes:

$$C_t(s) = \frac{y}{F} = \frac{1}{ms^2 + cs + k}$$

$$C_t(s) = \frac{y}{F} = \frac{\frac{1}{k}}{\frac{m}{k}s^2 + \frac{cs}{k} + 1} \left[\frac{m}{N}\right]$$

The derived variables becomes:

Eigen frequency: $\omega_0 = \sqrt{\frac{k}{m}}$  Spring compliance: $C_s = \frac{1}{k}$  Damping ratio: $\zeta = \frac{c}{2\sqrt{km}}$

Using the derived variables in transfer function $C_t(s)$:

$$C_t(s) = \frac{y}{F} = \frac{C_s}{\frac{s^2}{\omega_0^{\,2}} + 2\zeta\frac{s}{\omega_0} + 1} \quad \left[\frac{m}{N}\right]$$

To determine the amplitude of the signal, the Laplace variable $s$ is substituted by $j\omega$ to give the equation as function of the radial frequency $(\omega)$:

$$C_t(\omega) = \frac{y}{F} = \frac{C_s}{\frac{j^2\omega^2}{\omega_0^{\,2}} + j2\zeta\frac{\omega}{\omega_0} + 1} = \frac{C_s}{\underbrace{1 - \frac{\omega^2}{\omega_0^{\,2}}}_{REAL\ \ PART} + \underbrace{j2\zeta\frac{\omega}{\omega_0}}_{IMAGINARY\ \ PART}} \quad \left[\frac{m}{N}\right]$$

The amplitude is of the transfer function $C_t(\omega)$ becomes:

$$|C_t|(\omega) = \left|\frac{y}{F}\right| = \frac{C_s}{\sqrt{\left(1 - \frac{\omega^2}{\omega_0^2}\right)^2 + \left(2\zeta\frac{\omega}{\omega_0}\right)^2}}$$

In case of no damping: $\zeta = 0$, the brake caliper shows an uncontrolled resonance.

$$|C_t|(\omega) = \left|\frac{y}{F}\right| = \frac{C_s}{\sqrt{\left(1 - \frac{\omega^2}{\omega_0^2}\right)^2}} \rightarrow \frac{C_s}{\sqrt{\left(\frac{\omega_0^2}{\omega_0^2} - \frac{\omega^2}{\omega_0^2}\right)^2}} \rightarrow \frac{C_s}{\sqrt{\omega_0^2 - \omega^2}}$$

$$|C_t|(\omega) = \left|\frac{y}{F}\right| = \infty \qquad \text{when } \omega_0 = \omega$$

In presence of damping, $C_t(\omega)$ at this frequency relative to the spring-line, becomes maximal when $\omega_0 = \omega$:

$$|C_t|(\omega) = \left|\frac{y}{F}\right| = \frac{C_s}{\sqrt{\left(\frac{\omega_0^2}{\omega_0^2} - \frac{\omega_0^2}{\omega_0^2}\right)^2 + \left(2\zeta\frac{\omega_0}{\omega_0}\right)^2}} \rightarrow \frac{C_s}{2\zeta}$$

$$\frac{|C_t|\max}{C_s} = \frac{1}{2\zeta}$$

Sufficient hydraulic damping of the caliper is needed, but too much hydraulic damping decrease the brake dynamics and results into a decreased bandwidth of the measurement setup. Decreasing the damping of the brake pads increases the brake frictional force.

## A-3 Brake Pressure measurements sequence

The brake pressure measurements sequence:

- Open Matlab Simulink, click on file *"init.m"* within ***D:\FeedforwardBraking\BrakePressureTest*** and load the ***Brakepressuretest_FeedForwardBrakingJP model*** (.mdl file), build this model by pressing *"Ctrl B"* on the keyboard at the highest level of the model.

- Open dSPACE ControlDesk, open experiment in ***BrakePressureTest BrakePressureJPExperiment.cdx*** (including the control panel) and load the associated ***Brakepressuretest_FeedforwardbrakingJP.sdf*** file. Click on *"animation mode"* and adjust the settings of the data acquisition (where to safe, with which name, the length of each measurement, the number of down sampling).

- Choose the settings to actuate the by-pass valve, wave form, amplitude, frequency and the constant value where the signal is varying on. Click "Brake Pressure" ON in the control panel.

- Switch the following ON:

- Load force equipment and switch the small metal knob down and up, the by-pass valve controller (proportional analog controller), plug the hydraulic pump into the 380V socket.
- Reset the charge amplifier by switching 1 second, 1 tick down and up.
- Click on "Start" of the data acquisition part, the measurement data is from now logging. The measured brake pressure is on zero bar.
- Turn the voltage supply of the by-pass valve ON and the brake pressure is building up.
- At the ends of each measurement click on "Stop" of the data acquisition part.
- Turn the voltage supply of the by-pass valve OFF.
- Reset the brake pressure receiver by switching 1 second 1 tick down and up, the brake pressure for the next measurement is reset to zero.

## A-4 dSPACE ControlDesk sequence

To actuate and measure the VTL test setup, a control panel in ControlDesk has to be made, its design is up to yourself. From the existing Feed-Forward ABS model, the specific parameters are carefully chosen. Be aware of dimensionless dSPACE parameters in 0.1 order, Volts are times 10 and the pressure are times 100 the dSPACE parameters.
After modelling the control panel, the pre-defined experiment in dSPACE can be linked to the control panel by opening the experiment as figure A-4.1 shows.

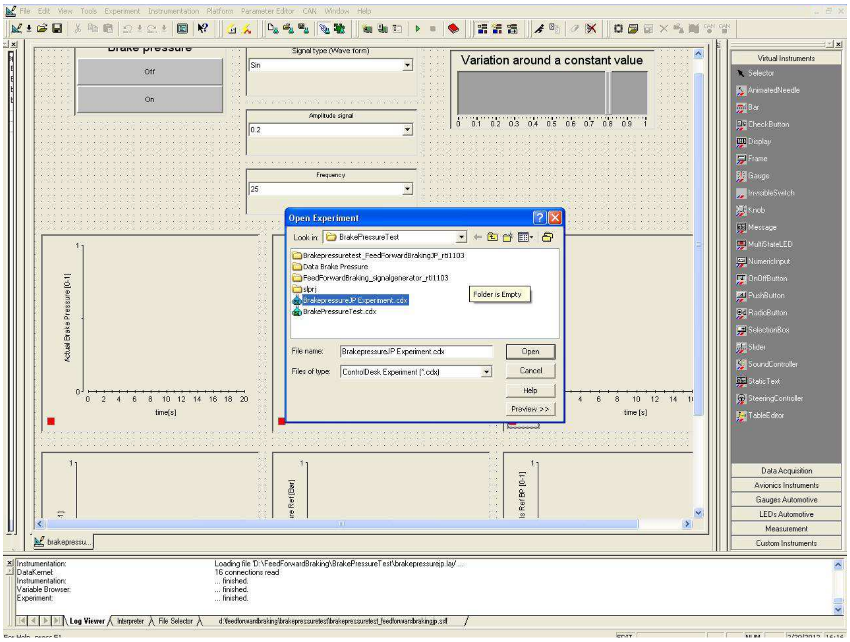

Figure A-4.1 Open Experiment in dSPACE ControlDesk panel

After opening the experiment, a belonging automatic generated SDF file has to be loaded to activate the actuation and measuring the data real time. The data is logged by the data acquisition of ControlDesk, see figure A-4.2. Every measurement is started and stopped with this tool by clicking on the Start / Stop button. Also the length of each measurement can be set and changed.

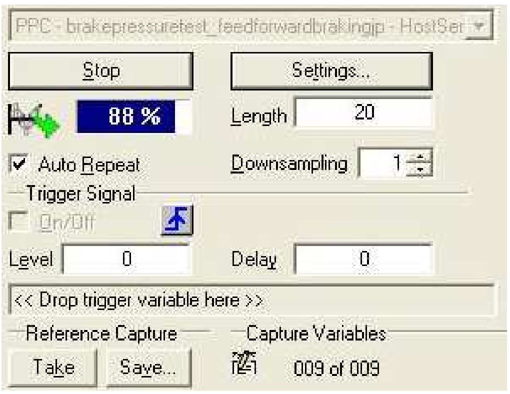


Figure A-4.2 Data acquisition dSPACE ControlDesk panel

Define the saving destination of the data during the logging, which is shown in figure A-4.3 There are five possibilities to save the data, depending on how the data has to be stored. During this thesis project “Autoname” is used, after every twenty seconds the saved data gets is sequenced by a number.

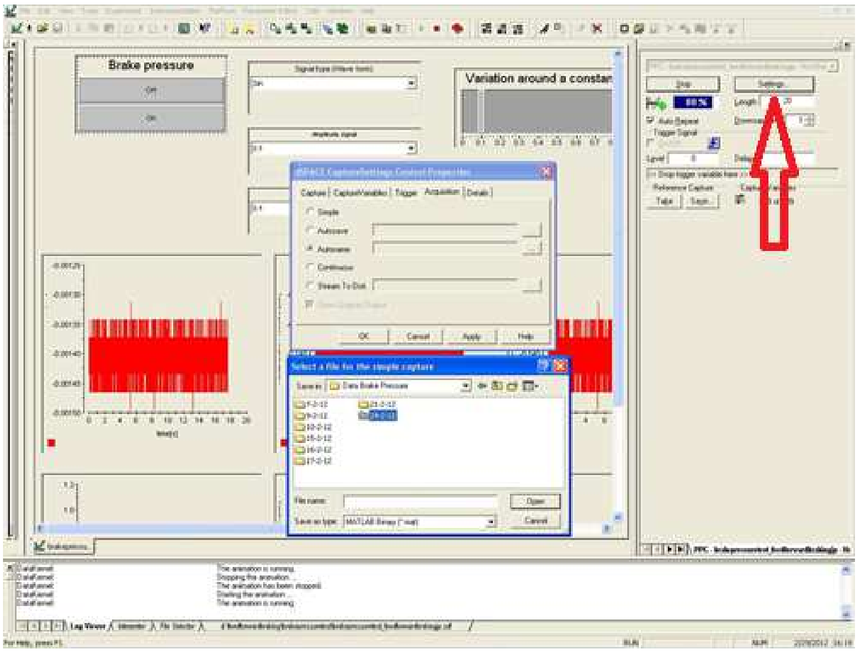

Figure A-4.3 Defining the saving destination of the data in dSPACE ControlDesk panel, click on button marked with the red arrow

Figure A-4.4 shows the selection of the SDF file to load the application or model. This file is needed to connect the measured data with the model.

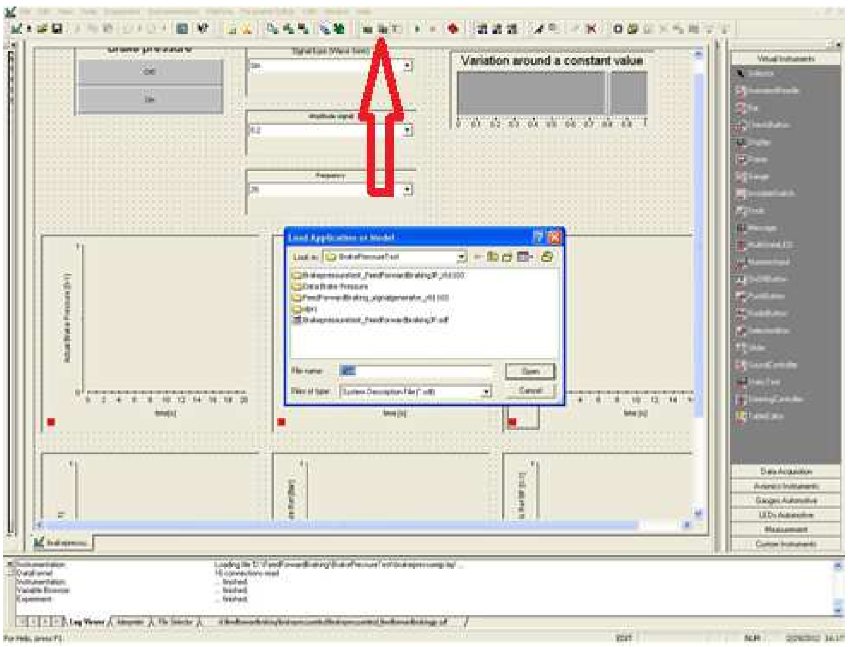

Figure A-4.4 Open a SDF file in dSPACE ControlDesk panel, click on button marked with the red arrow

To start the actuation and measurement the “Animation mode” has to be switched on in the ControlDesk panel as figure A-4.5 shows.

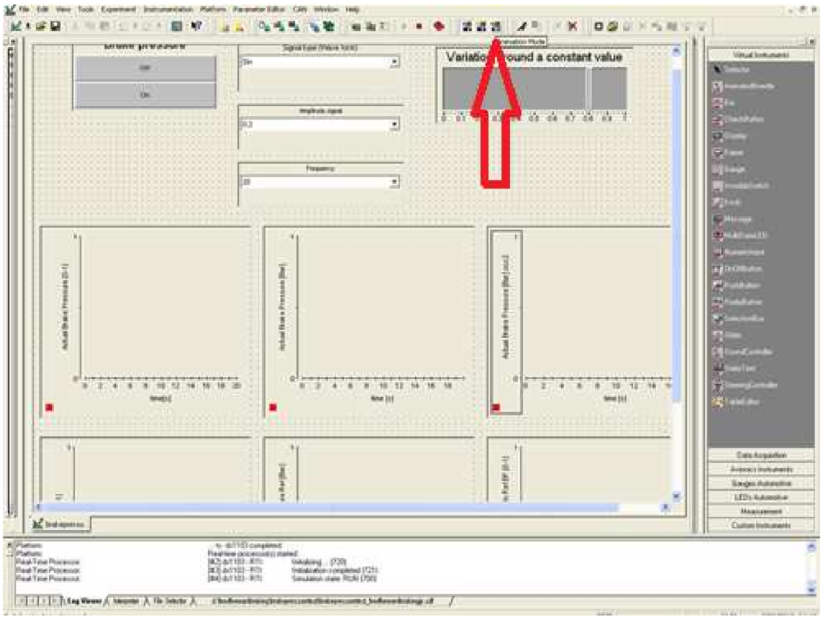

Figure A-4.5 Set on “animation mode” dSPACE ControlDesk panel, click on button marked with the red arrow

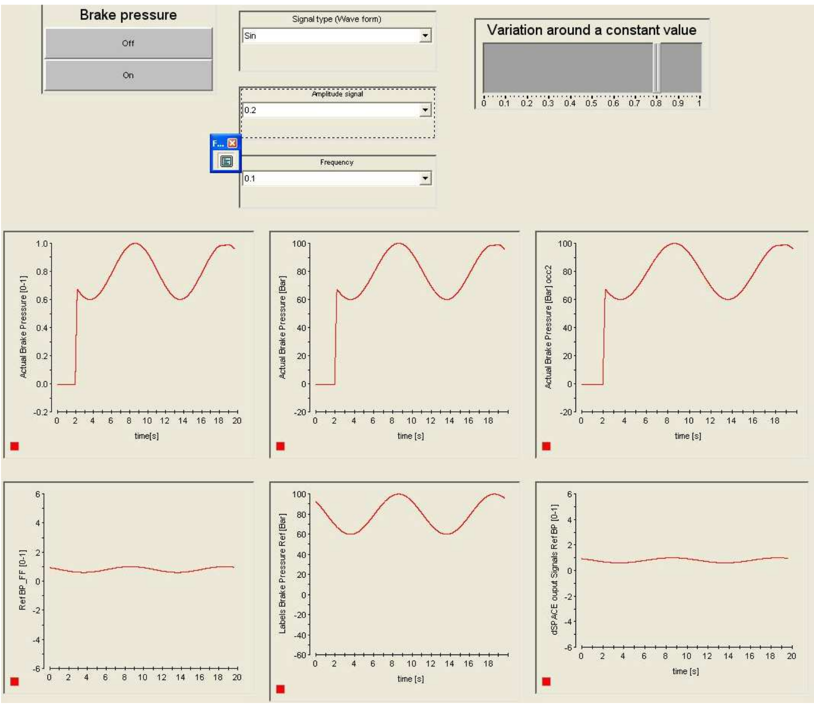


Figure A-4.6 dSPACE ControlDesk panel for static brake pressure measurements

The control panel contains (see figures A-4.5 and A-4.6):

1. ON-OFF buttons
2. A constant pressure value slider
3. graphs with measuring parameters
4. settings of the actuating signal
5. data acquisition

## A-5 The data preparation order

1. *Make a Matlab file to load the test data and display the graph(s) in Matlab.*

The selected signals to display the brake pressure graphs in the ControlDesk panel are the numbers 001 till 006 in green. These names are chosen by the people who were involved earlier in designing the Feed-Forward Matlab Simulink model. The data from 001 till 006 and the time are related to the data columns and presented with short names as time and P_act001 till P_act006 to identify easily in Matlab.

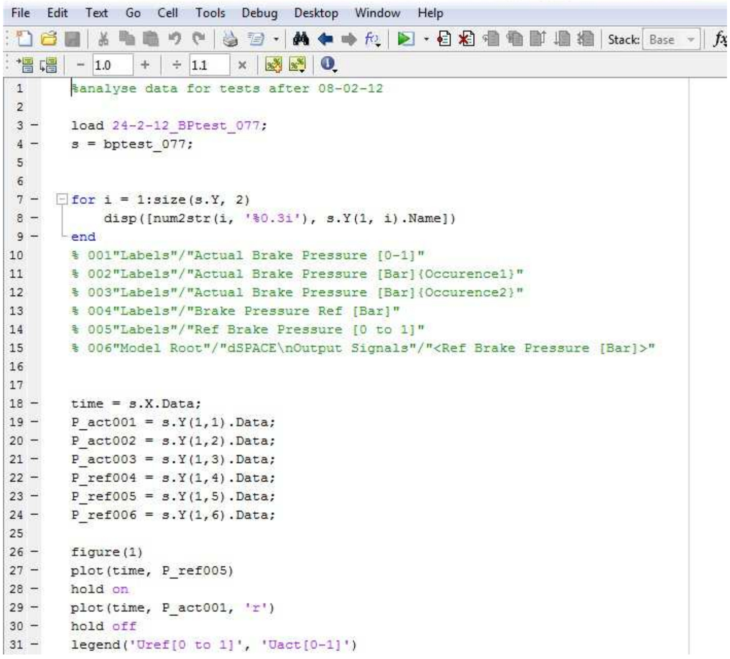

Figure A-5.1 “JPanalizer” to load and display the test data

2. *Run “JPanalizer” in Matlab.*

Brake pressure data P_act001-P_act006 and time are displayed in Workspace of Matlab. The sizes of each data <1 row x 20481 columns> with the minimal as maximal values are shown in figure 4.2.

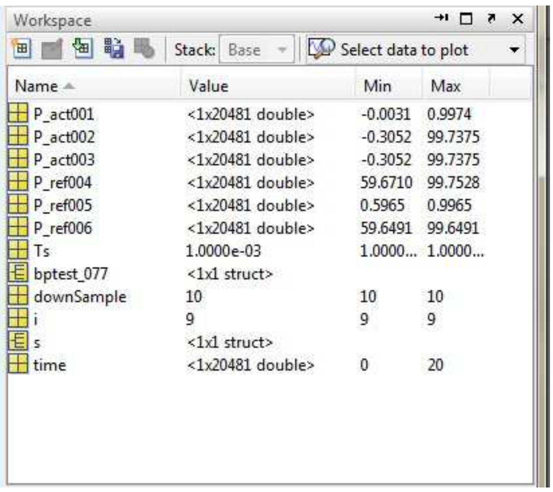


| Name | Value | Min | Max |
|---|---|---|---|
| P_act001 | <1x20481 double> | -0.0031 | 0.9974 |
| P_act002 | <1x20481 double> | -0.3052 | 99.7375 |
| P_act003 | <1x20481 double> | -0.3052 | 99.7375 |
| P_ref004 | <1x20481 double> | 59.6710 | 99.7528 |
| P_ref005 | <1x20481 double> | 0.5965 | 0.9965 |
| P_ref006 | <1x20481 double> | 59.6491 | 99.6491 |
| Ts | 1.0000e-03 | 1.0000... | 1.0000... |
| bptest_077 | <1x1 struct> | | |
| downSample | 10 | 10 | 10 |
| i | 9 | 9 | 9 |
| s | <1x1 struct> | | |
| time | <1x20481 double> | 0 | 20 |

Figure A-5.2 “JPanalizer” displayed in Matlab

3. *To differ the several brake pressure data form each measurement, the data of each test getting a unique name.*

This is done for the actual brake pressure 001 (i.e. jpact77=P_act001'), the reference brake pressure 005 (i.e. jpact77=P_ref005') and the time (i.e. t77=time'). The ' sign indicates the transposed from 1 row and 20481 columns into 1 column and 20481 rows. By selecting the whole column, it can be copied into an Excel sheet.

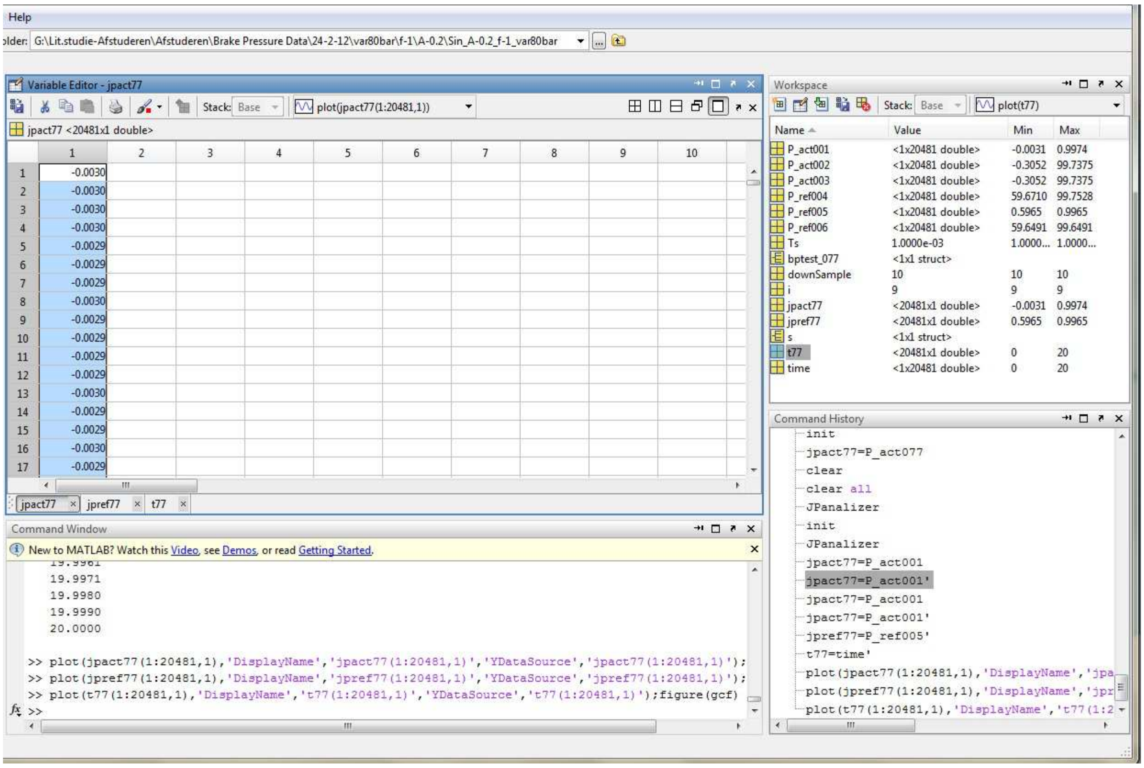

Figure A-5.3 Selecting and copying the blue column 1 into an Excel sheet

## A-6 Signal analysis

1. *Random noise excitation at a constant average of 50bar, varying amplitude of 0.1-0.9 bar*

**Figure A-6.1 Transfer functions at a constant average 50bar**

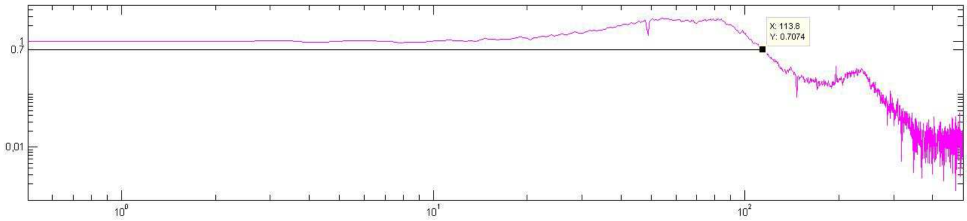


A-0.1bar_50bar, bandwidth at 113.8 Hz

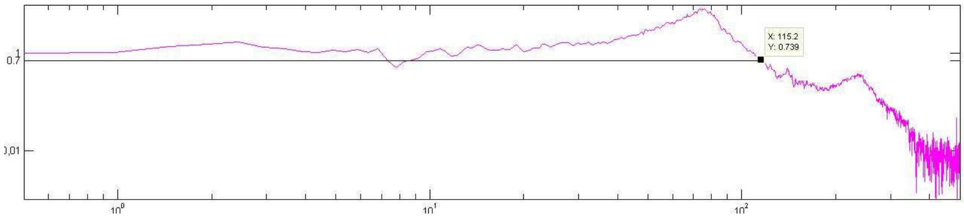


A-0.2bar_50bar, bandwidth at 115.2 Hz

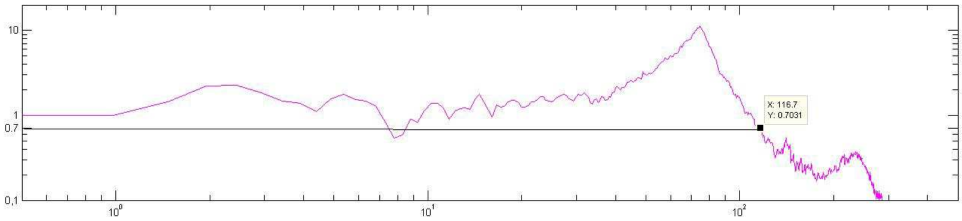


A-0.3bar_50bar, bandwidth at 116.7 Hz

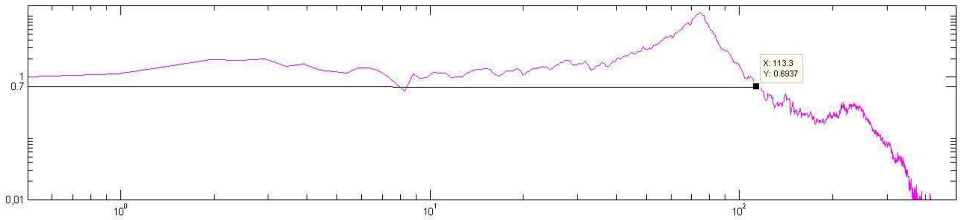


A-0.4bar_50bar, bandwidth at 113.3 Hz

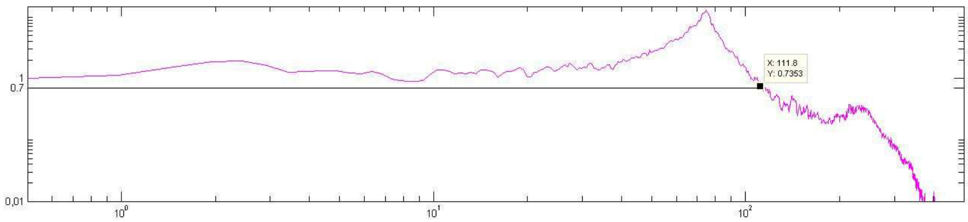


A-0.5bar_50bar, bandwidth at 111.8 Hz

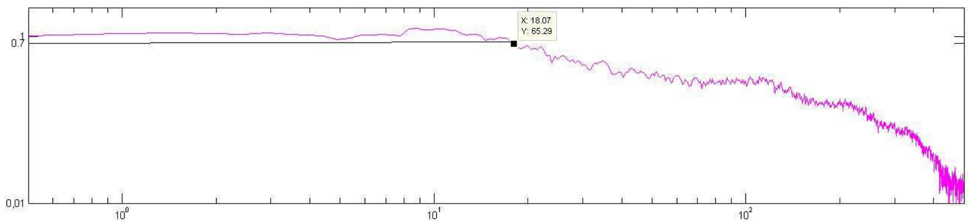


A-0.5bar_50bar, cross over frequency 300Hz bandwidth at 18.07 Hz

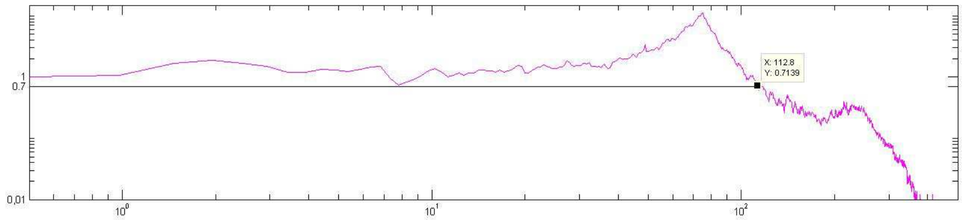


A-0.6bar_50bar, bandwidth at 112.8 Hz

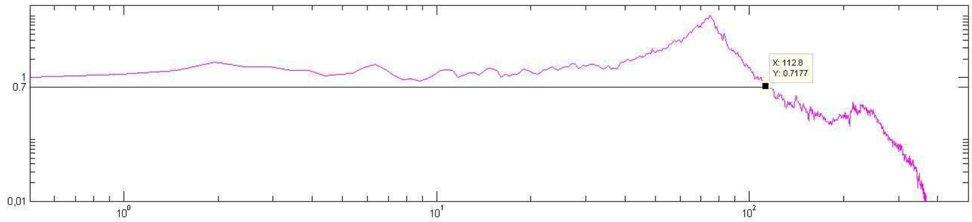


A-0.7bar_50bar, bandwidth at 112.8 Hz

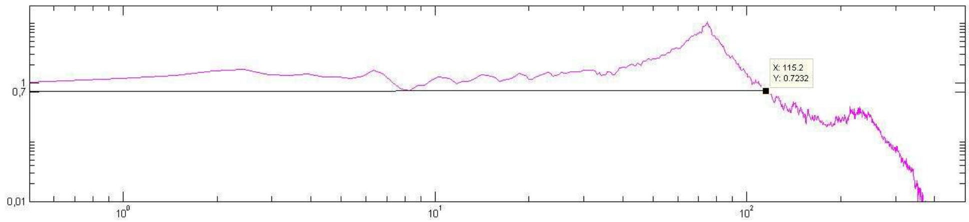


A-0.8bar_50bar, bandwidth at 115.2 Hz

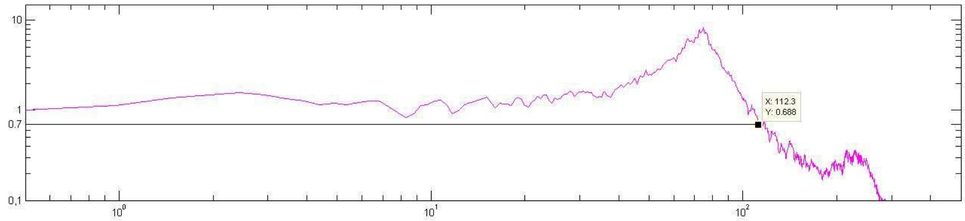


A-0.9bar_50bar, bandwidth at 112.3 Hz

**Figure A-6.2 Phase shifts/time delays at a constant average 50bar**

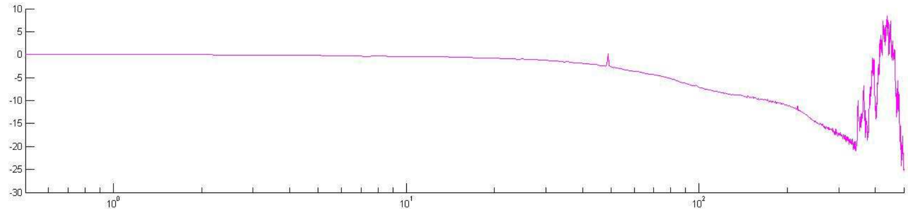


A-0.1bar_50bar

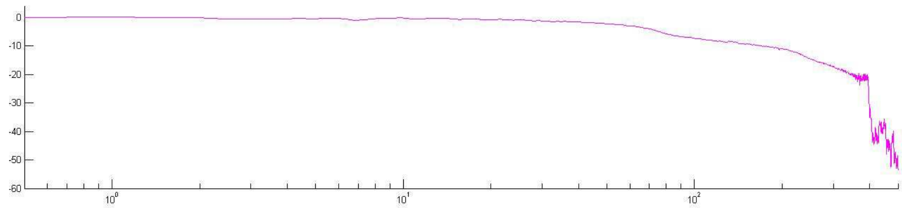


A-0.2bar_50bar

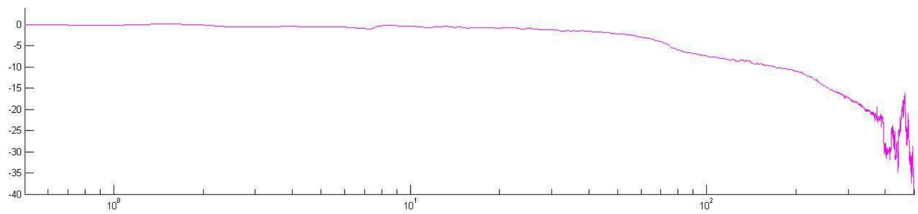


A-0.3bar_50bar

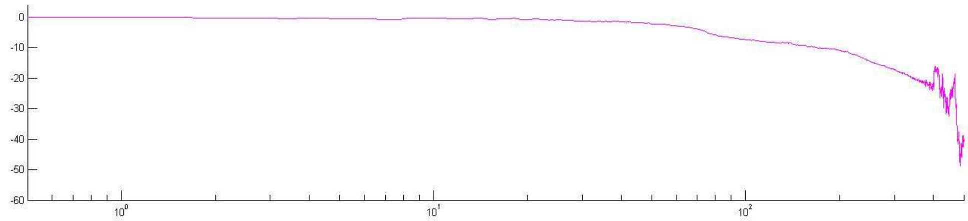

A-0.4bar_50bar

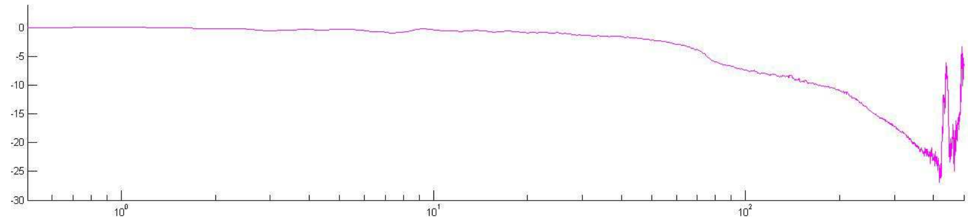

A-0.5bar_50bar

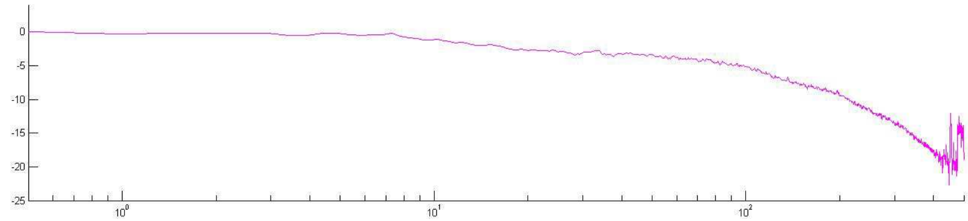

A-0.5bar_50bar, cross over frequency 300Hz

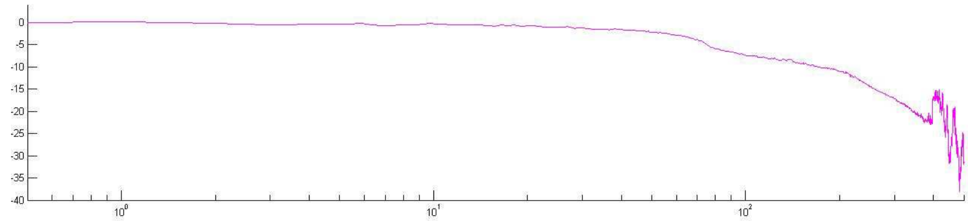

A-0.6bar_50bar

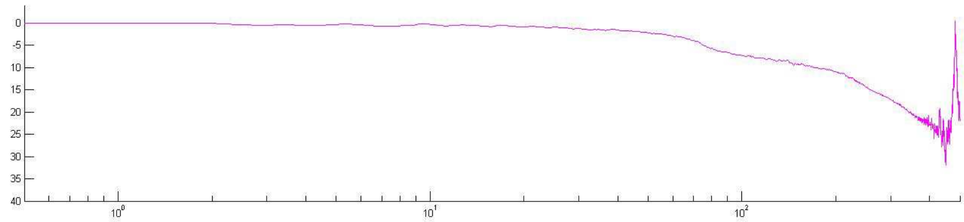

A-0.7bar_50bar

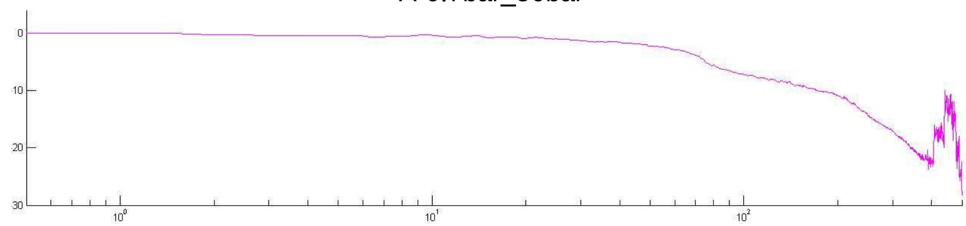

A-0.8bar_50bar

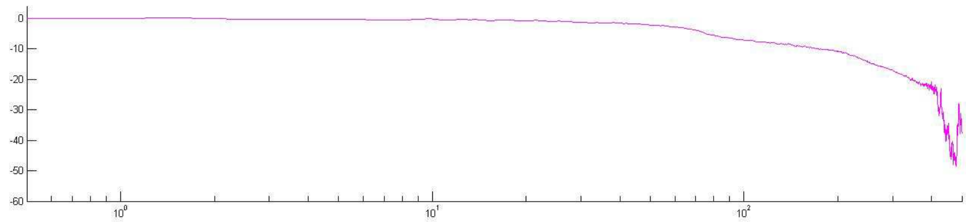

A-0.9bar_50bar

## Figure A-6.3 Coherence at a constant average 50bar

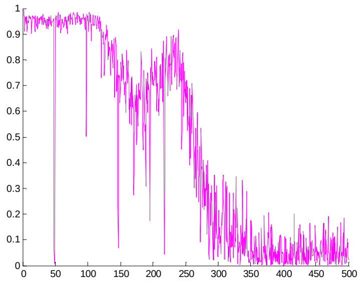
A-0.1bar_50bar

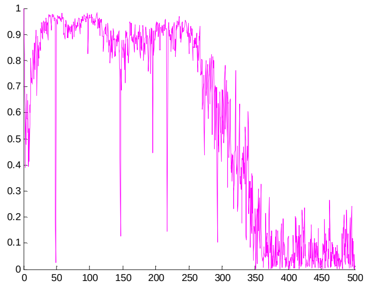
A-0.2_50bar

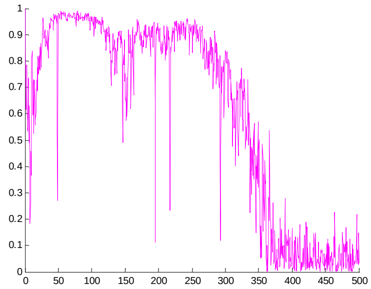
A-0.3bar_50bar

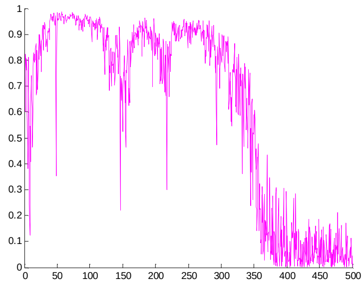
A-0.4bar_50bar

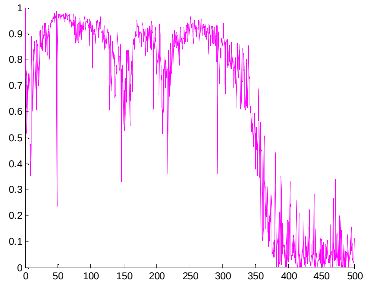
A-0.5bar_50bar

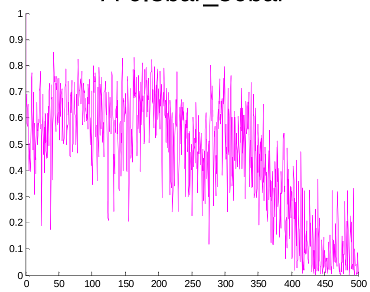
A-0.5bar_50bar 300Hz

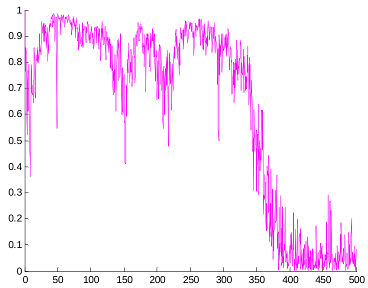
A-0.6bar_50bar

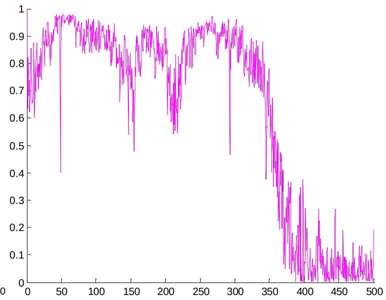
A-0.7bar_50bar

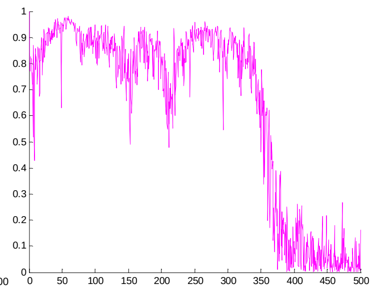
A-0.8bar_50bar

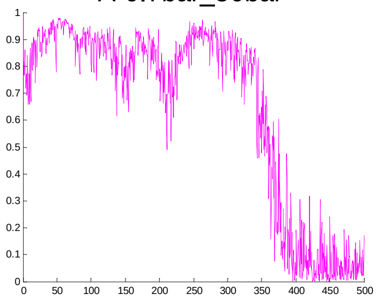
A-0.9bar_50bar

2. *Random noise excitation of at a constant average of 80bar, varying amplitude of 0.1-0.9 bar*

**Figure A-6.4 Transfer functions at a constant average 80bar**

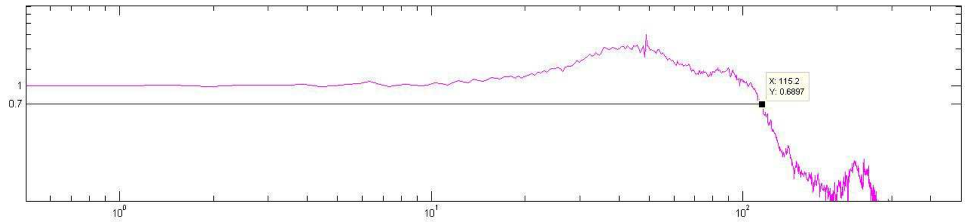


A-0.1bar_80bar, bandwidth at 115.2 Hz

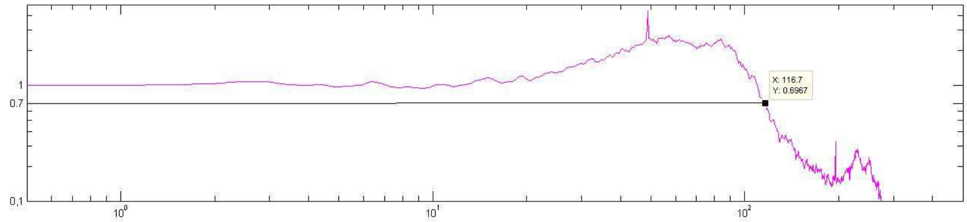


A-0.2bar_80bar, bandwidth at 116.7 Hz

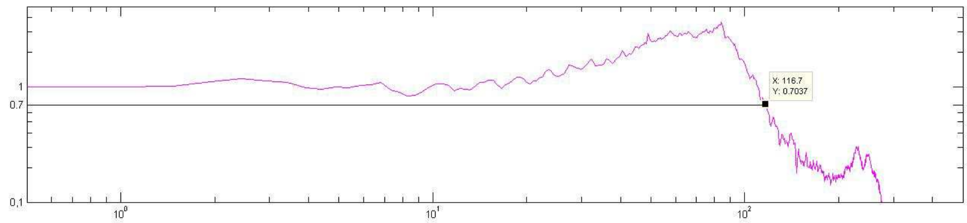


A-0.3bar_80bar, bandwidth at 116.7 Hz

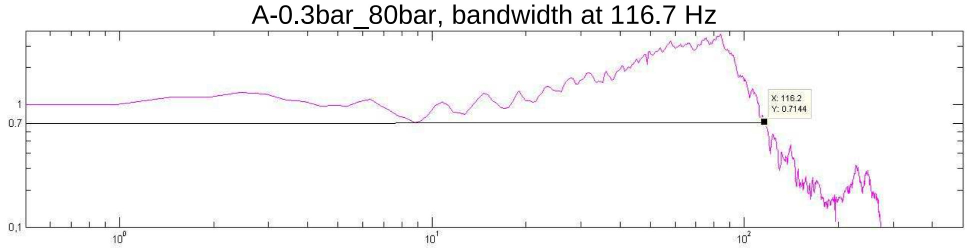


A-0.4bar_80bar bandwidth at 116.2 Hz

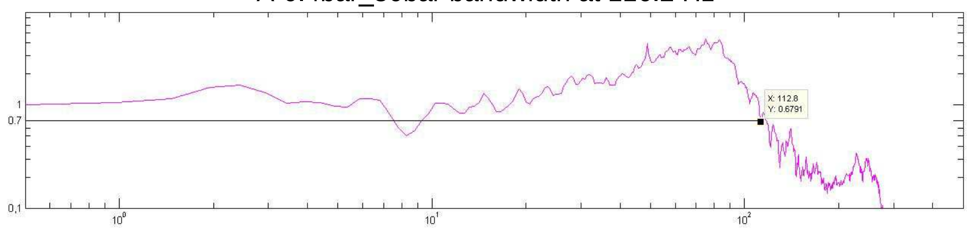


A-0.5bar_80bar, bandwidth at 112.8 Hz

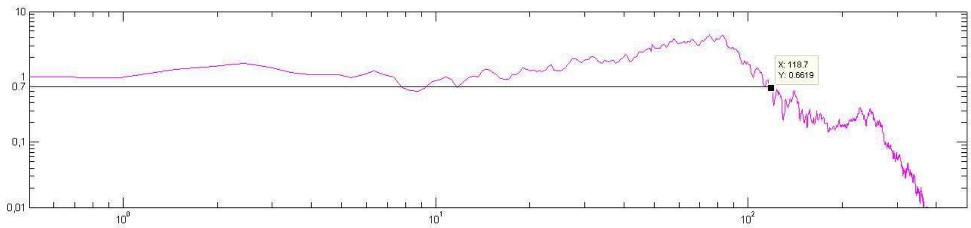


A-0.6_80bar, bandwidth at 118.7 Hz

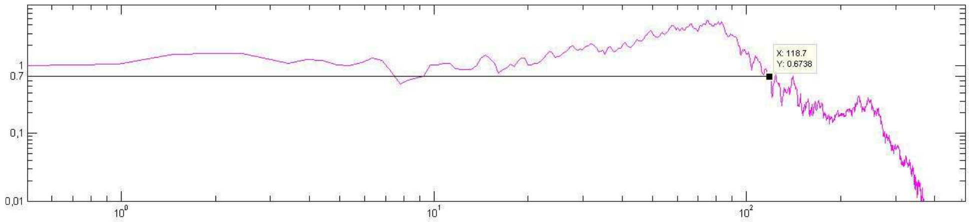

A-0.7bar_80bar, bandwidth at 118.7 Hz

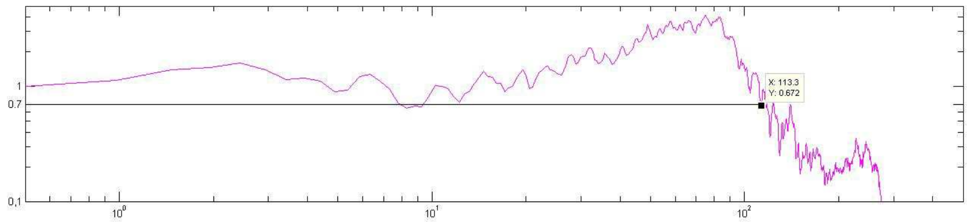

A-0.8bar_80bar, bandwidth at 113.3 Hz

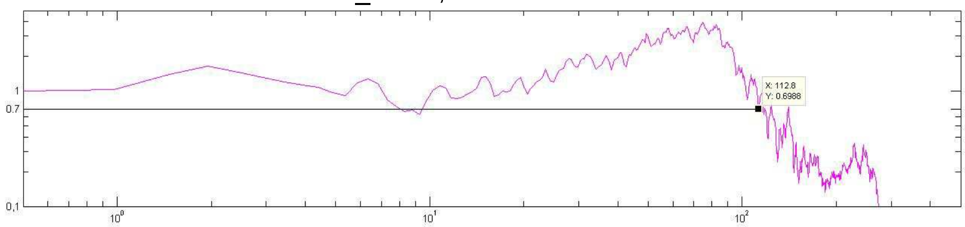

A-0.9bar_80bar, bandwidth at 112.8 Hz

**Figure A-6.5 Phase shifts/time delays at a constant average 80bar**

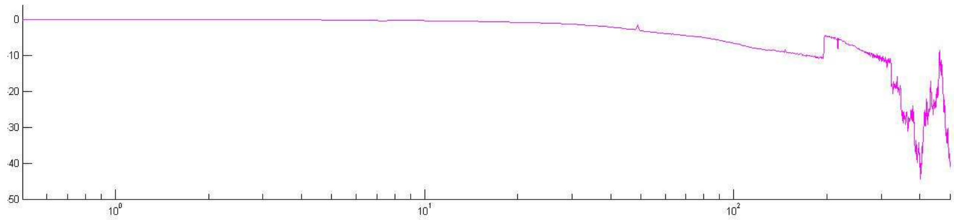
A-0.1bar_80bar

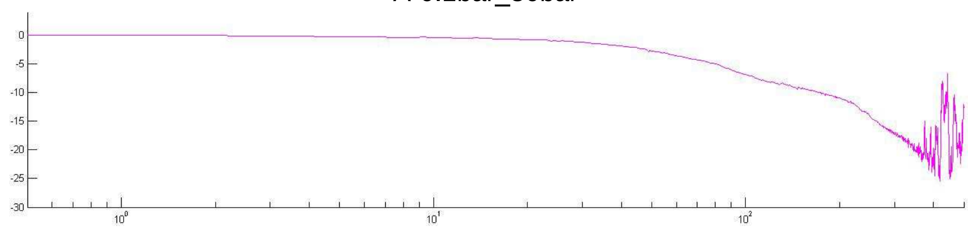
A-0.2bar_80bar

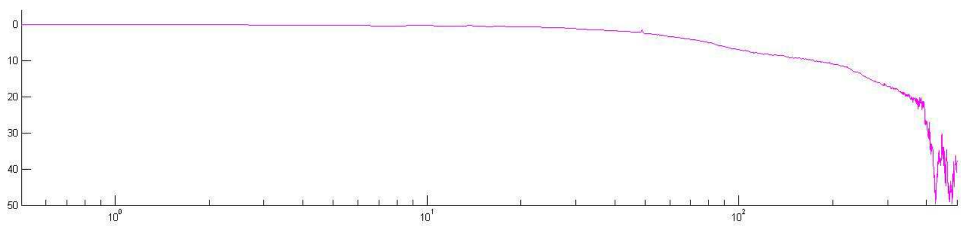
A-0.3bar_80bar

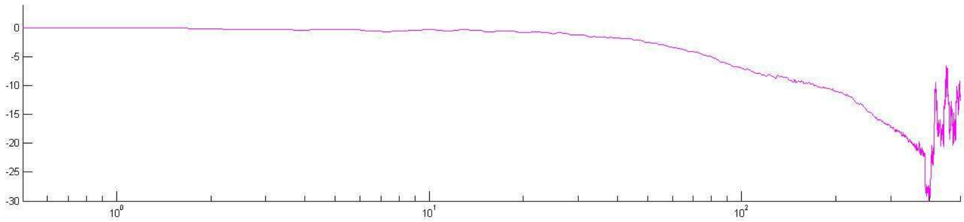

A-0.4bar_80bar

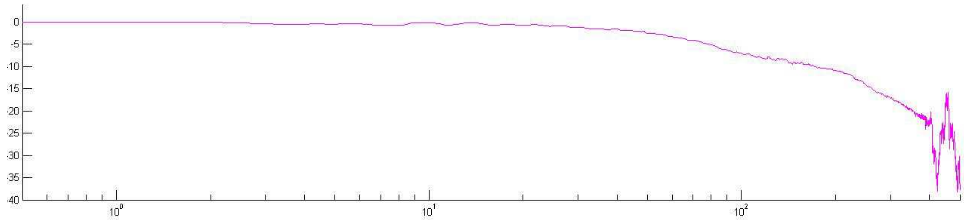

A-0.5bar_80bar

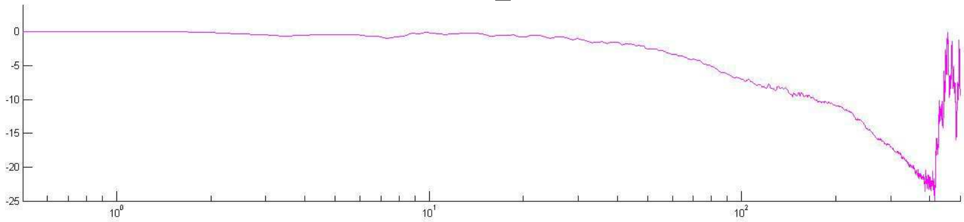

A-0.6bar_80bar

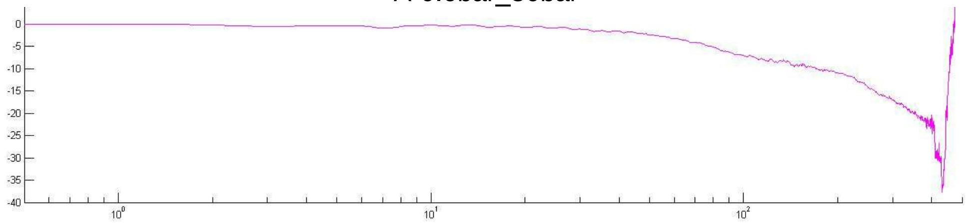

A-0.7bar_80bar

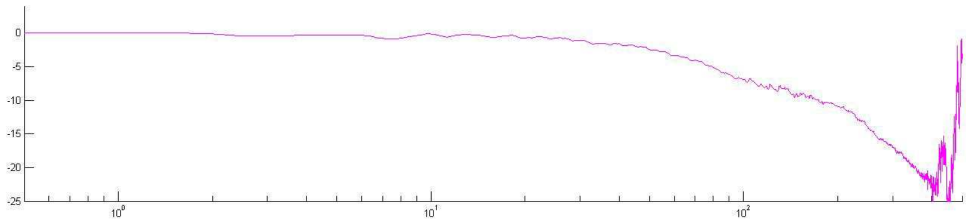

A-0.8bar_80bar

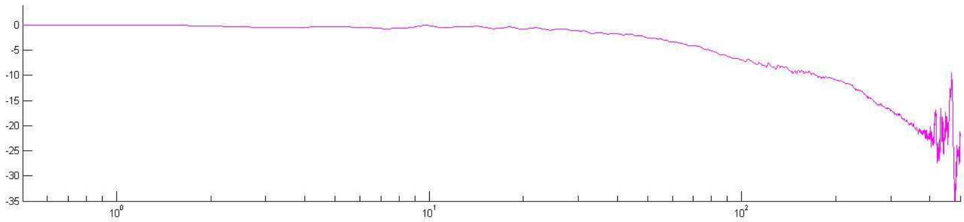

A-0.9bar_80bar

**Figure A-6.6 Coherence at a constant average 80bar**

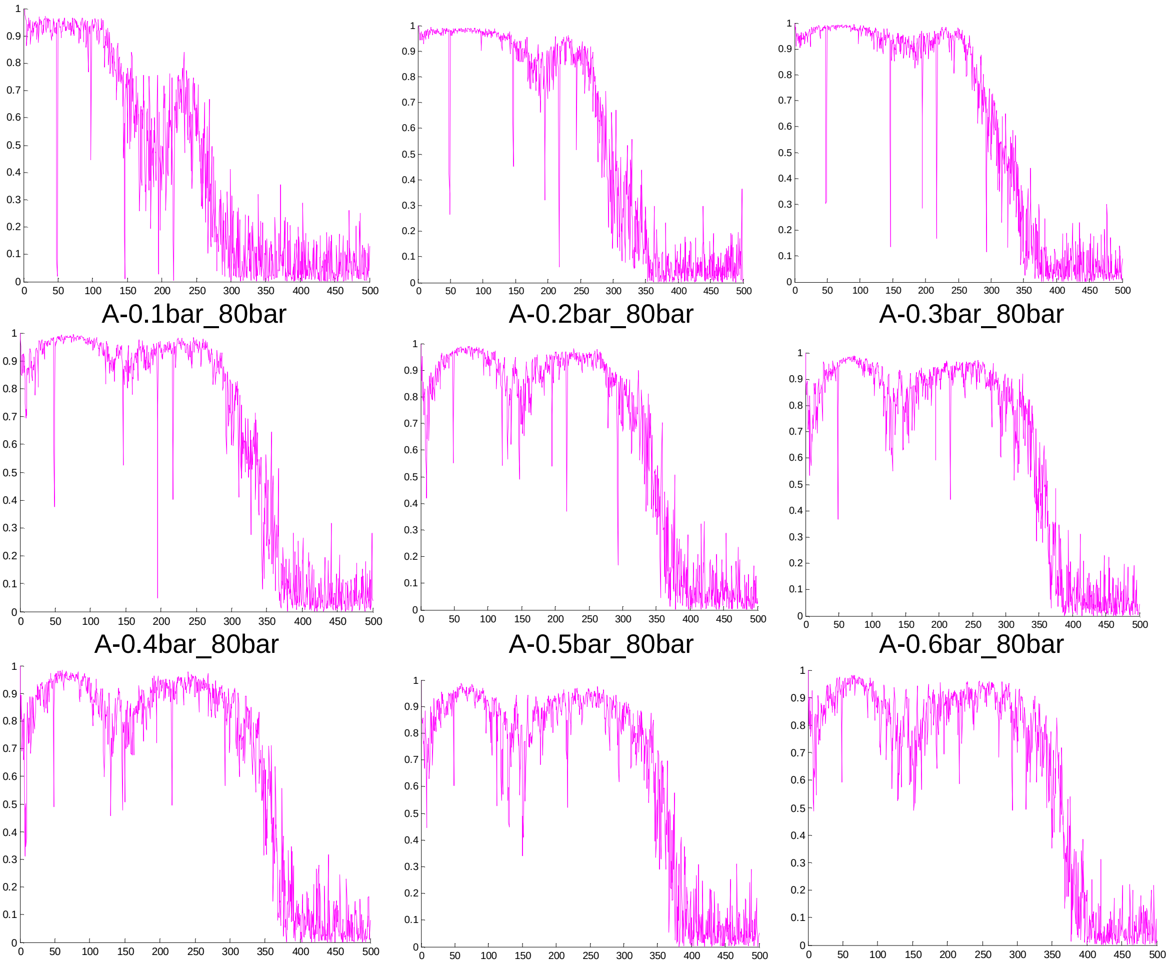

A-0.1bar_80bar A-0.2bar_80bar A-0.3bar_80bar

A-0.4bar_80bar A-0.5bar_80bar A-0.6bar_80bar

A-0.7bar_80bar A-0.8bar_80bar A-0.9bar_80bar

3. *Random noise excitation of at a constant average of 80bar, several varying amplitudes of 0.5bar, 1bar, and 20 bar and different corner frequencies shifted from 150Hz to 300Hz and 40Hz.Also different gain settings included.*

**Figure A-6.7 Transfer functions at a constant average 80bar**

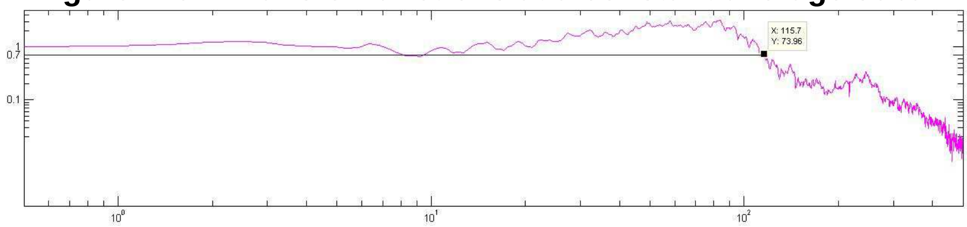


A-0.5bar_80bar 300Hz bandwidth at 115.7 Hz

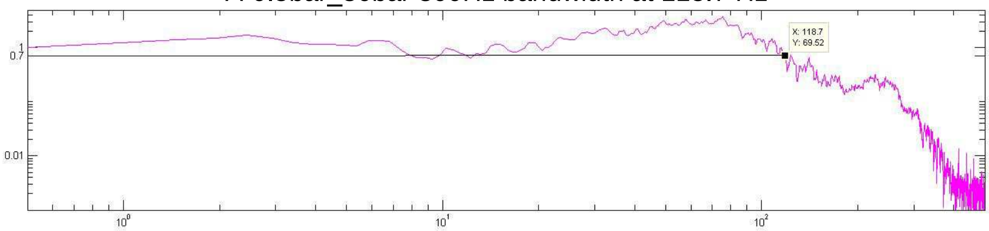


A-1bar_80bar 300Hz bandwidth at 118.7 Hz

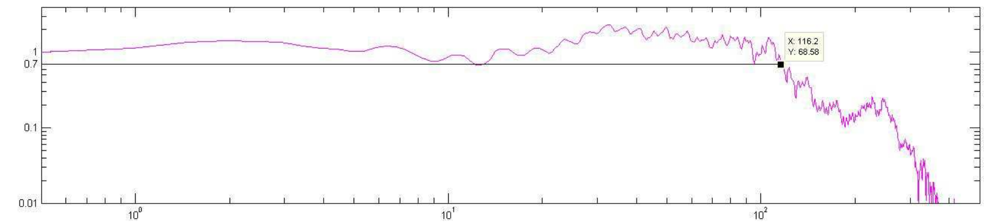

A-1bar_80bar 300Hz bandwidth at 116.2 Hz (filtered input ch6)

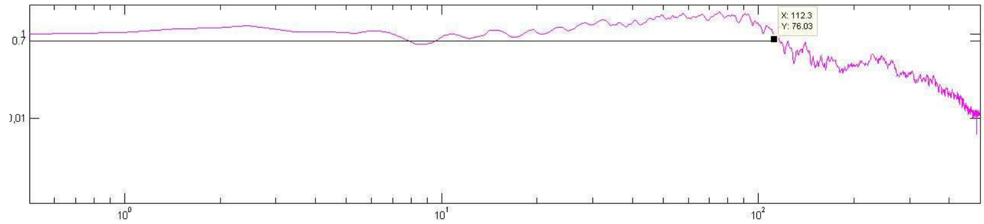

A-1bar_80bar 300Hz bandwidth at 112.3 Hz bgain 2.00

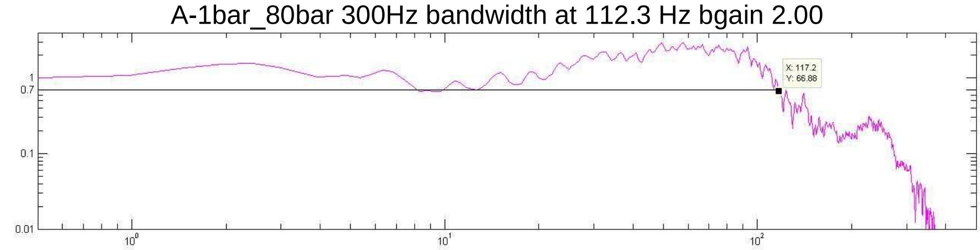

A-1bar_80bar 300Hz bandwidth at 117.2 Hz bgain 5.00

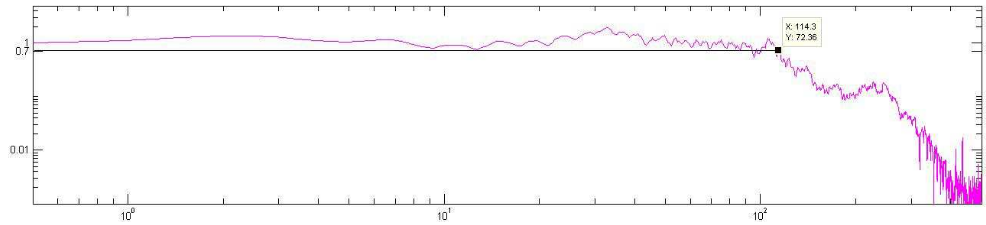

A-1bar_80bar 300Hz bandwidth at 114.3 Hz bgain 9.90

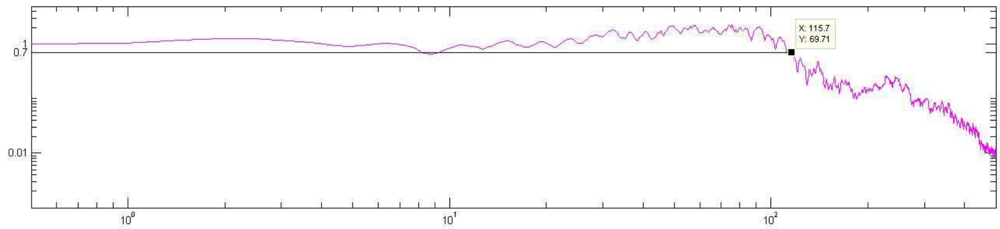

A-1bar_80bar 300Hz bandwidth at 115.7 Hz ogain 2.00

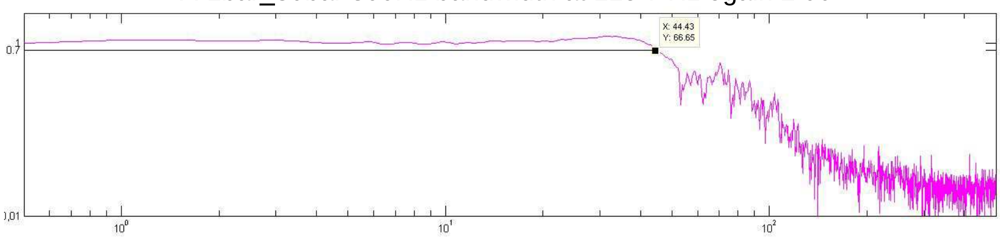

A-5bar_80bar 40 Hz bandwidth at 44.43 Hz

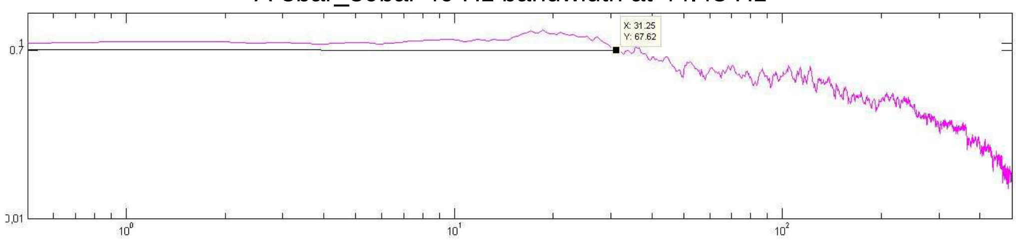

A-20bar_80bar 300Hz bandwidth at 31.25 Hz

**Figure A-6.8 Phase shifts/time delays at a constant average 80bar**

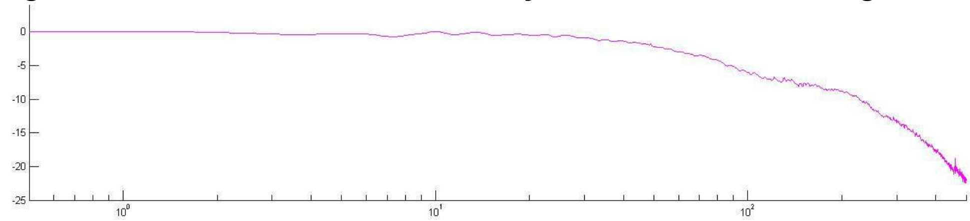

A-0.5bar_80bar 300Hz

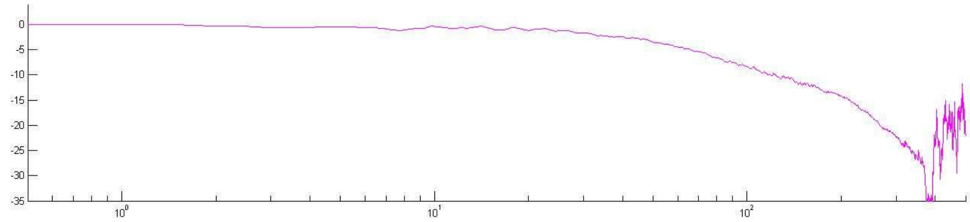

A-1bar_80bar 300Hz

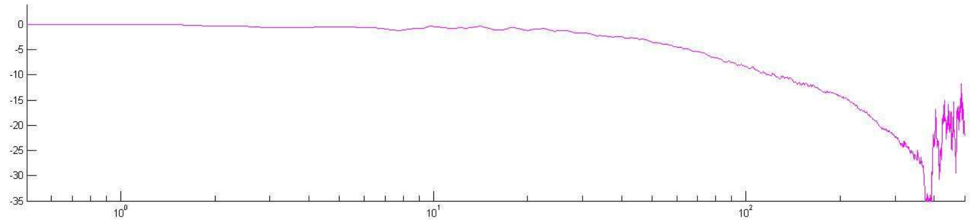

A-1bar_80bar 300Hz (filtered input ch6)

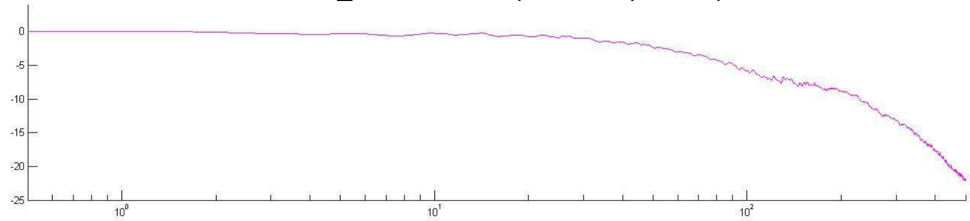

A-1bar_80bar 300Hz, bgain 2.00

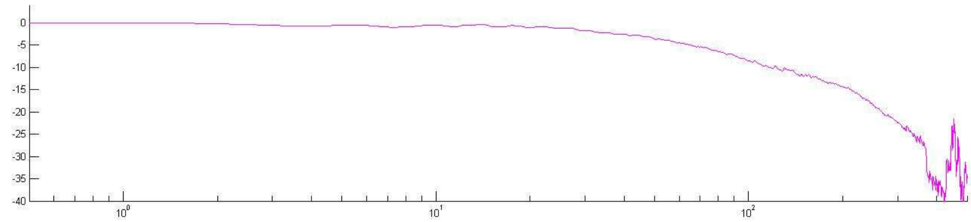

A-1bar_80bar 300Hz, bgain 5.00

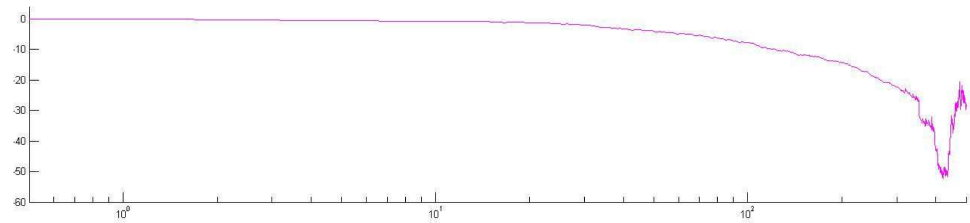

A-1bar_80bar 300Hz, bgain 9.90

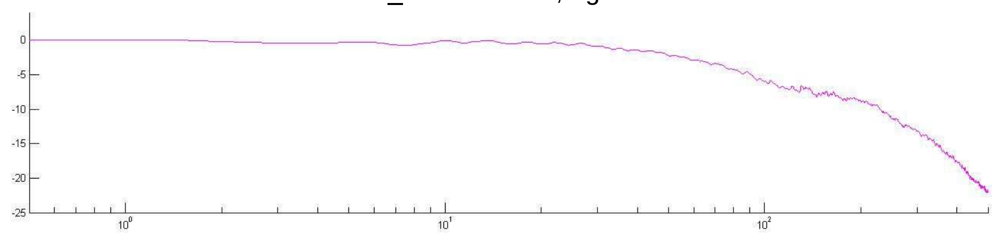

A-1bar_80bar 300Hz, ogain 2.00

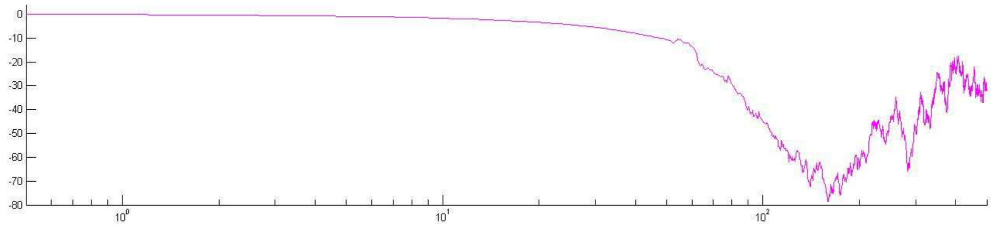

A-5bar_80bar 40Hz

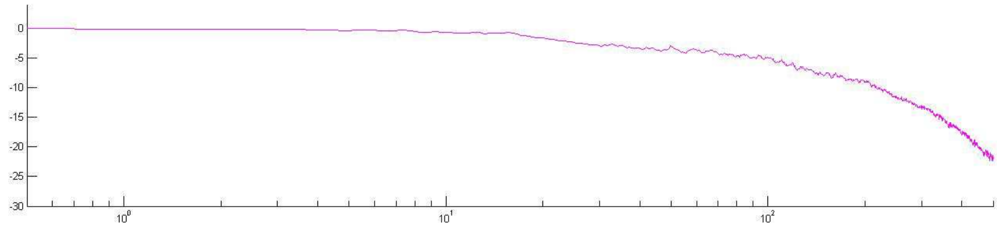

A-20bar_80bar, 300Hz

**Figure A-6.9 Coherence at a constant average 80bar**

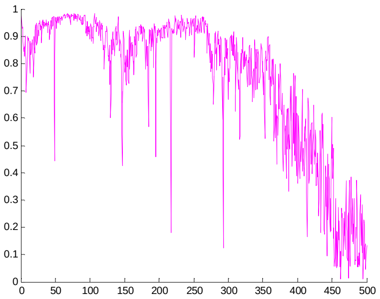

A-0.5bar_80bar 300Hz

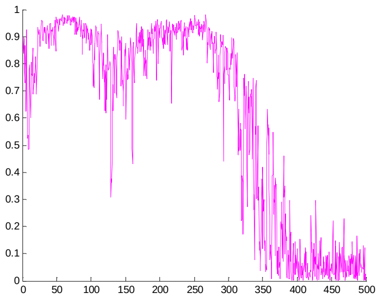

A-1bar_80bar 300Hz

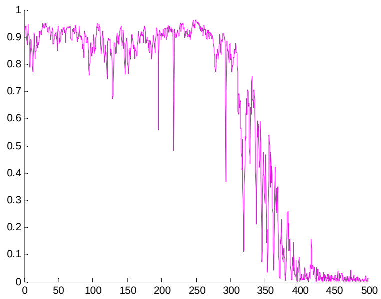

A-1bar_80bar 300Hz
(filtered input ch6)

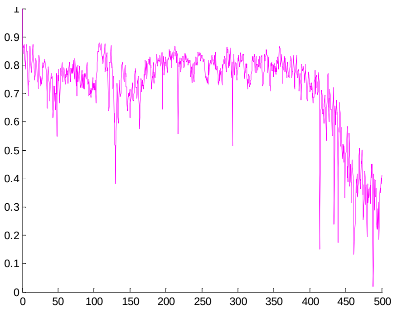

A-1bar_80bar bgain 2.00

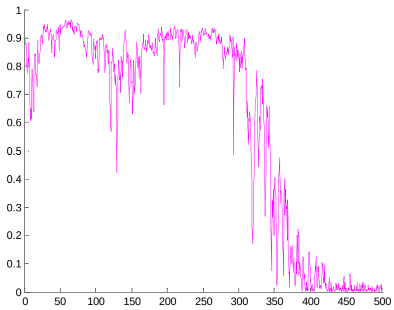

A-1bar_80bar bgain 5.00

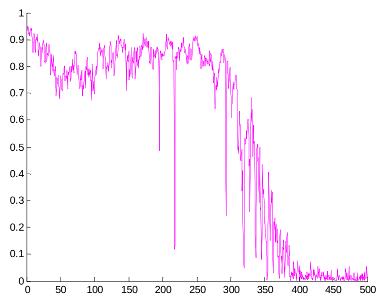

A-1bar_80bar bgain 9.90

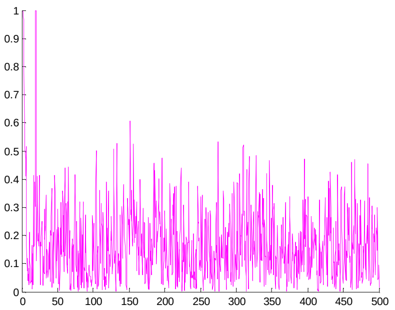

A-1bar_80bar ogain 2.00

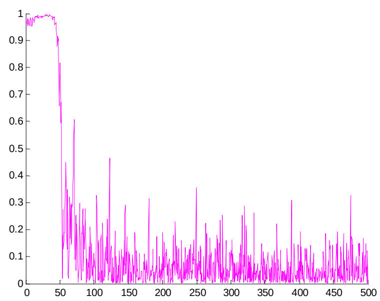

A-5bar_80bar, 40Hz

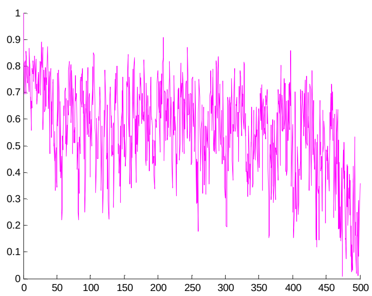

A-20bar_80bar, 300Hz